Universal Time effects on substorm growth phases and onsets

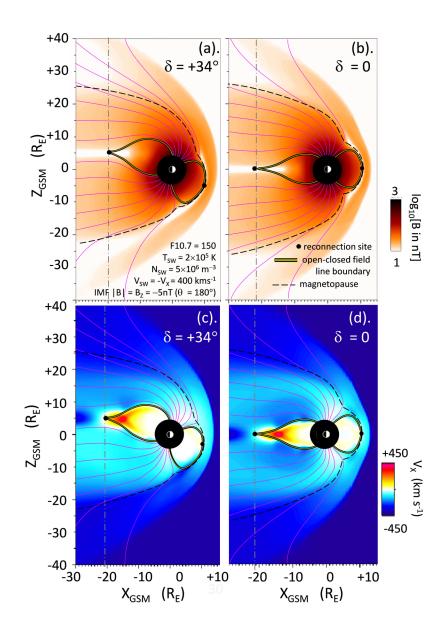
Michael Lockwood¹

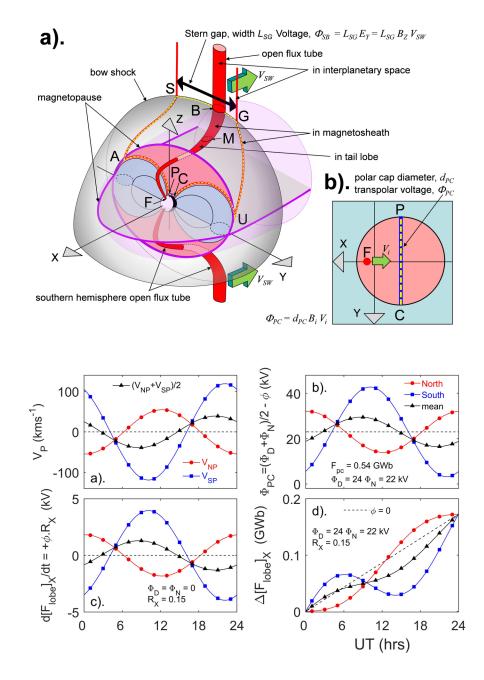
¹University of Reading

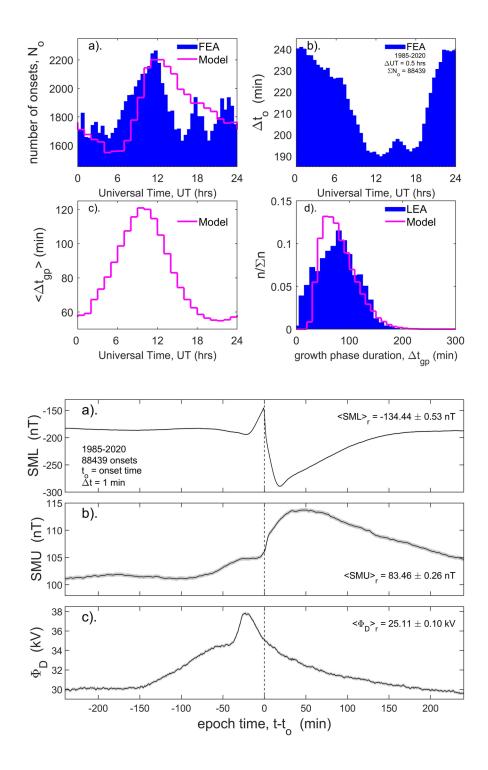
May 25, 2023

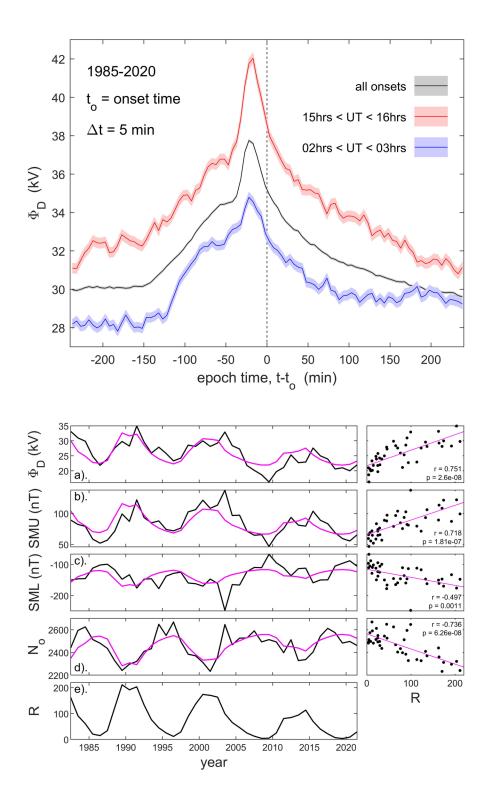
Abstract

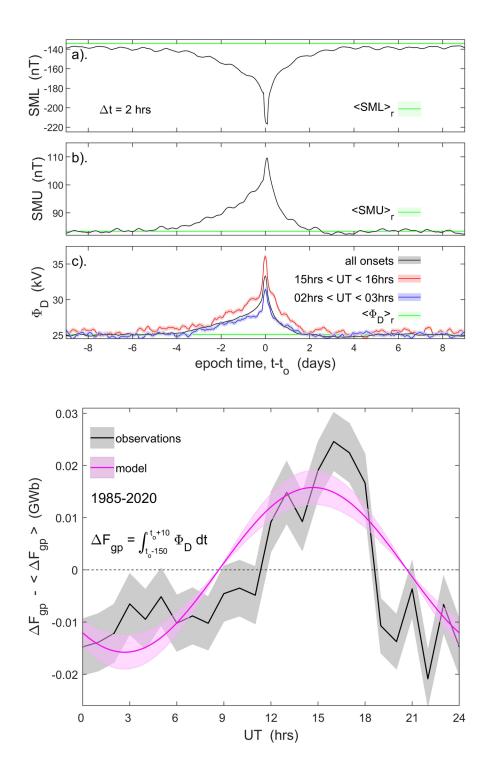
Universal Time UT variations in many magnetospheric state indicators and indices have recently been reviewed by (Lockwood and Milan, 2023). Key effects are introduced into magnetospheric dynamics by the eccentric nature of Earth's magnetic field, features that cannot be reproduced by a geocentric field model. This paper studies the UT variation in the occurrence of substorm onsets and uses a simple Monte-Carlo model to show how it can arise for an eccentric field model from the effect of the diurnal motions of Earth's poles on the part of the geomagnetic tail where substorms are initiated. These motions are in any reference frame that has an X axis that points from the center of the Earth to the center of the Sun and are caused by Earth's rotation. The premise behind the model is shown to be valid using a super-posed epoch study of the conditions leading up to onset. These studies also show the surprising degree of preconditioning required, ahead of the growth phase, for onset to occur. A key factor is the extent to which pole motions caused by Earth's rotation influence the near-Earth tail at the relevant X coordinate. Numerical simulations by a global MHD model of the magnetosphere reveal the required effect to generate the observed UT variations and with right order of amplitude, albeit too small by a factor of about one third. Reasons why this discrepancy may have arisen for the simulations used are discussed.

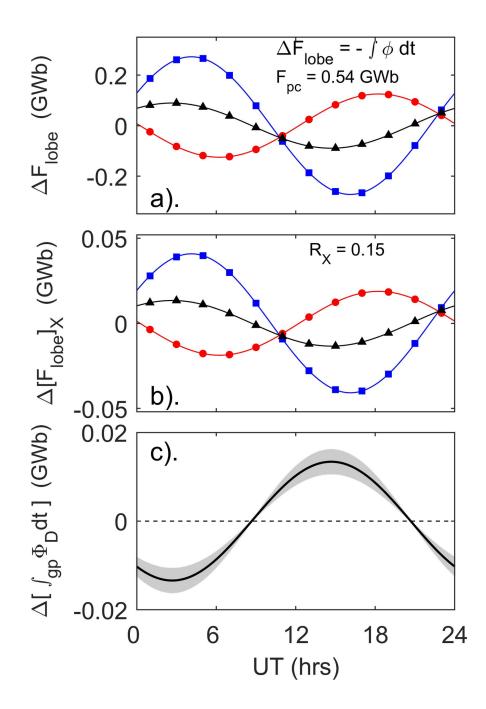


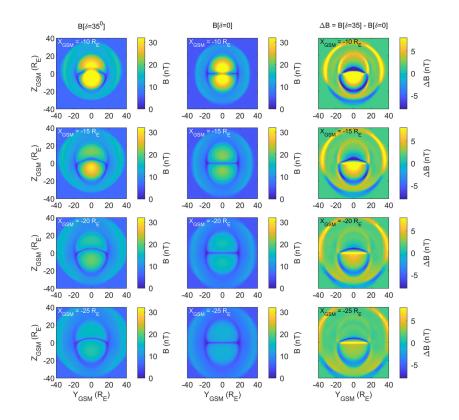


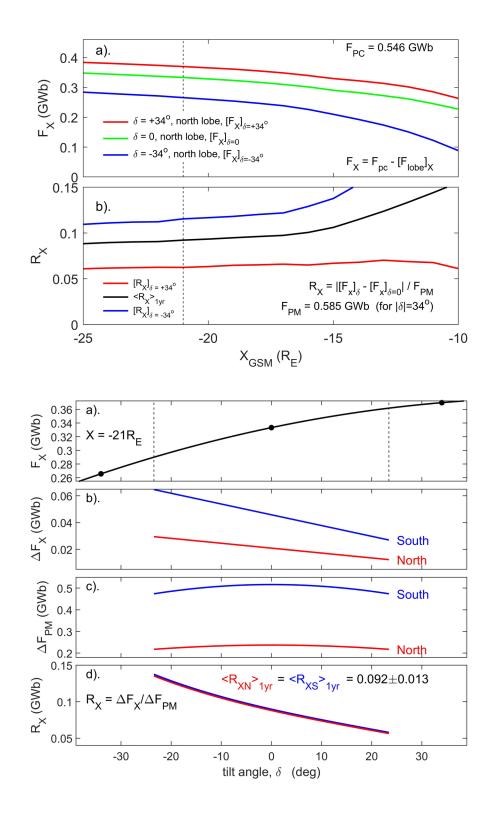


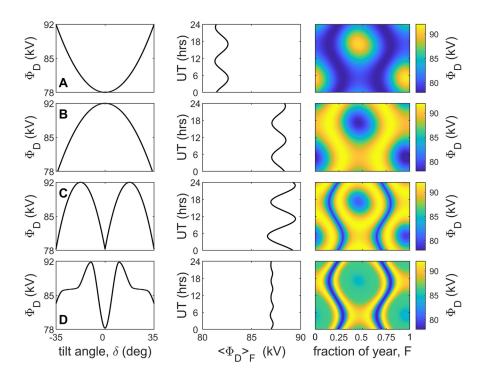












Universal Time effects on substorm growth phases and onsets

$\mathbf{M}.\ \mathbf{Lockwood}^1$

 $^1\mathrm{Department}$ of Meteorology, University of Reading, Reading, Berkshire, RG6 6BB, UK

Key Points:

3

4

5

6	•	1 Universal Time effects in the magnetosphere are caused by the eccentric nature
7		of Earth's intrinsic magnetic field
8	•	2 There is a Universal Time dependence of the integrated magnetopause recon-
9		nection voltage needed to trigger substorm onset
10	•	3 Growth phases that lead to substorm onset show considerable preconditioning
11		by prior reconnection

Corresponding author: Mike Lockwood, m.lockwood@reading.ac.uk

12 Abstract

Universal Time (UT) variations in many magnetospheric state indicators and indices have 13 recently been reviewed by Lockwood and Milan (2023). Key effects are introduced into 14 magnetospheric dynamics by the eccentric nature of Earth's magnetic field, features that 15 cannot be reproduced by a geocentric field model. This paper studies the UT variation 16 in the occurrence of substorm onsets and uses a simple Monte-Carlo model to show how 17 it can arise for an eccentric field model from the effect of the diurnal motions of Earth's 18 poles on the part of the geomagnetic tail where substorms are initiated. These motions 19 are in any reference frame that has an X axis that points from the centre of the Earth 20 to the centre of the Sun and are caused by Earth's rotation. The premise behind the model 21 is shown to be valid using a super-posed epoch study of the conditions leading up to on-22 set. These studies also show the surprising degree of preconditioning required, ahead of 23 the growth phase, for onset to occur. A key factor is the extent to which pole motions 24 caused by Earth's rotation influence the near-Earth tail at the relevant X coordinate. 25 Numerical simulations by a global MHD model of the magnetosphere reveal the required 26 effect to generate the observed UT variations and with right order of amplitude, albeit 27 too small by a factor of about one third. Reasons why this discrepancy may have arisen 28 for the simulations used are discussed. 29

³⁰ Plain Language Summary

Earth's magnetic field is eccentric in that the main magnetic (dipole) axis does not pass through the centre of the Earth. This introduces a wobble into many aspect of near-Earth space as Earth rotates. Many consequences of this have been noted in previous papers. This paper investigates the effect of the eccentricity on the phenomenon of magnetospheric substorms. It is shown that the explosive releases of energy stored in tail are more likely to start ("onset") at some Universal Times (and therefore geographic longitudes) than others and an explanation of why is provided.

38 1 Introduction

39

1.1 Universal Time variations in the magnetosphere

Lockwood and Milan (2023) have recently reviewed Universal Time (UT) varia-40 tions in magnetospheric observations and indices. Their study included: the am plan-41 etary geomagnetic index (Mayaud, 1972; Lockwood et al., 2019); the SML auroral elec-42 trojet index (Newell & Gjerloev, 2011a, 2011b); the SMR partial ring current indices (Newell 43 & Gjerloev, 2012); the polar cap indices (Stauning, 2007; Troshichev, 2022), transpolar 44 voltage observations from Low-Earth Orbit (LEO) spacecraft (e.g., Hairston & Heelis, 45 1993; Boyle et al., 1997), Φ_{PC} ; field aligned-current maps derived from measurements 46 by magnetometers on the Iridium LEO satellites by the AMPERE (Active Magnetosphere 47 and Planetary Electrodynamics Response Experiment) project (Coxon et al., 2018); and 48 substorm onset occurrence (Forsyth et al., 2015; Newell & Gjerloev, 2011a, 2011b). In 49 addition, Lockwood et al. (2021) have modelled the UT variations in the am index and 50 its hemispheric sub-indices an and as and Lockwood et al. (2023) have studied at how 51 UT variations in the magnetosphere-ionosphere-thermosphere coupled system influence 52 the upper atmosphere Joule heating response to terrestrial Coronal Mass Ejection (CME) 53 impacts. 54

UT effects arise in the coupled magnetosphere-ionosphere-thermosphere system because the Earth's magnetic poles are offset from its rotational axis. The most commonly used model of the intrinsic field of Earth is a geocentric dipole, for which this offset is the same in the two hemispheres. This means effects of Earth's rotation in the northern polar regions are equal and opposite to those in the southern polar regions and taking a global average means that many effects cancel and show no net UT variation. How-

ever, constraining Earth's magnetic dipole axis pass through the centre of the Earth is 61 only a useful approximation and eccentric dipole models show that this is not generally 62 valid. The standard way of describing an eccentric dipole, introduced by (Bartels, 1936), 63 is to use the first 8 coefficients that define a spherical harmonic expansion of the magnetic scalar potential, such as the International Geomagnetic Reference Field IGRF (Thébault 65 et al., 2015). This is compared to the first three used to define a centered dipole. In such 66 models the "axial" poles (where the dipole axis threads the Earth surface) are offset from 67 the rotational axis by different amounts in the two hemispheres and these magnetic poles 68 are not separated by 180° in longitude as they are for a geocentric dipole. The eccen-69 tric dipole model of (Koochak & Fraser-Smith, 2017a) gives the latitudinal offset of the 70 axial magnetic pole and the rotational pole of 8.23° in the northern hemisphere in 1980 71 and this fell to 5.91° in 2015. On the other hand, the corresponding values in the south-72 ern hemisphere were 15.29° in 1980 and 14.59° in 2015. Hence the ratio of the South/North 73 magnetic pole offsets has risen from 1.86 to 2.47 in just 35 years because the northern 74 magnetic pole has migrated towards the rotational axis. Many effects of the offset of the 75 rotational and magnetic poles in the two hemispheres that cancel for a geocentric dipole 76 do not cancel for an eccentric one leaving net UT variations. Thus the recent changes 77 in the Earth's intrinsic field mean that UT effects in the magnetosphere-ionosphere-thermosphere 78 system are of increasing importance. There are a number of potential effects discussed 79 in the following subsections. 80

1.2 Ionospheric conductivity effects

81

The most commonly-invoked effect of the offsets of the magnetic and rotational poles 82 is that of the changes in ionospheric conductivity at given polar and auroral locations 83 in geomagnetic coordinates. This is because of the changes in solar zenith angles χ at 84 such locations, which modulates the solar-EUV-generated ionospheric conductivities. This 85 effect has been invoked a great many times in the context of UT variations in geomag-86 netic activity (e.g. Lyatsky et al., 2001; Newell et al., 2002; Wang & Lühr, 2007). This 87 mechanism applies to enhanced conductivity that is generated by solar EUV illumina-88 tion (Ridley et al., 2004) and the effects at a given geomagnetic location are ordered by 89 time-of-year (here quantified by the fraction of a calendar year, F) and UT. However, 90 conductivity is also enhanced by particle precipitation. This second source is ordered in 91 magnetic coordinates and is highly variable in time (Carter et al., 2020). At certain places 92 and times, the precipitation source is dominant over the EUV source (Kubota et al., 2017). 93 Both EUV and precipitation effects show transient events, the former mainly due to so-94 lar flare effects and the latter associated with magnetospheric storms and substorms. In 95 both cases, strong UT variations occur as the event evolves but the timing of the events 96 are essentially random in the UT of their occurrence and so regular, systematic UT vari-97 ations are not seen. We have had good models of EUV-generated conductivity for many 98 years (e.g., Brekke & Moen, 1993) but the variability, in time and space, of precipitation-99 induced conductivity has made the development of equivalent models much more diffi-100 cult and complex (Zhang et al., 2015; Carter et al., 2020). 101

The dependence of EUV-generated conductivity at given geomagnetic coordinates 102 on solar zenith angle means there is a dependence on the dipole tilt angle δ with which 103 the Earth's magnetic axis is tipped towards the Sun. In the Solar Geocentric Ecliptic 104 (GSE) frame, the X axis points from the center of the Earth towards the center of the 105 Sun, the Z axis is the northward normal to the ecliptic and Y makes up the right hand 106 set (and so is antiparallel to Earth's orbital motion). In three dimensions, the Earth's 107 magnetic dipole axis \hat{M} makes an angle ψ with the GSE Z-axis and we here define the 108 dipole tilt angle δ to be the angle that the projection of $-\dot{M}$ onto the GSE XZ plane 109 makes with the Z axis. (Note that this definition means that positive δ means that the 110 northern magnetic pole is tilted towards the Sun and the southern away from it and neg-111 ative δ means the southern/northern pole is tilted towards/away from the Sun). Because 112 Earth's rotational axis is inclined at 23.44° with respect to the Z axis, this gives an an-113

nual contribution to the variation in δ of $\pm 23.44^{\circ}$ which depends on the fraction of the 114 calendar year, F. The present paper considers data for 1985-2021, the middle of that in-115 terval being 2003. In that year, Earth's geocentric dipole axis made an angle of 10.32° 116 with the rotational axis which gives an additional diurnal variation in δ of this ampli-117 tude, making the total range in δ over the year of $\pm 33.76^{\circ}$. For an eccentric dipole, off-118 sets of the north and south magnetic poles in 2003 were 6.81° and 14.96° , respectively, 119 which gives total ranges of δ of $\pm 30.25^{\circ}$ and $\pm 38.40^{\circ}$ for the north and south poles re-120 spectively. 121

122 Low values of $|\delta|$ form a characteristic pattern called the "McIntosh" or "equinoctial" pattern with F and UT. This pattern is also observed in geomagnetic activity, first 123 reported by McIntosh (1959) and frequently discussed since (for example Berthelier, 1976; 124 de La Sayette & Berthelier, 1996; Cliver et al., 2000; Lockwood, Owens, Barnard, Haines, 125 et al., 2020; Lockwood, McWilliams, et al., 2020; Lockwood et al., 2021). The equinoc-126 tial pattern is most clearly seen in the *am* index, which responds primarily to the sub-127 storm current wedge (Menvielle & Berthelier, 1991). The reason why am is the optimum 128 index for observing this pattern is that it has the most uniform F-UT response pattern 129 of all geomagnetic indices because it is constructed using homogeneous rings of stations 130 in both hemispheres with weighting function corrections to allow for any unavoidable lon-131 gitudinal inhomogeneities in the siting of stations due to oceans (Lockwood et al., 2019). 132

Low δ gives larger solar zenith angles χ at high latitudes which gives lower values 133 in EUV-generated ionospheric conductivity (Moen & Brekke, 1993; Ridley et al., 2004). 134 However, the conductivity pattern depends on δ and not $|\delta|$ and so it is not obvious how 135 conductivities could generate an equinoctial pattern in geomagnetic activity. The pro-136 posal of Lyatsky et al. (2001) and Newell et al. (2002) is that global geomagnetic activ-137 ity is enhanced when the midnight sector of both auroral ovals, where substorms are ini-138 tiated, are in darkness at E-region heights (solar zenith angles χ greater than about 101°) 139 and so have a lower conductivity, and this only occurs when $|\delta|$ is small. Alternatively, 140 the conductivity variation with χ proposed by Nagatsuma (2004) has, due to slant path 141 effects, a minimum at $\chi = 90^{\circ}$ (which would be more common at low $|\delta|$). However, 142 this minimum is not present in the models and observations of Brekke and Moen (1993), 143 Moen and Brekke (1993) and Ridley et al. (2004). 144

It should be noted that, as discussed in the following subsections, EUV-enhanced conductivities in polar regions is far from the only proposed mechanism by which the *F-UT* equinoctial pattern of $|\delta|$ can be imprinted on global geomagnetic activity.

148

1.3 Dipole tilt effects in the geomagnetic tail

The near-Earth tail is orientated with respect to the Earth's magnetic axis whereas the mid-tail and far-tail regions are orientated with respect to the solar wind flow (with a small aberration due to Earth's orbital motion). Consequently, between the near-Earth and the mid-tail regions the tail bends through the "hinge angle" which is very close to being the same as the dipole tilt angle δ . Hence this tail hinge angle also shows the equinoctial pattern.

Kivelson and Hughes (1990) proposed that the hinge angle plays a role in the sta-155 bility of the tail and the triggering of substorm onsets, an idea investigated further by 156 a number of authors (Danilov et al., 2013; Kubyshkina et al., 2015, 2022; Korovinskiy 157 et al., 2018). To fit the observations, substorm occurrence and strength (and hence also 158 global geomagnetic activity) would need to be enhanced when the hinge angle is small 159 160 (i.e., when $|\delta|$ is small). A variant of this idea was proposed by Alexeev et al. (1996) and Ou et al. (2022) who suggested the dipole tilt effect was through a change in the prox-161 imity of the ring current and the closest auroral electrojet. 162

A different mechanism for generating the equinoctial pattern in the geomagnetic 163 tail has been proposed by Lockwood, McWilliams, et al. (2020); Lockwood, Owens, Barnard, 164 Watt, et al. (2020). This uses the fact that the dipole tilt influences how quickly open 165 field lines are appended to the tail because of the shift with δ in the magnetic latitude 166 of the magnetic reconnection site in the dayside magnetopause, as has been modelled in 167 numerical MHD simulations (Park et al., 2006; Hoilijoki et al., 2014; Lockwood, Owens, 168 Barnard, Watt, et al., 2020; Eggington et al., 2020) and also observed in satellite data 169 (Trattner et al., 2012; Zhu et al., 2015; Kitamura et al., 2016). In the hemisphere in which 170 the dipole axis is tipped toward the Sun ($\delta > 0$ for the northern hemisphere), open field 171 lines take longer than those in the other hemisphere or for when $\delta = 0$: this is because 172 they have further to travel and because, initially, the open field lines are moving under 173 the magnetic curvature force against, rather than with, the magnetosheath flow. As a 174 result, a larger fraction of the open flux threads the dayside magnetopause sunward of 175 a given X in the tail in the hemisphere tipped towards the Sun (and hence a smaller frac-176 tion threads the tail lobe at that X). Numerical simulations show that the total field, in 177 both lobes, is smaller for larger $|\delta|$ and so the magnetic shear across the cross-tail cur-178 rent sheet is greatest for $\delta = 0$ and this too yields an equinoctial F-UT pattern (Lockwood, 179 Owens, Barnard, Watt, et al., 2020). This mechanism is supported by the observation 180 that the equinoctial pattern is enhanced by solar wind dynamic pressure which also en-181 182 hances the magnetic shear across the near-Earth cross-tail current sheet by squeezing the near-Earth tail (Lockwood, McWilliams, et al., 2020; Lockwood, Owens, Barnard, 183 Watt, et al., 2020). 184

1.4 Ion-neutral momentum exchange

There are other effects of the Earth's dipole tilt. The dynamics of ionospheric plasma 186 is ordered relative to the geomagnetic pole whereas the dynamics of the neutral thermo-187 spheric gas is ordered relative to the rotational pole. Both ion-neutral and electron-neutral 188 collisions contribute to ionospheric conductivities, but ion-neutral collisions have an ad-189 ditional role in momentum exchange between the ionosphere and thermosphere (specif-190 ically ions because their greater mass means that they carry much greater momentum 191 than electrons). As a result, plasma convection influences thermospheric winds which, 192 in turn influence the deposition of energy because ion-neutral frictional heating depends 193 on the vector difference between the velocities of ions and neutrals. Hence both the wind 194 response and the effect on energy deposition depend on UT (see review in Wang et al., 195 2017). An important factor in these effects is temporal variability in the ionospheric con-196 vection because the greater number densities of neutrals atoms compared to ions, results 197 in the response times of thermospheric winds to changes in ionospheric flow being larger 198 than the response times of ionospheric flows to changes in magnetospheric dynamics (Lockwood 199 et al., 1988; Zou et al., 2021). Förster and Cnossen (2013) noted that the hemispheric 200 intrinsic magnetic field differences were probably more important for polar thermospheric 201 neutral winds than ionospheric plasma convection but can still influence currents, con-202 vection and power dissipation rates in the upper atmosphere and have implications that 203 have been invoked by Chossen et al. (2012), Förster and Chossen (2013) and Laundal 204 et al. (2017). 205

206

185

1.5 The Russell-McPherron effect

The Russell-McPherron (R-M) effect (Russell & McPherron, 1973) is central to understanding the semi-annual variation in geomagnetic activity. A review of the evidence for this mechanism and of its influence has recently been given by Lockwood, Owens, Barnard, Haines, et al. (2020) and Lockwood, McWilliams, et al. (2020). The R-M effect arises because the IMF is ordered, on average, in a solar frame (the Parker Spiral configuration) but coupling into the magnetosphere depends in its orientation relative to Earth's magnetic dipole axis (in a frame such as Geocentric Solar Magnetospheric,

GSM). The most appropriate solar frame is the Geocentric Solar Equatorial (GSEQ). 214 The key effect is that the Earth's dipole tilt means that at the March equinox, negative 215 IMF $[B_Y]_{GSEQ}$ gives a southward IMF component in GSM (hence enhancing solar wind-216 magnetosphere coupling) whereas at the September equinox it is positive $[B_Y]_{GSEQ}$ that 217 does this. Geomagnetic activity shows, very clearly and very strongly, this preference 218 for high geomagnetic activity at one or other equinox, depending on the polarity of the 219 $[B_Y]_{GSEQ}$ component (Zhao & Zong, 2012; Lockwood, Owens, Barnard, Haines, et al., 220 2020; Lockwood, McWilliams, et al., 2020). This confirms the key importance of the R-221 M effect. The diurnal dipole tilt variation due to Earth's rotation means that the Septem-222 ber peak (for $[B_Y]_{GSEQ} > 0$) is at around 10hrs UT (with a minimum around 22 hrs 223 UT) whereas the March peak (for $[B_Y]_{GSEQ} < 0$) is at around 22 hrs UT (with a min-224 imum around 10 hrs UT). 225

226

1.6 Other dipole tilt effects on magnetopause reconnection voltage

The R-M effect has a characteristic F-UT pattern which is quite different to the 227 equinoctial pattern in $|\delta|$. Hence the R-M effect does not generate the equinoctial pat-228 tern. Another proposal to explain the observed equinoctial pattern in geomagnetic ac-229 tivity is that the magnetopause reconnection voltage Φ_D varies with the dipole tilt (Crooker 230 & Siscoe, 1986; Russell et al., 2003). However, (Finch et al., 2008) analysed the F-UT231 patterns in data from a very large number of individual magnetometer stations and showed 232 that the equinoctial pattern arises in the nightside auroral oval and that it was absent 233 absent in data from dayside stations. Similarly, (Lockwood, Owens, Barnard, Haines, 234 et al., 2020) and (Lockwood, McWilliams, et al., 2020) used the mid-latitude $a\sigma$ indices, 235 which cover 6-hour ranges in Magnetic Local Time (MLT) and showed the equinoctial 236 pattern was strongest in the midnight sector but hardly detectable in the noon sector. 237 This argues against the equinoctial pattern being generated by dipole tilt effects on day-238 side magnetopause coupling and the magnetopause reconnection voltage Φ_D . These re-239 sults strongly indicate that the equinoctial pattern in indices such as *am* is not consis-240 tent with dipole tilt modulation of the reconnection rate in the dayside magnetopause. 241 However, this does not mean that such effects do not occur and numerical simulations 242 by global MHD models have found dipole tilt modulation of magnetopause reconnection 243 voltage; however, Figure 7a of Eggington et al. (2020) shows that the modelled Φ_D vari-244 ation with δ is in the wrong sense to explain the equinoctial pattern of enhanced geo-245 magnetic activity. The effect of dipole tilt on the magnetopause reconnection voltage is 246 discussed further in Section 6. 247

248

1.7 Inductive effect of pole motions

Recently another mechanism has been added to this list. This is, in effect, a dif-249 ferent manifestation of the effect of dipole tilt on the evolution of open flux tubes into 250 the tail proposed by Lockwood, Owens, Barnard, Watt, et al. (2020) and that was dis-251 cussed in Section 1.3. Lockwood et al. (2021) have noted that models and observations 252 show that the ionospheric polar caps and auroral ovals undergo almost the same diur-253 nal sunward and antisunward sequence of motion due to Earth's rotation as the geomag-254 netic pole in a geocentric-solar frame (meaning any frame that has an X axis that points 255 from the centre of the Earth to the centre of the Sun, such as GSE, GSM and GSEQ). 256 At first sight the velocities of these motions appear negligible, being smaller than typ-257 ical solar wind flow speeds in the same frame by a factor of order 2×10^{-4} . However, the 258 flow-transverse magnetic field is larger in the ionosphere than in interplanetary space by 259 a factor that is typically 10^4 and hence in terms of electric fields and voltages the pole 260 motions give values that are typically about half those in interplanetary space. 261

As demonstrated by (Kabin et al., 2004), the effect of dipole tilt on the location of the open-closed field line boundary is readily seen in simulations made by numerical, global, MHD models of the magnetosphere. Figure 1 shows simulations by the SWMF

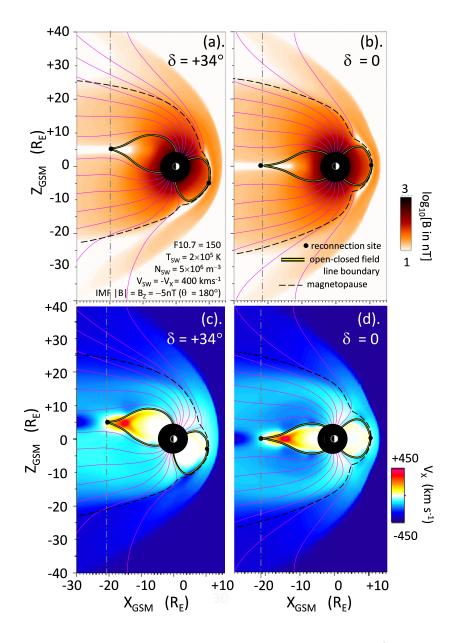


Figure 1. Numerical MHD model results from the SWMF model (version v20140611 - also known as BATSRUS) for run time 90 min in the simulations described by (Lockwood, Owens, Barnard, Watt, et al., 2020). Note these simulations use a geocentric dipole model of the Earth's intrinsic field. The plots show noon-midnight cuts in the GSE XZ plane (Y=0), parts a and b give color contours of the magnetic field strength, B (on a logarithmic scale) and parts c and d give colour contours of the sunward flow speed, V_X . Parts a and c are for a dipole tilt of $\delta = +34^{\circ}$ and parts b and d are for $\delta = 0$. The magnetopause, defined from the plasma beta, flow and the magnetopause current in the Y direction, is shown as dashed lines and reconnection sites, identified by polarity flips in fast flows in the relevant direction, by black dots. The black and yellow line is the open-closed field line boundary. In addition, open magnetic field lines, reconnected 4 min apart, are shown in mauve. The vertical grey dot-dash line is at the X value of the tail reconnection X-line (at Y=0) which is at $X = -20.5R_E$ for $\delta = +34^{\circ}$ and $X = -21R_E$ for $\delta = 0$.

numerical MHD model (version v20140611, also known as BATSRUS) with a geocen-265 tric dipole model of the intrinsic geomagnetic field. The solar wind at (and before) the 266 run time used here (90 min) was steady at $400 km s^{-1}$ with an IMF pointing due south-267 ward in the GSM frame and of magnitude 5nT. The solar wind number density was 3×10^6 268 m^{-3} and the mean ion mass 1.1 amu. Using the empirical relation by Lockwood and McWilliams 269 (2021a), the predicted magnetopause reconnection voltage Φ_D is constant at 56kV. Note 270 that in order to isolate the effects of the dipole tilt angle δ , these simulations were car-271 ried out with two fixed values of δ (0 and 34°) and not one that varies with UT. Note 272 also that the model has been run over 90 min to give a near steady-state with the effect 273 of initial conditions removed. 274

Figure 1 shows noon-midnight cuts (i.e., in the XZ plane of the GSE frame) of the 275 modelled structure in field strength (top panels) and antisunward flow speed (bottom 276 panels) with the left-hand panels for a dipole tilt of $\delta = +34^{\circ}$ and the right-hand pan-277 els for $\delta = 0$. Plots for $\delta = -34^{\circ}$ are not shown because, for the geocentric dipole used. 278 the results for the northern hemisphere are the same as for the southern for $\delta = +34^{\circ}$. 279 The magnetopause is shown by the black dashed line and the X value of the tail recon-280 nection site by the vertical grey dot-dash line. The mauve lines are open field lines that 281 were reconnected 4 minutes apart. The symmetry of the $\delta = 0$ case means that the open 282 field line motion into the tail is the same in the two hemispheres and Figure 1d shows 283 that in both hemispheres open field lines have the same antisunward speed at the mag-284 netopause at all X and that in both hemispheres open field lines take about 12.5 min 285 for the point where they thread the magnetopause to reach the X coordinate of the tail 286 reconnection site $(X \approx -21R_E)$: as a result, in Parts b and d for both hemispheres the 287 two most recently-reconnected field lines shown thread the magnetopause sunward of this 288 X value, and the other 5 of the open field lines shown are appended to the tail lobe by 289 this X: hence roughly $(5/7) \approx 70\%$ of the open flux is appended to both tail lobes at this 290 X in this case. 291

Parts a and c of Figure 1 show how radically the dipole tilt alters this hemispheric 292 symmetry. The field lines in the northern hemisphere reach a flow speed of $V_X = 200 km s^{-1}$ 293 at a GSE latitudes near 80° latitude (approximately 12 min after reconnection) whereas 294 those in the southern hemisphere reach it at near 45° (after only 2.5 min). This is be-295 cause the shift of the magnetopause reconnection site into the southern hemisphere means 296 that for southern hemisphere open field lines the sheath flow and the tension force act 297 together to move open flux tailward whereas initially the sheath flow is opposing the mo-298 tion of northern hemisphere open flux towards the tail. As a result of this hemispheric 299 difference in open flux evolution, only 4 out of the 7 open field lines are inside the tail 300 lobe at the X of the tail reconnection site (approximately 60%) in the northern hemi-301 sphere, whereas in the southern hemisphere this figure is 6 out of 7 (approximately 86%). 302

The tilt of $\delta = 34^{\circ}$ used in Figure 1 is an extreme deviation from $\delta = 0$, slightly larger than the peak-to-peak diurnal variation of the southern ionospheric polar cap over 12 hours of 29.92° (for the pole offset in an eccentric dipole in 2003) and a bit over twice the corresponding diurnal range for the northern polar cap of 13.62°. However it clearly demonstrates how the polar caps move sunward and antisunward with the value of δ . The model runs shown in Figure 1 will be used in Section 5 to check that a best-fit value of a parameter used in this paper (R_X , defined in Section 2.1) is reasonable.

There is also diurnal motion of the ionospheric polar caps in the Y-direction, but this is different in the GSE, GSM and GSEQ frames as they differ in their Y-axis definition; however, they share the same X axis and so the polar cap motion in this direction (towards/away from the Sun) is the same in all these frames and here termed V_P (V_{PN} in the Northern hemisphere, V_{PS} in the southern). Assuming there is no change in the polar cap shape, the voltage across the polar cap generated by these pole motions in all three frames is

$$\phi = V_P B_i d_{PC} \tag{1}$$

where B_i is the ionospheric magnetic field and d_{PC} is the maximum diameter of the po-317 lar cap in the dawn-dusk direction, perpendicular to X. Note that d_{PC} , V_P and B_i are 318 all values for the same altitude. We define V_P as positive for motion towards the Sun 319 which is in the opposite direction to the solar wind flow (which is close to the -X direc-320 tion). For this definition, the voltage ϕ given by Equation 1 is subtracted from that gen-321 erated across the polar cap by the solar wind flow because it is positive when the po-322 lar cap is moving sunward. Using the Expanding-Contracting polar cap model of iono-323 spheric convection excitation (Cowley & Lockwood, 1992; Milan et al., 2021; Lockwood 324 & McWilliams, 2021b; Lockwood & Cowley, 2022), the total voltage across the polar cap 325 allowing for this pole motion effect becomes 326

$$\Phi_{PC} = f_D \Phi_D + f_N \Phi_N + \Phi_V - \phi \tag{2}$$

where Φ_D is the reconnection voltage in the subsolar dayside magnetopause (the rate 327 of production of open flux), Φ_N is the reconnection voltage in the cross-tail current sheet 328 that is between open flux in the tail lobes (the rate of loss of open flux), Φ_V is the "viscous-329 like" voltage induced by all non-reconnection mechanisms of solar wind-magnetosphere 330 interaction. The factors f_D and f_N are the fractions of reconnection voltages (Φ_D and 331 Φ_N , respectively) placed across the maximum diameter of the polar cap. These factors 332 depend upon the shape of the polar cap and how it is changing: for the approximation 333 of a polar cap that remains circular at all times $f_D = f_N = 0.5$ (Lockwood, 1993) but 334 in general the polar cap boundary shape is always evolving (Tulegenov et al., 2023) and 335 so the factors f_D and f_N are not constant. 336

Figure 2 looks at the implications of these pole motions by considering a Faraday 337 loop PASGUC that is fixed in the GSM frame (shown by the vellow dashed line). The 338 segment PC is the polar cap diameter and the voltage across (i.e. the magnetic flux trans-339 fer rate across it) is $\Phi_{PC} = V_i B_i d_{PC}$ where V_i is the plasma and frozen-in field veloc-340 ity across it. The segment SG is just outside the bow shock in interplanetary space (some-341 times referred to as the "Stern Gap") and the voltage across it is $\Phi_{SG} = V_{SW} B_Z d_{SG}$, 342 where V_{SW} is the solar wind speed in the -X direction, B_Z is the interplanetary mag-343 netic field (IMF) component in the GSM Z direction and d_{SG} is the spatial separation 344 of S and G in the GSM Y direction (the width of the Stern gap). The segments of the 345 loop PAS and GUC are the open field lines on the dawn and dusk extremities of the po-346 lar cap and neglecting any field-aligned voltages (that will be very small compared to 347 Φ_{SG} and Φ_{PC}), Faraday's law tells us the difference in the flux transfer rates $\Phi_{SG} - \Phi_{PC}$ 348 is equal to the rate of growth of flux threading the loop PASGUC. Because the solar wind 349 and relevant sheath flow are supersonic and super-Alfvénic, the solar wind flow and volt-350 age Φ_{SG} is not influenced by any change in Φ_{PC} caused by the pole motion. Hence, in 351 addition to reducing the transpolar voltage Φ_{PC} by ϕ , the effect of a sunward pole mo-352 tion $(\phi > 0)$ is to increase the lobe flux by ϕ . 353

Hence the diurnal cycle of sunward and then antisunward pole motion caused by the rotation of the Earth generates a diurnal cycle of decrease then increase of the ionospheric transpolar voltage with an associated cycle of increase and then decrease in the rate at which open flux is added to the tail lobe.

1.8 Universal Time variations

Many of the effects discussed above generate systematic UT variations when a subset of the data are considered but not when averages of all data are considered. For example, the R-M effect generates UT variations if we consider the two polarities of the

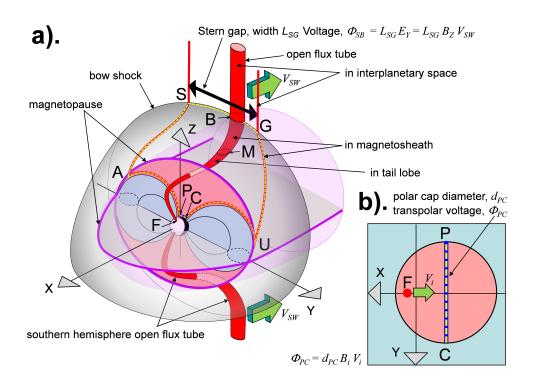


Figure 2. (a). Schematic of inductive decoupling of the "Stern Gap" voltage across open field lines in interplanetary space, Φ_{SG} and the transpolar voltage in the ionosphere Φ_{PC} . The magnetosphere is here viewed from northern middle latitudes in the mid-afternoon sector. The loops PASGUC (shown by the yellow dashed line) and PAUC (enclosing the northern tail lobe cross-section shaded pink) are fixed in the XYZ GSM frame, where P and C are the dawn and dusk extremes of the northern ionospheric polar cap, AP and UC are field-aligned in the magnetosphere, SA and GU are field-aligned in the magnetosheath, SG lies in the bow shock and AU in the tail magnetopause. The red flux tubes are open field lines and the northern-hemisphere tube threads the bow shock at B and the magnetopause at M and has an ionospheric footpoint, F. The solar wind flow is in the -X direction at speed V_{SW} . (b) is a view looking down (in the -Zdirection) on the northern hemisphere polar cap in which the antisunward ionospheric convection velocity of the footpoint F is V_i . After Lockwood and Milan (2023).

IMF separately, but because the distribution of IMF B_Y values is very close to symmetric around zero, the effects of the two polarities almost completely cancel in a full dataset and so the R-M effect does not give a net systematic UT variation if all data are considered.

Indeed, because the dipole tilt angle averages to zero over a full year, this is true for any mechanism that depends linearly on the dipole tilt. However, EUV-induced ionospheric conductivities have a non-linear dependence on solar zenith angle and hence on the dipole tilt. This means that the conductivity effects can give a net systematic UTvariation even after averaging over a whole number of years. However, this depends on location, as demonstrated by Figure 6 of Lockwood and Milan (2023).

The pole-motion effect is different because the diurnal variation of the sunward velocities V_{PN} and V_{PS} are almost independent of the time of year (Lockwood et al., 2021) and so their diurnal effect is not reduced or eliminated by averaging over a whole number of years.

Because the offset of the rotational and magnetic pole in the southern hemisphere 376 is approximately twice that in the northern, the amplitude of the sinusoidal variation 377 in the pole motion speed V_{PS} is approximately twice that in V_{PN} and so the effects on 378 ionospheric transpolar voltage and lobe flux growth rate are roughly twice as large in 379 the south than the north. In addition, whereas the sinusoidal variations would be in ex-380 act antiphase (and of equal amplitude) for a geocentric dipole model of the field (and 381 hence would be equal and opposite and so cancel at any one time), the longitudinal sep-382 aration of the axial poles for an eccentric dipole is not 180° and the hemispheric vari-383 ations are not in exact antiphase as well as being different in amplitude. Thus there is 384 a net UT variation for a global average for an eccentric dipole that is absent for a geo-385 centric dipole. The longitudinal separation of the poles from the Koochak and Fraser-386 Smith (2017b) eccentric dipole model has fallen from 152° in 1985 to 145° in 2015. This 387 means that the phase difference between the sinusoidal variations in V_{PS} and V_{PN} has 388 decreased from 0.85π to 0.81π , compared to the constant value of π for a geocentric dipole. 389

³⁹⁰ 2 The effect of pole motions on substorm growth phases

391

392

2.1 A simple Monte-Carlo model of substorm growth phases and onsets

Lockwood and Milan (2023) have recently proposed a simple Monte-Carlo model 393 of how pole motions influence substorm growth phases and so introduce a UT variation 394 into substorm onset occurrence. This section refines that model slightly and Section 3 395 provides an independent test of the concepts it is based on. In this model, the magne-396 topause reconnection voltage Φ_D is assumed constant and, because we are aiming to re-397 produce average behaviour, we use the overall average $\langle \Phi_D \rangle$ of 24 kV. In Lockwood and 398 Milan (2023), the night ide reconnection voltage Φ_N was also held constant. In the present 399 paper the linear open flux loss found by Lockwood et al. (2023) for times of small |SML|400 is used, with the loss time constant of $\tau_N = 6.8$ hrs $= 2.448 \times 10^4$ sec reported in that 401 paper. Thus the open flux continuity equation for the growth phases simulated is 402

$$dF_{PC}/dt = \Phi_D - \Phi_N = \Phi_D - F_{PC}/\tau_N \tag{3}$$

The questions then arise 'when do growth phases end?' and 'what triggers substorm onset?'. This has been discussed for many years and many mechanisms proposed (Spence, 1996; Lyons et al., 2018; Milan et al., 2019; Tanaka et al., 2021). To determine when onset occurs, the model uses the concept from the analysis of F_{PC} values at the time of onset by Boakes et al. (2009): this does not define the precise time of onset but does give us a usable statistical relationship. These authors found that for values of F_{PC} below ⁴⁰⁹ 0.3*GWb*, the probability of a substorm onset occurring was negligible but that as F_{PC} ⁴¹⁰ rose above this level the probability increased linearly and was undefined above 0.9*GWb*. ⁴¹¹ Lockwood and Milan (2023) took the probability of onset to become unity at $F_{PC} = 1.2$ GWb, ⁴¹² the maximum possible open flux estimated by Mishin and Karavaev (2017). The impli-⁴¹³ cation is that the magnitude of the open flux F_{PC} that causes onset through its effect ⁴¹⁴ on the total lobe flux in the tail and hence the magnitude of the cross-tail current. The ⁴¹⁵ flux in one tail lobe, $[F_{lobe}]_X$, at a given (negative) value of X in the tail, is given by

$$[F_{lobe}]_X = F_{PC} - F_X \tag{4}$$

where F_X is the open flux connected to the ionospheric polar cap in that hemisphere that still threads the dayside magnetopause sunward of X. Differentiating with time t gives

$$d[F_{lobe}]_X/dt = dF_{PC}/dt - dF_X/dt$$
(5)

The pole motion influence on F_X depends on the value of X considered and will decline with distance away from the Earth down the tail. We can allow for this with a factor that depends on X, R_X , which is the ratio $(dF_X/dt)/\phi$,

$$d[F_{lobe}]_X/dt = dF_{PC}/dt - R_X\phi \tag{6}$$

⁴²² The factor R_X will, in general, depend on how much of the open flux was recently ⁴²³ opened and hence the prior history of the voltage Φ_D . However, the constant Φ_D used ⁴²⁴ in this simple model means that R_X will be constant for a given X. Substituting from ⁴²⁵ equation 3 gives

$$d[F_{lobe}]_X/dt = \Phi_D - F_{PC}/\tau_N - R_X\phi \tag{7}$$

⁴²⁶ Note that Equation 7 applies to both hemispheres and that, because of Maxwell's ⁴²⁷ equation $\nabla . \vec{B} = 0$, Φ_D and F_{PC} are the same for both hemispheres, as is the loss time ⁴²⁸ constant τ_N , whereas we need to separately consider $(R_{XN}\phi_N)$ for the northern hemi-⁴²⁹ sphere and $(R_{XS}\phi_S)$ for the southern in order to compute the total tail lobe flux $[F_{tail}]_X$, ⁴³⁰ which is the sum of the north and south lobe fluxes at X, $[F_{lobe}]_{XN}$ and $[F_{lobe}]_{XS}$:

$$d[F_{tail}]_X/dt = d[F_{lobe}]_{XN}/dt + d[F_{lobe}]_{XS}/dt = 2\Phi_D - 2F_{PC}/\tau_N - R_{XN}\phi_N - R_{XS}\phi_S$$
(8)

The survey by Boakes et al. (2009) found that substorm onset probability increased 431 with the open flux F_{PC} . The model of substorm growth phases employed here uses the 432 equivalent of the Boakes et al. (2009) result but also allows for the open magnetic flux 433 that threads the dayside magnetopause, F_X and how it is influenced by the dipole tilt. 434 It is proposed that the probability of onset being triggered primarily depends on the level 435 of $[F_{tail}]_X$, rather than F_{PC} . In order to demonstrate the principle, the ratios (R_{XS} and 436 $(R_{XN}$ are taken to be equal and held constant. The value was varied and the optimum 437 fit to the observed UT variation of substorm onset (see Section 2.3) was found for $(R_{XS} =$ 438 $R_{XN} = 0.15$ for the X coordinate relevant to substorm onset. In Section 3 this value 439 is also shown to be consistent with a superposed epoch analysis of substorms onsets. 440

Because sequences of upstream IMF variation are independent of the phase of Earth's rotation, the model initiates each growth phase at a UT that is selected using a random number generator. The integration of Equation 8 is started from an initial tail lobe flux

(in each lobe) of $F_i = 0.2 GWb$ ($[F_{tail}]_X = 0.4 GWb$) which is consistent with typical 444 quiet time values of F_{PC} . Note that, in reality, this value will vary but that lowering F_i 445 increases the average length of the growth phases but does not influence the distribu-446 tion of onset UTs because the start UT values of growth phases are randomly selected. Using equation 3, the value of F_{PC} throughout the growth phase is also computed and 448 by assuming a circular polar cap this yields the polar cap diameter, d_{PC} (using the equa-449 tion by Lockwood et al. (2023), based on the work of Milan et al. (2021)). This is used 450 in Equation 1 to compute ϕ_N and ϕ_S at each time. The model calculates $[F_{tail}]_X$ ev-451 ery 1 second using Equation 8 and onset is determined to have occurred or not at each 452 time step using a random number generator constrained to select onset occurrence based 453 on the probability set by the $[F_{tail}]_X$ value. Note that there are three improvements in 454 the model used here, compared to that used by Lockwood and Milan (2023): (1) it al-455 lows for the effect of growth in F_{PC} on the open flux loss rate Φ_N and (2) it allows for 456 the effect of changing polar cap diameter d_{PC} on the pole-motion voltage ϕ (equation 457 1) and (3) it allows for the R_X factors. 458

This model is purely a model of substorm growth phases and onset and so cannot 459 reproduce the intervals between onsets, Δt_o , because they also include the durations of 460 the subsequent expansion and recovery phases (or alternatively the period of driven re-461 connection as discussed by Milan et al. (2021)) and any interval of quiet (northward IMF) 462 conditions between the substorms. Also notice that each substorm growth phase in the 463 model starts from the same initial tail flux $2F_i$ and at a randomly-selected UT. Hence 464 the model cannot account for recurrent substorms during periods of persistent south-465 ward IMF, where a growth phase of a substorm starts immediately after the recovery 466 phase of the prior substorm. 467

468 469

2.2 Effects of pole motions on transpolar voltages and the accumulation of magnetic flux in the tail lobes

Figure 3b and 3d show idealised variations that give an indication of how the pole 470 motions influence the transpolar voltage and the accumulation of lobe flux at the X rel-471 evant to onset. This plot is illustrative and for constant values of the reconnection volt-472 ages Φ_D and Φ_N . The value of Φ_N and of the polar cap diameter d_{PC} employed would 473 apply for a polar cap flux of $F_{PC} = 0.54 \ GWb$. The key point is that effects of the pole-474 motions in the two hemispheres are not of equal amplitude nor in perfect antiphase, as 475 they would be for a geocentric dipole. As a result, there is a sinusoidal variation in both 476 the average Φ_{PC} and the average $\Delta[F_{lobe}]_X$ which is the integral of $R_X \phi$ with time. Fig-477 ure 3c is for steady-state ($\Phi_D = \Phi_N$) whereas Figure 3d is for a growing polar cap with 478 $\Phi_D=24$ kV and $\Phi_N=22$ kV. Figure 3d shows that the net effect of the pole motions is 479 to reduce the rate at which flux is added to the tail, compared to the case without pole 480 motions (the dashed black line) between 2.5hrs UT and 14.5hrs UT but to enhance it 481 at all other UTs. 482

483

2.3 The UT distribution of substorm onsets

Figure 4a shows the histograms of the numbers of substorm onsets N_0 in UT bins 484 0.5hrs wide, derived for 1985-2020 (inclusive) from the SML index and using the algo-485 rithm byForsyth et al. (2015) (hereafter FEA). The onset list by Newell and Gjerloev 486 (2011a, 2011b) (hereafter N&G) gives a very similar variation. The total number of sub-487 storm onsets ΣN_o is 88439 for the FEA list and 62532 for the N&G list. Hence the FEA 488 list is including more and smaller events that are not counted as distinct onsets in the 489 490 N&G list. Despite this difference, the distribution in UT is similar in the two cases with a large peak near 12hrs UT. This is broadly reproduced by the simple Monte-Carlo model. 491 as shown by the mauve lines in Figure 4a. In the model, this occurs because the slow-492 ing of the rate of accumulation of tail lobe flux means that more simulated growth phases 493 (that remember were started at randomly-chosen UTs) are reaching the required tail lobe

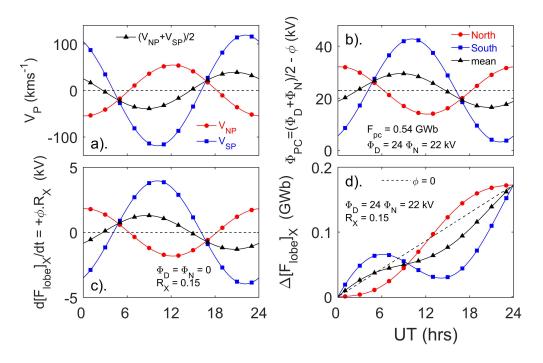


Figure 3. Plots of idealised Universal Time (UT) variations caused by pole motions. In all plots the red lines with red circle symbols are for the northern hemisphere polar cap, blue lines with blue square symbols are for the southern hemisphere polar cap and black lines with triangle symbols are for the global average of the two. Note that the symbols are added to aid readers with impaired colour vision and spaced considerably further apart than the UT resolution of the plots which is 1 min. Variations are based on the eccentric dipole model of Koochak and Fraser-Smith (2017b) for the year 2003. (a) the speed of sunward motion in the GSM frame of the geomagnetic poles at 120 km altitude in the E-region ionosphere, V_{NP} in the north, V_{SP} in the south and the average of the two in black. (b) The polar cap voltages Φ_{PC} from Equations 1 and 2 for constant dayside reconnection voltages of $\Phi_D = 24kV$ and a constant nightside voltage of $\Phi_N = 22$ kV (the value we would expect at low -SML activity levels for an open flux of $F_{PC} = 0.54 GWb$ for the linear loss dependence with time constant $\tau_N = 6.8 hrs$). The viscouslike voltage Φ_V is set to zero. For a circular polar cap this F_{PC} gives a polar cap diameter of d_{PC} = 3.71×10^6 m. (c) The contribution of the pole motions to the rate of accumulation tail lobe flux at X (for $R_X = 0.15$), $d[F_{lobe}]_X/dt = R_X \cdot \phi$ that would be the only change if steady state applied with $\Phi_N = \Phi_N$. (d) The total accumulation of lobe flux $\Delta[F_{lobe}]_X$ for the values of Φ_D , Φ_N in part (b). The dashed black line is for $\phi = 0$.

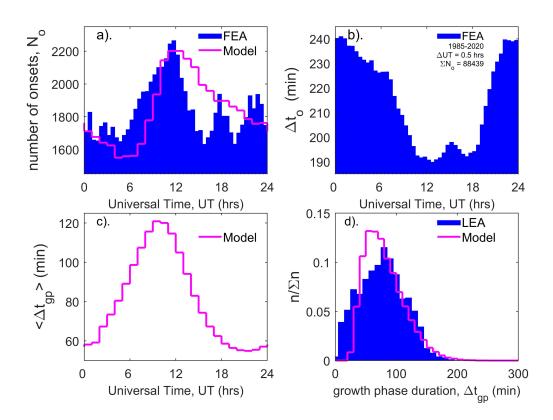


Figure 4. The blue histograms in the top panels show observed distributions with UT of (a) substorm onset times and (b) the interval after the prior onset from the list of such events compiled for 1985-2020 (inclusive) using the *SML* index and the algorithm by Forsyth et al. (2015). These plots both show a marked UT variation. The mauve line in (a) is the variation predicted by the simple Monte-Carlo model described in Section 2.1. (c) Means of the modelled growth phase duration in bins $\Delta UT = 1hr$ wide, $\langle \Delta t_{gp} \rangle$, as a function of UT. (d) The probability distribution of modelled growth phase durations Δt_{gp} (mauve line), where n is the number in bins 10min-wide bins and Σn is the total number (equal to 200,000 for the model simulations). Also shown by the blue histogram is the distribution for $\Sigma n = 368$ observed growth phase durations compiled by Li et al. (2013).

flux to give a high probability of onset at those UTs. After 12 hrs UT this number in 495 a set time falls as the rate of increase in tail flux increases. The observed mean time be-496 tween onsets Δt_{ρ} is shown by the blue histogram in Part b: as discussed in Section 2.1, 497 this cannot be reproduced by the model. Δt_o also shows a marked variation with UT: it decreases from near 4 hrs to close to 3 hrs over the interval 5-12 UT while the num-499 ber of onsets N_o rises. However after 12 UT it remains low even though N_o falls again. 500 This shows that although substorm onsets are rarer by 15 UT, the events that do oc-501 cur tend to recur in short succession. As discussed in Section 2.1, this behaviour can-502 not be captured in the model which restarts each growth phase at a random UT and so 503 it is not surprising the observed variation cannot be reproduced by the model at these 504 UTs in Figure 4a. However, the model does explain how the dipole tilt effect gives the 505 observed peak in onset occurrence at around 12 UT. 506

It is interesting to note what is happening in the growth-phase model. Initially the 507 open flux F_{PC} is low and so the night reconnection voltage Φ_N is considerably smaller 508 than the dayside voltage Φ_D . This means the polar cap flux grows rapidly. However, the 509 rise in F_{PC} increases the value of Φ_N and the rise in F_{PC} slows. Eventually the differ-510 ence between Φ_D and Φ_N becomes small and so the lobe flux variations due to the di-511 urnal pole motions and, in particular, the variations that they cause in $[F_{lobe}]_X$ become 512 significant. Hence although variations in $[F_{lobe}]_X$ due to the pole motions are small they 513 have a significant impact on when the total tail field $([F_{lobe}]_{XN} + [F_{lobe}]_{XS}$ reaches a 514 value that makes the probability of an onset occurring high. 515

Figure 4c presents the UT variation in the mean of the modeled growth phase du-516 rations Δt_{qp} . Unfortunately, we do not have a large observational database to compare 517 these predictions to. However, the plot confirms the above interpretation of the model 518 predictions, with the growth phases coming to an end at around 12 UT having greater 519 durations on average. Figure 4d shows the overall distribution of the 200,000 simulated 520 Δt_{ap} values (in mauve) is quite similar to that of the 368 values observed by Li et al. (2013) 521 (hereafter LEA), shopwn by the blue histogram. LEA divided the onsets into a high, medium 522 and low subsets of the interplanetary electric field, E_{SW} , and showed that the distribu-523 tion of Δt_{ap} values shifted to lower values for the larger E_{SW} cases, as we would expect. 524 The distribution shown by the blue histogram in Figure 4d is the total for all three E_{SW} 525 subsets. The mean value of the LEA distribution is 77 min which is close to the value 526 of 81 min for the modelled distribution. The major difference is that the modelled dis-527 tribution has fewer very short growth phases which suggests that either the initial to-528 tal lobe flux F_i is slightly too low or that the threshold tail flux of 0.6 GWb for the prob-529 ability of onset rising above zero is slightly too high. 530

⁵³¹ 3 Superposed epoch analysis of substorms

Section 2.3 shows that the simple Monte-Carlo model described in section 2.1, whilst 532 not fully modelling the observed UT variation of substorm onsets, provides an impor-533 tant insight into dipole tilt effects. In this section we look for more direct evidence of 534 such an effect using analysis of the variations in the SMU and SML geomagnetic indices 535 and in the magnetopause reconnection voltage estimated from interplanetary measure-536 ments, Φ_D , using a superposed-epoch analysis (also known as Chree analysis or composit-537 ing). This paper presents the plots made using the FEA onset list, but results for the 538 N&G list were similar. 539

Figure 5 presents superposed-epoch plots of the variations in (a) SML, (b) SMUand (c) Φ_D . The epoch time is relative to the times t_o of each of the 88439 substorm onsets in the FEA list for the years 1985 to 2020, inclusive. The mean value and the standard error in the mean are computed at epoch times $(t-t_o)$ between -240 min and +240 min in steps of $\delta t = 1$ min. This was repeated using randomly-selected epoch times t_o as a test of significance: because of the very large numbers of samples these random tests

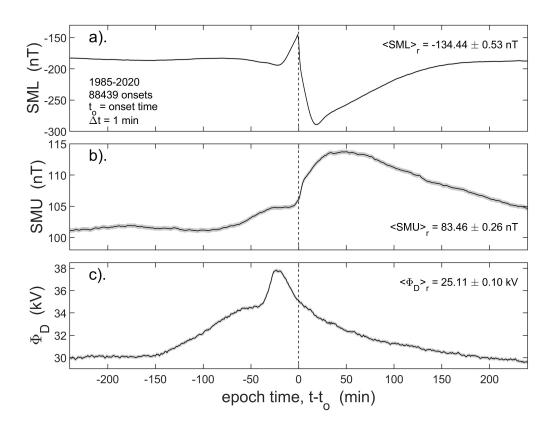


Figure 5. Superposed-epoch plots of substorms using the FEA list of substorm onsets for 1985-2020, inclusive. The mean value is shown as a function of epoch time $(t - t_o)$, where t is the observation time and t_o is the time of onset, for: (a) the *SML* index; (b) the *SMU* index; and (c) the estimated reconnection voltage, Φ_D , lagged by a nominal propagation lag of $\delta t_p =$ 19 min from the nose of the bow shock. The grey areas under the plotted black line are between plus and minus one standard error in the mean, but because of the very large number of samples (88439) these areas are smaller than the line width used for the case of *SML* and cannot be seen.

gave a completely flat variation: these are not shown in Figure 5 as values are considerably lower and so showing them suppresses detail in the plots for the real t_o ; however each plot gives the mean for the randomly-selected epoch times (respectively, $\langle SML \rangle_r$, $\langle SMU \rangle_r$ and $\langle \Phi_D \rangle_r$ in parts a, b and c), plus and minus the value of the mean of the corresponding standard errors. The randomly-selected onset values are shown in Figure 8 which presents the superposed-epoch plots at lower time resolution but over considerably larger ranges of epoch time, $(t - t_o)$.

In Figure 5, the black lines are the mean values over-plotted on top of grey bands 553 that are plus and minus the standard error in the mean. Because of the very large num-554 bers of samples, the gray band is hardly visible, especially for SML. The vertical black 555 dashed line is at epoch time $(t-t_o) = 0$. The Φ_D data have been lagged by a nominal 556 propagation lag of $\delta t_p = 19$ min from the nose of the bow shock. This value is appro-557 priate to the transpolar voltage Φ_{PC} and SML response to Φ_D (Lockwood & McWilliams, 558 2021b), but values near 30-40 min would be more appropriate to the delay before sub-559 storm onset and SML. Hence in relation to onset the Φ_D curve in part c may need to 560 be shifted to the left by an additional lag of about 10-20 min in some considerations. 561

The variation in SML in Figure 5a is as expected with some small changes in the 562 growth phase shortly before onset and a big perturbation to large negative values start-563 ing at onset. It should be remembered the onset times are determined from SML and 564 so we would expect SML to be well ordered by the onset times t_o derived from it. The 565 variation in SMU is also as expected with small increases in the growth phase and then 566 larger positive values after onset. Note that for the randomly-selected values of t_o the 567 values (almost identical at all epoch times) are $\langle SML \rangle_r = -134.44 \pm 0.53$ nT and so larger 568 (less negative) than for the real epoch times and values of $\langle SMU \rangle_r = 83.46 \pm 0.26$ are 569 considerably lower. Hence in all of the 8 hours of epoch time shown, the disturbance lev-570 els of SML and SMU are considerably above the overall average values. Similarly $\langle \Phi_D \rangle_n$ 571 is 25.11 ± 0.10 kV at all epoch times and so considerably lower than for the 8 hour-period 572 around substorm onset. 573

Figure 6 is the same as Figure 5c, but also shows the results for two one hour win-574 dows of the UT of the onset. The windows shown are 15-16 UT (in red) and 02-03 UT575 (in blue). These UT ranges are chosen as they give the maximum deviation either side 576 of the values for all onsets. The means are taken over Δt of 5 min (rather than the 1 min 577 used in Figure 5) because the higher time resolution is not needed and the 1-hour win-578 dows have fewer samples by a factor of roughly 24. The plot clearly shows that, on av-579 erage, larger Φ_D is needed ahead of substorm onsets at 15-16 UT than is needed ahead 580 of onsets at 02-03 UT. The difference between the two is roughly constant at about 4 581 kV at all negative values of $t-t_o$ shown and over that time this is a difference in opened 582 flux of 0.058 GWb which is of order 10% of an average open polar cap flux, F_{PC} (Milan 583 et al., 2008; Boakes et al., 2009). 584

At the start and end of the period shown Φ_D is 30 kV (4.9 kV above average) and 585 starts to rise above this at $t-t_o$ near -150 min. Thus the contribution of enhanced mag-586 netopause reconnection to the enhanced tail flux at onset, on average, begins at this time 587 and increases until about 1 hour before onset (for the nominal propagation lag of δt_p = 588 19 min). It then reaches a plateau for about half an hour before rising to a peak at t-589 $t_o = -25 \min$ (for the nominal $\delta t_p = 19 \min$). This marks the southward turning of the 590 IMF that is usually taken to be the start of the growth phase. However, the plot reveals 591 two levels of "preconditioning" by enhanced Φ_D before this time. The first is the 4.9 kV 592 by which Φ_D is elevated above average values 4 hours ahead of onset. The second is the 593 594 reconnection taking place in the 2 hours before ther inferred southward turning (between $t - t_o = -150$ min and $t - t_o = -30$ min on average). Thus the open flux gained only 595 between the southward turning and onset is not the only contribution to the tail lobe 596 flux at the time of onset. 597

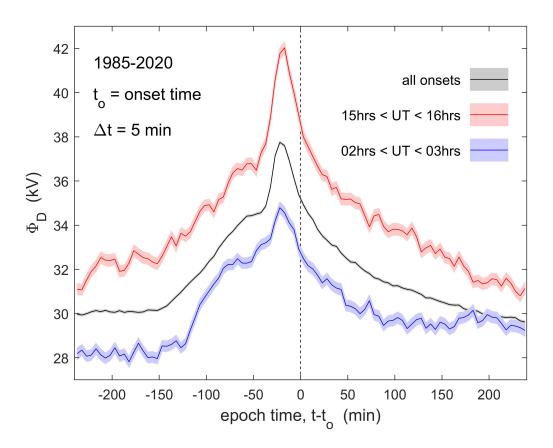


Figure 6. The same as Figure 5 but showing the values for onset UT between 15 and 16 hrs (in red) and between 02 and 03 hrs (in blue). The pink and pale blue shaded areas are plus and minus one standard error in the mean. The averages are here taken over $\Delta t = 5$ min windows in epoch time, $t - t_o$. The black line and grey shaded area is for all UT (also shown in Figure 5c).

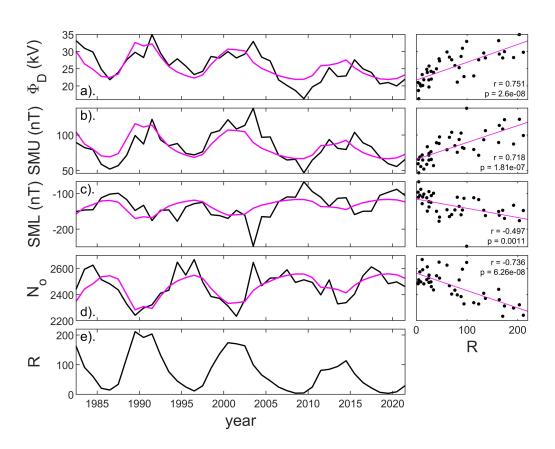


Figure 7. The left-hand column shows the Solar cycle variations in annual means (black lines) of: (a) the estimated magnetopause reconnection voltage, Φ_D ; (b) the *SMU* index; (c) the *SML* index; (d) the number of substorm onsets, N_o and (e) the international sunspot number, R. In panels a-d the mauve lines show the linear regression fit of R to the parameter. The right-hand column gives the scatter plots of the annual means with R, the mauve line being the linear regression fit. In each case, the correlation coefficient r and the p-value of the null hypothesis that there is no correlation are given.

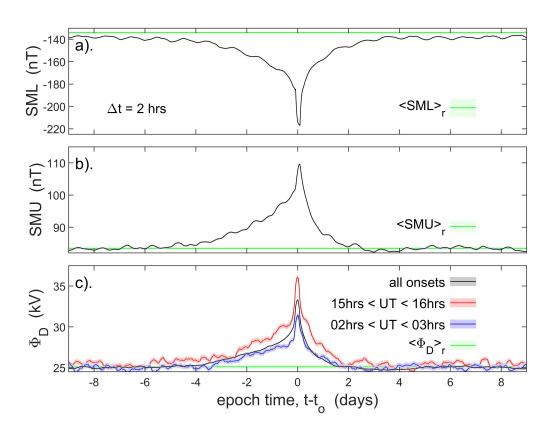


Figure 8. Super-posed epoch plots like those in Figures 5 and 6, but for integration intervals $\Delta t = 2$ hrs and covering epoch times $(t - t_o)$ between -9days and +9 days, where t is the observation time and t_o is the time of onset, for: (a) the *SML* index; (b) the *SMU* index; and (c) the estimated reconnection voltage, Φ_D , lagged by a nominal propagation lag of $\delta t_p = 19$ min from the nose of the bow shock. The black lines are the means for all data and grey areas are plus and minus one standard error in the means. The green lines are for randomly selected epoch times. In Part c, the red and blue lines are means of Φ_D for onset *UT* between 15 and 16 hrs (in red) and between 02 and 03 hrs (in blue): the pink and pale blue shaded areas are plus and minus one standard error in the means.

The first preconditioning, seen as the 4.9 kV by which Φ_D is elevated at $t-t_o =$ 598 -240 min appears be a solar cycle effect; however, Figure 7 shows that this is not the case. 599 Such an effect would arise if onsets were more frequent as higher solar activity, as one 600 might expect, and so the long-term averages of Φ_D , SMU and -SML would all be increased 601 above their overall means. Figure 7 plots the solar cycle variations in annual means for 602 the dataset used here (1985-2021) and although Φ_D , SMU and -SML are all correlated 603 with sunspot number R as we would expect, surprisingly, the number of onsets per year, 604 N_o is anticorrelated with more onsets occurring at sunspot minimum. (Note that SML605 not -SML is plotted in Figure 7 and that the anticorrelation for SML is weaker than the 606 other correlations (larger p value of the null hypothesis) largely because of the anoma-607 lous year 2003 for which the mean SML was exceptionally low. 608

Figure 7 shows that the enhanced Φ_D at the start of Figures 5 and 6 (over the over-609 all mean value which is very close to the value for random selection of epoch times be-610 cause the number of onsets is so high) is not due to the solar cycle variation in the num-611 bers of onsets. Figure 8 looks at the origin of this by extending the interval covered by 612 the superposed epoch study and including the plots for the random selection of epoch 613 times (the green lines with pale green areas showing plus and minus one standard error; 614 however, in most cases these are smaller than the line width and not visible). In these 615 plots the averaging interval was increased to $\Delta t = 2$ hrs. Part a shows that at epoch times 616 well away from onset $t-t_o = -9$ days and $t-t_o = +9$ days, SML is very close to is over-617 all mean and the randomly sampled value $\langle SML \rangle_r$. Part b shows the same is true for 618 SMU, the average vale being found at $(t - t_o) < -5$ days and $(t - t_o) > +2.5$ days. The 619 black line in part c shows that Φ_D is the same as its randomly-selected mean for (t - t)620 t_o <-5 days and that the variation for 15-16 UT is not elevated above that for 02-03 621 UT for $(t - t_0) < -6$ days. Hence the UT variation in the voltage needed to cause an 622 onset depends, to some degree, on a preconditioning (by prior magnetopause reconnec-623 tion) of the substorm growth phase over an interval of about 6 days before the south-624 ward turning that traditionally marks the start of the growth phase. The average effect 625 of that preconditioning can be seen to increase considerably after $(t-t_o) = -2.5$ days. 626 Magnetopause reconnection is likely to continue after onset and only at $(t-t_o) > 2$ days 627 does the mean value of Φ_D fall back to is overall mean value. Hence substorm onsets tend 628 to sit in intervals about 4.5 days long in which Φ_D is enhanced over the overall mean value. 629

It is interesting to note that integrating Φ_D over the interval between the appar-630 ent southward turning of the IMF (at $(t-t_o) = -35$ min, when mean values of Φ_D start 631 to rise sharply to the pre-onset peak) and $(t-t_o) = 10$ min, we find a total of 0.1 GWb 632 of open flux is generated. If we look at the total opened over the preconditioning inter-633 val -4 days $< (t-t_o) < -35$ min, it is 9.3 GWb. Much of this open flux will be lost and 634 Figure 8a shows that average -SML increases with the increasing Φ_D over this interval, 635 indicating enhanced open flux loss by enhanced nightside reconnection. However it is in-636 teresting how little open flux is, on average, generated in the growth phase and how much 637 the occurrence of a substorm onset relies on open flux accumulated during the precon-638 ditioning phase. The growth phase adds the final flux that triggers onset, but the role 639 of prior open flux and preconditioning appears to be very significant. 640

641

3.1 UT variations in the reconnection voltage Φ_D prior to onset

The black line in Figure 9 shows the variation of mean open flux generated in the 642 interval 150 min before onset to 10 min after, ΔF_{ap} , evaluated in bins of UT that are 643 1 hr wide. This is surrounded by a grey area that is plus and minus one standard error 644 in these means. Because the variations of average Φ_D with elapsed time $(t-t_o)$ are very 645 similar in form for all UTs (as in Figure 6), the results are insensitive to the interval of 646 elapsed times that is adopted. Indeed the same form is even seen if take the integral over 647 the whole preconditioning interval of 4 days before onset, as discussed above; however, 648 just as the total fluxes opened in that longer interval are roughly ten times larger than 649

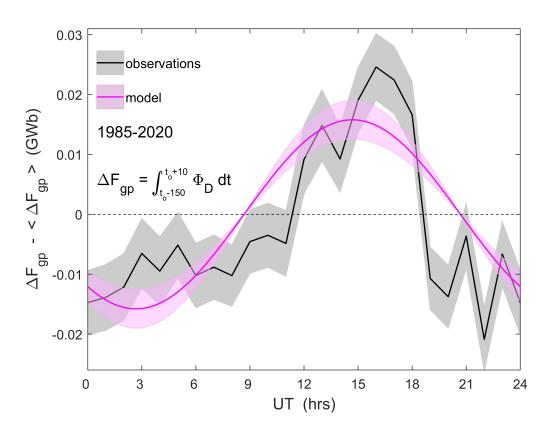


Figure 9. The variation of the open flux ΔF_{gp} generated in the substorm growth phase, taken to be the interval between 150 min before onset and 10 min after (using the nominal propagation lag of $\delta t_p = 19$ min from the nose of the bow shock), which is the integral of Φ_D over that interval. Values are shown as a function of UT for 1-hour intervals of UT and with the mean for all UT, $\langle \Delta F_{gp} \rangle$, subtracted. The black lines are mean values from the data, with the grey area showing plus and minus one standard error in the mean. The mauve line is the model prediction (see section 4) of text).

in the hour before onset (as discussed in the previous section), so the amplitude of the UT variation is also ten times larger.

This plot shows that there is a significant UT variation in the flux that is opened 652 ahead of substorm onsets. The mauve line (with an estimated error shown by the pink 653 area) is the predicted variation for pole motion effect. This uses a value of R_X of 0.15 654 in both hemispheres and was derived in Section 4 using the model used to predict the 655 onset occurrence (see Figure 4a) and described in Section 2.1. The uncertainty of $\pm 20\%$ 656 that is derived in Section 5 from the numerical model predictions shown in Figure 1. It 657 can be seen that this model prediction is not matching all the detail of the observed vari-658 ation, but both the phase and the amplitude of the main component is well reproduced. 659 Hence the UT variations in both the occurrence of onset and the integrated reconnec-660 tion voltage needed to trigger a substorm can be predicted by the model based on the 661 effect of pole motions. 662

$_{663}$ 4 Analysis of UT variation of flux added in substorm growth phase

Figure 10a gives the changes in the lobe fluxes (at X near zero) caused by the mo-664 tions of the poles, ΔF_{lobe} . This is the integral of the pole motion voltage ϕ with time. 665 The colours and symbols are as used in Figure 3. Figure 10b is the variation of the lobe 666 flux at $X = -21R_E$, $\Delta[F_{lobe}]_X$, obtained by multiplying the variations in Part a by R_X 667 = 0.15. The black line is the average of the two which will be half the UT variation of 668 the total lobe flux in the tail, $\Delta[F_{tail}]_X$. The model assumes that it is this total flux that 669 sets the probability of substorm onset occurring. To compensate for the UT variation 670 in $\Delta[F_{tail}]_X$ and give the same probability of onset requires a UT variation in the to-671 tal open flux produced by magnetopause reconnection which is given by the black line 672 in part c of Figure 10. This is the integral of the magnetopause reconnection voltage Φ_D 673 needed, which has been derived from the superposed epoch analysis of the data in Sec-674 tion 3.1. The uncertainty band shown by the grey area is for a $\pm 20\%$ variation in R_X 675 which is derived in the next Section 5. 676

The variation shown in Figure 10c is reproduced in Figure 9 as the mauve line with the uncertainty plotted in pink. It can be seen that the model is reproducing main phase and amplitude of the variation in prior reconnected flux with UT. The amplitude depends on value of R-X of 0.15 which agrees with the simple Monte-Carlo model of onset occurrence and which, in the next section, is found to be a reasonable value using the numerical simulations which gave Figure 1.

5 Numerical modelling the magnetotail response to dipole tilt

This section uses the results of a numerical, global, MHD model of the magnetosphere, shown in Figure 1, to gain some understanding of the factors R_{SX} and R_{NX} in Equation 8.

The simulations used are for tilt angles δ of 0, 34° and -34°. (Note that the use of 687 a geocentric dipole field means that the third simulation for $\delta = -34^{\circ}$ gave identical re-688 sults to $\delta = +34^{\circ}$ but with the north and south hemispheres reversed). All three simu-689 lations were started (at simulation time $t_s=0$) with a large open flux of $F_{PC}=0.85$ GWb 690 which decayed until near steady state was achieved shortly after $t_s=90$ min. The decay 691 was greater for $\delta = \pm 34^{\circ}$ than for $\delta = 0$ largely because the dayside reconnection voltage 692 Φ_D was persistently lower for $\delta = \pm 34^{\circ}$ and the night loss rate was high in both cases 693 because F_{PC} was high. At simulation time $t_s = 90$ min, F_{PC} was 0.583 GWb for $\delta = 0$ 694 and 0.509 GWb for $\delta = \pm 34^{\circ}$, a ratio of 1.145. At this time Φ_D was 90.8 kV for $\delta = 0$ and 695 78.3 kV for $\delta = \pm 34^{\circ}$. Hence the ratio of the reconnection voltages in the two cases was 696 1.160, similar to the ratio for F_{PC} . To allow for the different reconnection rate and make 697 comparisons, all open magnetic fluxes are adjusted so that the F_{PC} is the average of the 698

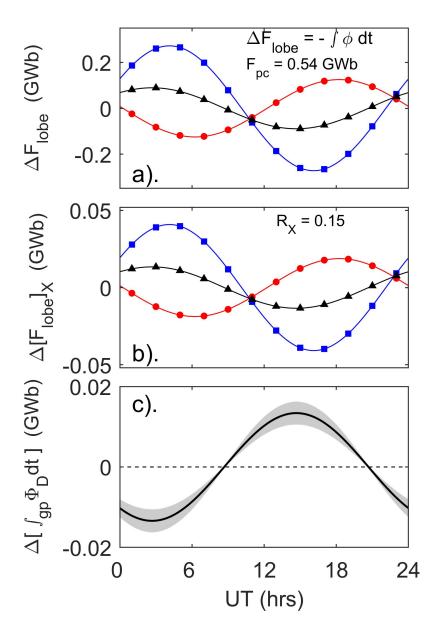


Figure 10. Variations giving the model prediction of the UT variation of flux opened during the growth phase, ΔF_{gp} shown in Figure 9. (a) the flux added to the lobes by the pole motions, ΔF_{lobe} , shown using the same colours and symbols as in Figure 3 (namely: red lines with red circle symbols are for the northern hemisphere polar cap, blue lines with blue square symbols are for the southern hemisphere polar cap and black lines with triangle symbols are for the global average of the two). This is the integral of ϕ with time for an average polar cap flux of F_{PC} of 0.54 GWb (giving a polar cap diameter d_{PC} of 3.73×10^6 m). (b) The variation in $[F_{lobe}]_X$, at the X coordinate of the tail reconnection site ($X = -21R_E$) in the numerical simulation shown in Figure 1. The value of R_X is 0.15, also used to make the model predictions in Figure 4. The variation in the integrated growth phase reconnection voltage needed to offset the variation in the average tail $[F_{lobe}]_X$, show by the black line in part (b). The uncertainty band is derived in Section 5.

 $\delta = 34^{\circ}$ and $\delta = 0$ cases (i.e., 0.546 GWb) which means multiplying the open flux for $\delta = 0$ by 0.937 and that for $\delta = \pm 34^{\circ}$ by 1.073. We also apply these factors to the two parts that add up to the total open flux (Equation 4), F_X and $[F_{lobe}]_X$. The analysis was repeated without these flux normalisation factors and the results for R_X were very similar because their effects on the fluxes F_X , ΔF_{PM} and F_{PC} are very similar. As well as using the mean of the open flux for $\delta = 0$ and $\delta = 34^{\circ}$, the value for each was employed and used to set an uncertainty on the R_X values derived.

The input solar wind parameters in the simulations were held constant and were 706 solar wind speed V_{SW} =400 kms⁻¹, solar wind number density N_{SW} =3×10⁶ m⁻³, mean 707 ion mass $m_{SW}=1.1$ amu, IMF flow-transverse component $B_t=5$ nT and an IMF clock 708 angle in GSM θ =180°. Note that the dayside reconnection voltages of 90.8 kV and 74.3 709 kV generated by the model are both larger than we would expect from these input so-710 lar wind parameters using the empirical relationship by Lockwood and McWilliams (2021a) 711 which gives 56.1 kV for Φ_D but are more similar to the total polar cap voltage Φ_{PC} from 712 the same study (which includes the effect of nightside reconnection and any viscous-like 713 voltage) of 69.6 kV. 714

Figure 1 gives an indication of how dipole tilt effects influence the magnetosphere 715 but it is not the whole story as it only shows the (XZ) plane at Y=0 and does not re-716 veal the behaviour closer to the dawn and dusk flanks. Figure 11 uses the same simu-717 lations to show how the total flux in the tail can be computed. It shows the magnetic 718 field B in cross sections of the tail (YZ planes at various X) in which the minima in B 719 clearly reveal the locations of the magnetopause currents and the cross tail current sep-720 arating the lobes. (Both are also clearly identified from the simulated currents). The mid-721 dle panel is for dipole tilt $\delta = 0$ and the two lobes are symmetrical and the cross-tail 722 current lies at Z=0 at all X and Y. 723

The left-hand panel shows that for dipole tilt angle $\delta = +34^{\circ}$ the cross tail cur-724 rent sheet is warped, such that its displacement to positive Z seen at Y=0 in parts a 725 and c of Figure 1 is a maximum but this displacement in Z is close to zero at the dawn 726 and dusk flank of the tail where it connects to the magnetopause currents. It can be seen 727 that for $\delta = +34^{\circ}$ the field in the southern lobe is considerably enhanced at all X com-728 pared to the $\delta = 0$ case, whereas in the northern hemisphere it is decreased. Because 729 this simulation is for an geocentric dipole field, the southern hemisphere for $\delta = +34^{\circ}$ 730 is identical to the northern hemisphere for $\delta = -34^{\circ}$ (Lockwood, Owens, Barnard, Watt, 731 et al., 2020). 732

In both cases, the field in the tail decreases with increasingly negative X. From the integral of the field threading the cross sections of the tail (the B_X component) we obtain the magnetic flux in each lobe at each x, $[F_{lobe}]_X$. At X below about $-20R_E$ there is no closed flux in the tail and so the decrease in this flux with increasingly negative X is only because of open flux F_X that threads the magnetopause sunward of the X in question.

From equation 4 we can compute the flux threading the magnetopause sunward of X, F_X and this is shown as a function of X in Figure 12a for the northern hemisphere for dipole tilt angles (positive for northern hemisphere tipped towards the Sun) of (red) $\delta = +34^\circ$, (green) $\delta = 0$ and (blue) $\delta = -34^\circ$. This plot shows that the magnitude of the effect on F_X of a tilt towards the Sun is somewhat smaller than a tilt of the same magnitude away from it. Hence the variation in the tail is not linear with δ .

From these variations we can compute the R_X factors. By integration of the definition of R_X with time, we have:

$$R_X = (dF_X/dt)/\phi = F_X/\int \phi dt = F_X/F_{PM} = \Delta F_X/\Delta F_{PM}$$
(9)

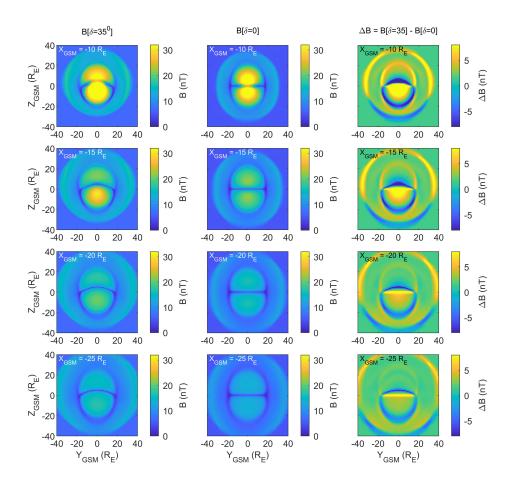


Figure 11. Cross-sections of the tail showing the field strength B in the GSM YZ plane from the simulations shown in Figure 1. From top to bottom the rows are for X of $-10R_E$, $-15R_E$, $-20R_E$, and $-25R_E$. The left-hand column is for dipole tilt angle $\delta = +34^\circ$, the middle column is for $\delta = 0$ and the right-hand column shows the difference between the two, ΔB .

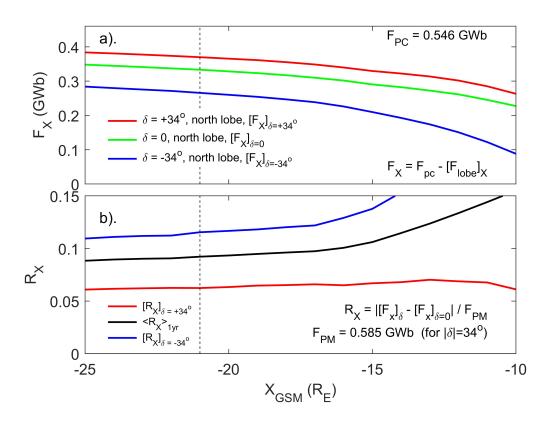


Figure 12. (a). Variation of the fluxes threading the dayside magnetopause F_X with X for a fixed polar cap flux F_{PC} of 0.546 GWb: red, green and blue are for dipole tilt angles (positive for northern hemisphere tipped towards the Sun) of $\delta = +34^{\circ}$, $\delta = 0$ and $\delta = -34^{\circ}$. The X of the tail reconnection site $(-21R_E)$ is shown by the vertical dashed line. (b) The values of R_X derived from Part a for (red) $\delta = +34^{\circ}$ and (blue) $\delta = -34^{\circ}$. The black line is the annual mean of the R_X values that are due to diurnal motions, $\langle R_X \rangle_{1yr}$, the derivation of which is explained in Figure 13.

where in this case we consider the deviation from the $\delta = 0$ case, $\Delta F_X = [F_X]_{\delta} - [F_X]_{\delta=0}$. 747 The corresponding flux ΔF_{PM} is given by $d_{PC}.B_i.\Delta X$ where ΔX is the difference in the 748 X coordinate of the diameter of the polar cap for tilt angles of δ and of $\delta = 0$. This yields 749 $|\Delta F_{PM}|$ of 0.585 GWb for the 34° change in δ . The red lines in Figure 12b gives the val-750 ues of R_X for tilting the polar cap sunward from $\delta = 0$ to $\delta = +34^{\circ}$ (or antisuward the 751 other way) and the blue line the value of R_X for tilting the polar cap sunward from δ 752 = -34° to $\delta = 0$ (or, again, antisuward the other way). The black line gives the average 753 over a whole year of R_X for the daily sunward/antisunward motion, $\langle R_X \rangle_{1ur}$. The deriva-754 tion of this from the simulation results is explained by Figure 13. 755

Figure 13 is for the example X of $-21R_E$. The points in Part a are the values of 756 the flux threading the dayside magnetopause F_X for $\delta = +34^\circ$, $\delta = 0$ and $\delta = -34^\circ$ 757 at this X, as given in Figure 12a. The line is a second order polynomial fit to these points. 758 This has been extended out to $\pm 39^{\circ}$, which is the full range of possible δ values that the 759 south pole can have. The vertical dashed lines mark the range of the annual variation 760 due to Earth's orbital motion ($\pm 23.44^{\circ}$). For each value of δ between the dashed lines, 761 the diurnal variation in δ is added and the diurnal change in F_X (ΔF_X) that it causes 762 is then scaled from the polynomial fit in Part a and the corresponding change in the pole 763 motion flux F_{PM} (ΔF_{PM}) (the integral of ϕ calculated from Equation 1): ΔF_X and ΔF_{PM} 764 are shown in parts b and c, respectively, as a function of the daily mean δ , and the ra-765 tio of the two, (equal to R_X by Equation 9) is shown in Part d. 766

A total of 365 values of R_X were computed for the daily average of δ of each day of the year and the mean taken to give the average value over a full year caused by the diurnal variation. The results show the means are the same for the two hemispheres and equal to 0.092. The analysis was re-run using the F_{PC} of the $\delta = +34^{\circ}$ simulation and then again using that for $\delta = 0$ (rather than the mean of the two which is used in Figures 12 and 13). This yield an uncertainty range in the R_X value of ± 0.013 .

The R_X value is of 0.092 is of the required order of magnitude but is smaller than 773 the 0.15 used and we need to look for potential missing factors of 1.6. There are a num-774 ber of considerations that can, individually or collectively, explain this factor. The val-775 ues of R_X depend on how much recently opened flux is present and so the time history 776 of Φ_D is important: larger fluxes of more-recent opened field lines give a higher F_X for 777 a given F_{PM} . The simulations are for near constant Φ_D whereas in substorm growth phases 778 Φ_D has increased with time, giving a higher fraction F_X/F_{PC} . However, from the time 779 variations of Φ_D shown in Figure 5, this factor gives, at most, a rise by a factor of only 780 about 1.05 in R_X . A bigger factor is the value of the open flux F_{PC} which is only 0.546 781 GWb in the simulations but Boakes et al. (2009) find is typically 0.75-0.9 at the time 782 of onset. The value of F_X is close to being proportional to F_{PC} and, for a circular po-783 lar cap, ϕ (and hence F_{PM}) is proportional to $F_{PC}^{0.5}$. Hence, by Equation 9, R_X is pro-784 portional to $F_{PC}^{0.5}$. This gives a factor of between 1.2-1.3. Another factor is the number 785 density of the solar wind, N_{SW} which controls the magnetosheath density at the day-786 side magnetopause, and hence the Alfvén speed with which newly-opened field lines move 787 over the dayside magnetopause away from the reconnection site. In the simulation, a low 788 value was used $(3 \times 10^6 \text{ m}^3)$ whereas the average value is roughly twice this. Increasing 789 N_{SW} by a factor of 2 would lower the Alfvén speed at the dayside magnetopause by a 790 factor of $2^{0.5} = 1.4$ and this would increase the F_X for a given F_{PC} and δ . This would 791 therefore also increase the R_X . Lastly, the value of $R_X = 0.092$ is derived from the sim-792 ulations for the reconnection X-line position in those simulations at the steady state achieved 793 at simulation time $t_s = 90$ min. As shown in Figure 1, this is at $X = -21R_E$. It is highly probable that the X-line at substorm onset forms closer to the Earth than this and Fig-795 ure 12 shows that the simulations give $R_X = 0.11$ at $X = -15R_E$ and $R_X = 0.12$ at X 796 $= -13R_{E}.$ 797

These considerations mean that the simulations can only be used as an order of magnitude guide but we can conclude that they give R_X values that are reasonably consis-

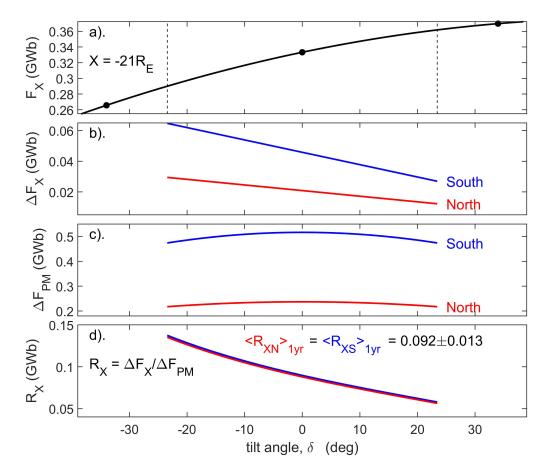


Figure 13. The derivation of the annual mean of the R_X values due to diurnal motions, $\langle R_X \rangle_{1yr}$ (the black line in Figure 12b) shown here for the example X of $-21R_E$. The points in part a are the values of the fluxes threading the dayside magnetopause F_X for δ = $+34^{\circ},$ $\delta = 0$ and $\delta = -34^{\circ}$, as given in Figure 12a and the line is a second order polynomial fit to these points. The plot covers the full potential range of δ (for the southern pole) and the vertical dashed lines mark the range of the annual variation due to Earth's orbital motion. For each value of δ in this range the maximum and minimum δ due to the diurnal variation is considered and the change that the diurnal motions cause in F_X , ΔF_X is scaled from the polynomial fit in part a and shown in b as a function of the daily mean of δ . The corresponding change in the pole motion flux caused by the diurnal motion in the polar cap (the integral of ϕ) is calculated from Equation 1 ΔF_{PM} , and shown in Part c. Part d gives $R_X = \Delta F_X / \Delta F_{PM}$. The mean value over a whole year for both hemispheres is 0.092. An uncertainty is derived using the open flux for each of the two runs, rather than the mean of the two. This yield an uncertainty in idered and the change that the diurnal motions cause in R_X of ± 0.013 .

tent with the empirically-derived value of 0.15, particularly if we take all the factors that are likely to increase the value of R_X into account.

⁸⁰² 6 Discussion and Conclusions

This paper has studied systematic *UT* variations in magnetospheric substorms, using a simple Monte-Carlo model, a global numerical MHD model and 1-minute observations taken over a 34-year interval. All reveal an effect consistent with the effect of diurnal motions of the magnetic poles in a geocentric-solar frame of reference caused by Earth's rotation and the eccentric dipole nature of the intrinsic geomagnetic field.

The analysis has focused on the effect of dipole tilt on the tail flux as an explana-808 tion of UT effects but we should also remember that the num, erical simulations give a 809 dayside reconnection voltage Φ_D that is 16% higher (92kV) for $\delta=0$ than for $\delta=\pm 34^{\circ}$ 810 (78 kV). As discussed in Section 1.6 such a variation in Φ_D with δ has been invoked as 811 the origin of the equinoctial pattern and we need to be clear what this means for aver-812 age variations with UT. By Maxwell's equation $\nabla \vec{B} = 0$, Φ_D must be the same for both 813 hemispheres (as must Φ_N) but note that transpolar voltages Φ_{PC} can differ in the two 814 polar caps because of induction effects associated with field changes in the magnetosphere. 815 for simplicity of explanation, we here consider a geocentric dipole (epoch 2003) and the 816 fact that Φ_D must be the same for the two hemispheres means that the variation of Φ_D 817 with δ must be symmetrical about zero, such that the value for a given tilt δ is the same 818 as that for $-\delta$. The left hand column in Figure 14 shows four model variations of Φ_D 819 with δ that meet this condition. In row (A) there is a minimum in Φ_D at $\delta=0$. The right 820 hand panel shows the F-UT pattern of Φ_D (F being the fraction of a calendar year) that 821 this generates. Averaging over all 365 days of a year at a given UT yields the means $\langle \Phi_D \rangle_F$ 822 shown as a function of UT in the middle panel the middle panel. The F-UT pattern is 823 an "inverse equinoctial" pattern: inverse because the contours of low $|\delta|$ give minima. 824 The variation with UT shows a semi-diurnal form with minima near 11 and 23 UT. 825

Row (**B**) shows the case for a maximum in Φ_D at $\delta=0$. This is the case that was revealed by the numerical simulations discussed in Section 5 and, indeed, the variation has been scaled to the values obtained in that section for $|\delta|=0$ and $|\delta|=\pm 34^{\circ}$. This does give the equinoctial pattern, with low $|\delta|$ giving maxima, as seen for geomagnetic activity. The UT variation again has a semi-diurnal form, but this time it is maxima at 11 hrs UT and 23 hrs UT.

Row (C) shows what happens when the peak Φ_D is at an intermediate δ (here $\pm 17.5^{\circ}$). The *F*-*UT* pattern is like an equinoctial form but is more complex, having a deep minimum embedded within the bands of the maximum Φ_D . The *UT* variation is, however, the same in form as for (**B**).

Row (**D**) shows the results for the variation of Φ_D with δ from the simulation results of Eggington et al. (2020). Thee have been scaled up to the same range as the other variations in the Figure. At first sight we would expect the results to be similar to those in row (**C**) for peak Φ_D at intermediate δ and indeed, the *F*-*UT* plot has similarities but the features are much narrower and sharper. This has a major effect when we average over all *F* and no consistent variation of $\langle \Phi_D \rangle_F$ with *UT* is seen.

Figure 14 shows that variations of Φ_D with δ can give an equinoctial pattern but the diurnal variation seen when data for a given UT are averaged over all F gives two peaks a day. These are at 10.8 hrs UT and 22.8 hrs UT for a geocentric dipole and at 9.0 hrs UT and 21.0 hrs UT for an eccentric dipole (times for 2003). Figure 9 shows the dominant variation is diurnal and not semidiurnal which eliminates variations in the magnetopause reconnection rate as the cause. That being said, the deviations from a pure sinusoidal form in Figure 9 might well be explained by a semi-diurnal oscillation in Φ_D ,

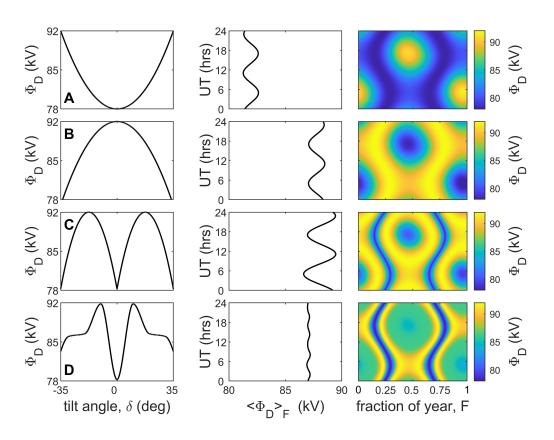


Figure 14. Analysis of the effects of various variations of the magnetopause reconnection voltage, Φ_D , with the tilt angle δ . The left-hand column gives the variation of Φ_D with δ . The right-have column gives the resulting *F*-*UT* pattern of Φ_D (where *F* is the fraction of a calendar year). The middle column gives Φ_D averaged over a year (x-axis) as a function of *UT* (y-axis). The input variations are all scaled between a maximum of 92 kV and a minimum of 78 kV to match the results of the numerical MHD simulations shown in Figures 1, 11 and 12 and a geocentric dipole is used for simplicity. the top row (**A**) is for a minimum Φ_D at δ =0; row (**B**) is for a maximum at δ =0 (the variation consistent with the numerical simulation results) row (**C**) is for a maximum at δ =17.5° and row (**D**) is the variation from the numerical simulations by Eggington et al. (2020) (scaled to the same minimum-to-maximum range as the other panels).

but that would be a considerably smaller amplitude modulation than the dominant diurnal one shown.

Another reason why we can discount the effects of modulation of Φ_D by δ for the 851 effects studied here comes from the superposed epoch plots shown on Figure 8. If the 852 difference between the variations at a given UT were due to semi-diurnal variations in 853 Φ_D , we would expect the superposed epoch variations to show oscillations with a 1-day 854 period. These are not seen. We do note, however, that tilt angle effects on Φ_D can give 855 the equinoctial pattern. That having been said, the same is true of potential tilt angle 856 857 effects of the night reconnection voltage Φ_N , be it through enhanced instability in the tail to substorm onset, i.e. through lowering the tail flux threshold needed for on-858 set to occur - as proposed by Kivelson and Hughes (1990), or through the effect of dipole 859 tilt on the tail field, as modelled by Lockwood, Owens, Barnard, Watt, et al. (2020). 860

On the other hand, the paper has shown that the UT variations are consistent with the diurnal pole motions of an eccentric dipole. Using a simple Monte-Carlo model based on the idea that the probability of onset is raised by the total magnetic flux in both lobes in the near-Earth tail, we can model the observed UT variation in the number of onsets (Figure 4) except the model as yet has no way of including recurrent substorms due to persistent southward IMF and instead re-starts each growth phase at a random time.

This idea (of the probability of substorm onset being raised by the tail lobe field 867 which is modulated by the dipole tilt) is supported by the superposed epoch studies. These 868 clearly show larger magnetopause reconnection voltages are required for onsets at some 869 $UT_{\rm s}$ than at others. Figure 8 shows that the average behaviour is that after a substorm 870 onset the reconnection voltage has fallen back to it average value in about 2 days. How-871 ever, before onset a considerably longer period of enhanced opening of magnetospheric 872 flux is required. The plots (Figures 5 and 8) reveal a rise in Φ_D , on average, of order 30 873 min ahead on an onset. this is consistent with the southward turning that traditionally 874 starts substorm growth phases. However there seems to be two levels of precondition-875 ing before this. The first is an average rise in Φ_D in the 100 min prior to the southward 876 turning. The second is a preconditioning from overall average levels that increases over 877 the prior 6 days. Analysis of solar cycles shows, somewhat surprisingly, substorm onsets 878 are more common at sunspot minimum and hence this cannot be attributed to the vari-879 ation of average solar wind conditions with the sunspot cycle. 880

A theory that allows us to accommodate the effect of pole motions and an eccen-881 tric dipole into magnetospheric dynamics has been presented. In relation to substorm 882 growth phase termination and onsets, the majotr unknown is the extent to which dipole 883 tilts influence the tail and X coordinates that influence onset. This has been allowed for 884 in the present paper with the factor R_X . The Monte-Carlo model of onsets requires $R_X \approx 0.15$, 885 a value that is shown here to agree well with the UT variation found from the super-886 posed epoch studies. A test of this value using a numerical MHD model of the magne-887 to sphere is shown to result in a value near 0.10. However, there are a number of factors 888 that could be invoked to increase this number and make it consistent with the 0.15 value. 889 The present paper does no more than establish that the numerical model simulations show 890 an effect that gives the required diurnal variation with the correct phase, but the am-891 plitude is smaller than needed to fit the observations by a factor of about a third. Fur-892 ther work is needed to establish if indeed $R_X=0.15$ is the correct value. 893

894 **References**

 Alexeev, I. I., Belenkaya, E. S., Kalegaev, V. V., Feldstein, Y. I., & Grafe, A. (1996).
 Magnetic storms and magnetotail currents. Journal of Geophysical Research: Space Physics, 101 (A4), 7737–7747. Retrieved 2022-12-12, from http://doi
 .wiley.com/10.1029/95JA03509 doi: 10.1029/95JA03509

Bartels, J. (1936). The eccentric dipole approximating the Earth's magnetic field. Journal of Geophysical Research, 41(3), 225-250. Retrieved 2023-01-20, from http://doi.wiley.com/10.1029/TE041i003p00225 doi: 10.1029/TE041i003p00225

- Berthelier, A. (1976). Influence of the polarity of the interplanetary magnetic field
 on the annual and the diurnal variations of magnetic activity. Journal of Geophysical Research, 81(25), 4546-4552. Retrieved 2022-12-09, from http://doi
 .wiley.com/10.1029/JA081i025p04546 doi: 10.1029/JA081i025p04546
- Boakes, P. D., Milan, S. E., Abel, G. A., Freeman, M. P., Chisham, G., & Hubert,
 B. (2009). A statistical study of the open magnetic flux content of the magnetosphere at the time of substorm onset. *Geophysical Research Letters*,
 36(4), L04105. Retrieved 2022-10-23, from http://doi.wiley.com/10.1029/
 2008GL037059 doi: 10.1029/2008GL037059
- Boyle, C. B., Reiff, P. H., & Hairston, M. R. (1997). Empirical polar cap potentials. Journal of Geophysical Research: Space Physics, 102(A1), 111–125. Retrieved 2022-12-19, from http://doi.wiley.com/10.1029/96JA01742 doi: 10.1029/ 915 96JA01742
- Brekke, A., & Moen, J. (1993). Observations of high latitude ionospheric conductances. Journal of Atmospheric and Terrestrial Physics, 55 (11-12), 1493-1512.
 Retrieved 2022-12-09, from https://linkinghub.elsevier.com/retrieve/
 pii/002191699390126J doi: 10.1016/0021-9169(93)90126-J
- 920Carter, J. A., Milan, S. E., Paxton, L. J., Anderson, B. J., & Gjerloev, J. (2020).921Height-integrated ionospheric conductances parameterized by interplanetary922magnetic field and substorm phase. Journal of Geophysical Research: Space923Physics, 125(10). Retrieved 2022-11-10, from https://onlinelibrary.wiley924.com/doi/10.1029/2020JA028121
- Cliver, E. W., Kamide, Y., & Ling, A. G. (2000). Mountains versus valleys: Semiannual variation of geomagnetic activity. Journal of Geophysical Research: Space Physics, 105(A2), 2413-2424. Retrieved 2022-11-27, from http://doi.wiley
 .com/10.1029/1999JA900439 doi: 10.1029/1999JA900439
- Cnossen, I., Wiltberger, M., & Ouellette, J. E. (2012). The effects of seasonal and diurnal variations in the Earth's magnetic dipole orientation on solar
 wind-magnetosphere-ionosphere coupling. Journal of Geophysical Research: Space Physics, 117(A11), n/a-n/a. Retrieved 2022-12-19, from http:// doi.wiley.com/10.1029/2012JA017825 doi: 10.1029/2012JA017825
- Cowley, S. W. H., & Lockwood, M. (1992). Excitation and decay of solar winddriven flows in the magnetosphere-ionosphere system. Annales Geophysicae, 10, 103-115. Retrieved 2022-08-18, from https://ui.adsabs.harvard.edu/ abs/1992AnGeo..10..103C (ADS Bibcode: 1992AnGeo..10..103C)
- Coxon, J. C., Milan, S. E., & Anderson, B. J. (2018, March). A review of Birkeland current research using AMPERE. In A. Keiling, O. Marghitu, & M. Wheatland (Eds.), *Geophysical Monograph Series* (pp. 257–278). Hoboken, NJ, USA: John Wiley & Sons, Inc. Retrieved 2023-04-08, from https://onlinelibrary
 .wiley.com/doi/10.1002/9781119324522.ch16 doi: 10.1002/9781119324522
 .ch16
- Crooker, N. U., & Siscoe, G. L. (1986). On the limits of energy transfer through
 dayside merging. Journal of Geophysical Research, 91 (A12), 13393. Retrieved
 2022-12-12, from http://doi.wiley.com/10.1029/JA091iA12p13393 doi: 10
 .1029/JA091iA12p13393
- Danilov, A. A., Krymskii, G. F., & Makarov, G. A. (2013). Geomagnetic

949 950	activity as a reflection of processes in the magnetospheric tail: 1. The source of diurnal and semiannual variations in geomagnetic activity. Ge-
951	omagnetism and Aeronomy, 53(4), 441–447. Retrieved 2022-11-27,
952	from http://link.springer.com/10.1134/S0016793213040051 doi:
953	10.1134/S0016793213040051
954	de La Sayette, P., & Berthelier, A. (1996). The am annual-diurnal variations 1959-
955	1988: A 30-year evaluation. Journal of Geophysical Research: Space Physics,
956	101(A5), 10653-10663. Retrieved 2022-12-09, from http://doi.wiley.com/10
957	.1029/96JA00165 doi: 10.1029/96JA00165
958	Eggington, J. W. B., Eastwood, J. P., Mejnertsen, L., Desai, R. T., & Chittenden,
959	J. P. (2020). Dipole tilt effect on magnetopause reconnection and the steady-
960	state magnetosphere-ionosphere system: Global MHD simulations. Journal
961	of Geophysical Research: Space Physics, 125(7). Retrieved 2022-12-11, from
962	https://onlinelibrary.wiley.com/doi/10.1029/2019JA027510 doi:
963	10.1029/2019JA027510
964	Finch, I. D., Lockwood, M. L., & Rouillard, A. P. (2008). Effects of solar wind mag-
965	netosphere coupling recorded at different geomagnetic latitudes: Separation
966	of directly-driven and storage/release systems. Geophysical Research Letters,
967	35(21), L21105. Retrieved 2022-08-18, from http://doi.wiley.com/10.1029/
968	2008GL035399 doi: 10.1029/2008GL035399
969	Forsyth, C., Rae, I. J., Coxon, J. C., Freeman, M. P., Jackman, C. M., Gjerloev,
970	J., & Fazakerley, A. N. (2015). A new technique for determining Substorm Onsets and Phases from Indices of the Electrojet (SOPHIE). Journal of
971	Onsets and Phases from Indices of the Electrojet (SOPHIE). Journal of Geophysical Research: Space Physics, 120(12), 10,592–10,606. Retrieved
972	2022-12-13, from http://doi.wiley.com/10.1002/2015JA021343 doi:
973 974	10.1002/2015JA021343
	Förster, M., & Cnossen, I. (2013). Upper atmosphere differences between north-
975 976	ern and southern high latitudes: The role of magnetic field asymmetry. <i>Journal</i>
977	of Geophysical Research: Space Physics, 118(9), 5951–5966. Retrieved 2022-
978	12-19, from http://doi.wiley.com/10.1002/jgra.50554 doi: 10.1002/jgra
979	.50554
980	Hairston, M. R., & Heelis, R. A. (1993). High-latitude electric field studies using
981	DMSP data. University of Texas at Dallas, Richardson Center for Space Sci-
982	ences Report. Retrieved 2022-12-19, from https://apps.dtic.mil/sti/pdfs/
983	ADA265032.pdf
984	Hoilijoki, S., Souza, V. M., Walsh, B. M., Janhunen, P., & Palmroth, M. (2014).
985	Magnetopause reconnection and energy conversion as influenced by the dipole
986	tilt and the IMF B_x . Journal of Geophysical Research: Space Physics,
987	119(6), 4484-4494. Retrieved 2022-12-11, from http://doi.wiley.com/
988	10.1002/2013JA019693 doi: 10.1002/2013JA019693
989	Kabin, K., Rankin, R., Rostoker, G., Marchand, R., Rae, I. J., Ridley, A. J., L.,
990	D. D. (2004). Open-closed field line boundary position: A parametric study
991	using an MHD model. Journal of Geophysical Research, 109(A5), A05222.
992	Retrieved 2022-10-27, from http://doi.wiley.com/10.1029/2003JA010168
993	doi: 10.1029/2003JA010168
994	Kitamura, N., Hasegawa, H., Saito, Y., Shinohara, I., Yokota, S., Nagai, T.,
995	Burch, J. L. (2016). Shift of the magnetopause reconnection line to the minter hereignberg under control IME conditions. Costail and MMS ab
996	winter hemisphere under southward IMF conditions: Geotail and MMS ob-
997	servations. <i>Geophysical Research Letters</i> , 43(11), 5581–5588. Retrieved 2022-12-12, from http://doi.wiley.com/10.1002/2016GL069095 doi:
998	10.1002/2016GL069095
999	Kivelson, M. G., & Hughes, W. J. (1990). On the threshold for triggering substorms.
1000 1001	Planetary and Space Science, 38(2), 211–220. Retrieved 2022-11-27, from
1001	https://linkinghub.elsevier.com/retrieve/pii/0032063390900855 doi:
1003	10.1016/0032-0633(90)90085-5

Koochak, Z., & Fraser-Smith, A. C. (2017a). An update on the centered and 1004 eccentric geomagnetic dipoles and their poles for the years 1980–2015. 1005 Earth and Space Science, 4(10), 626–636. Retrieved 2022-10-27, from 1006 https://onlinelibrary.wiley.com/doi/10.1002/2017EA000280 doi: 1007 10.1002/2017EA000280 1008 Koochak, Z., & Fraser-Smith, A. C. (2017b). An update on the centered and 1009 eccentric geomagnetic dipoles and their poles for the years 1980–2015. 1010 Earth and Space Science, 4(10), 626–636. Retrieved 2022-10-27, from 1011 https://onlinelibrary.wiley.com/doi/10.1002/2017EA000280 doi: 1012 10.1002/2017EA000280 1013 Korovinskiy, D. B., Semenov, V. S., Erkaev, N. V., Ivanov, I. B., & Kiehas, 1014 S. A. Current sheet bending as destabilizing factor in magne-(2018).1015 totail dynamics. *Physics of Plasmas*, 25(9), 092901. Retrieved 2022-1016 12-11, from http://aip.scitation.org/doi/10.1063/1.5046175 doi: 1017 10.1063/1.5046175 1018 Kubota, Y., Nagatsuma, T., Den, M., Tanaka, T., & Fujita, S. (2017). Polar cap po-1019 tential saturation during the Bastille Day storm event using global MHD sim-1020 Journal of Geophysical Research: Space Physics, 122(4), 4398–4409. ulation. 1021 Retrieved 2022-12-09, from http://doi.wiley.com/10.1002/2016JA023851 1022 doi: 10.1002/2016JA023851 1023 Kubyshkina, M., Semenov, V., Erkaev, N., Gordeev, E., & Kubyshkin, I. (2022).1024 The asymmetry of magnetospheric configuration and substorms occurrence 1025 rate within a solar activity cycle. In A. Kosterov, N. Bobrov, E. Gordeev, 1026 E. Kulakov, E. Lyskova, & I. Mironova (Eds.), Problems of Geocosmos-2020 1027 (pp. 451–464). Cham: Springer International Publishing. Retrieved 2022-12-11, 1028 from https://link.springer.com/10.1007/978-3-030-91467-7_33 (Se-1029 ries Title: Springer Proceedings in Earth and Environmental Sciences) doi: 1030 10.1007/978-3-030-91467-7_33 1031 Kubyshkina, M., Tsyganenko, N., Semenov, V., Kubyshkina, D., Partamies, N., & 1032 Gordeev, E. (2015). Further evidence for the role of magnetotail current shape 1033 in substorm initiation. Earth, Planets and Space, 67(1), 139. Retrieved 2022-1034 12-11, from http://www.earth-planets-space.com/content/67/1/139 doi: 1035 10.1186/s40623-015-0304-1 1036 Laundal, K. M., Cnossen, I., Milan, S. E., Haaland, S. E., Coxon, J., Pedatella, 1037 N. M., ... Reistad, J. P. (2017). North–south asymmetries in Earth's mag-1038 netic field: Effects on high-latitude geospace. Space Science Reviews, 206(1-4), 1039 Retrieved 2022-12-19, from http://link.springer.com/10.1007/ 225 - 257.1040 s11214-016-0273-0 doi: 10.1007/s11214-016-0273-0 1041 Li, H., Wang, C., & Peng, Z. (2013).Solar wind impacts on growth phase dura-1042 tion and substorm intensity: A statistical approach. Journal of Geophysical 1043 Research: Space Physics, 118(7), 4270–4278. Retrieved 2022-12-21, from 1044 http://doi.wiley.com/10.1002/jgra.50399 doi: 10.1002/jgra.50399 1045 Lockwood, M. (1993).Modelling high-latitude ionosphere for time-varying 1046 plasma convection. IEE Proceedings H Microwaves, Antennas and Propa-1047 qation, 140(2), 91.Retrieved 2022-08-18, from https://digital-library 1048 .theiet.org/content/journals/10.1049/ip-h-2.1993.0015 doi 1049 10.1049/ip-h-2.1993.0015 1050 Lockwood, M., Chambodut, A., Finch, I. D., Barnard, L. A., Owens, M. J., & 1051 Haines, C. (2019).Time-of-day/time-of-year response functions of plane-1052 tary geomagnetic indices. Journal of Space Weather and Space Climate, 9, 1053 Retrieved 2022-08-18, from https://www.swsc-journal.org/10.1051/ A20. 1054 swsc/2019017 doi: 10.1051/swsc/2019017 1055 Lockwood, M., Cowley, S., Todd, H., Willis, D., & Clauer, C. (1988).Ion 1056 flows and heating at a contracting polar-cap boundary. Planetary and 1057 Retrieved 2022-08-18, from https:// Space Science, 36(11), 1229-1253. 1058

1059 1060	linkinghub.elsevier.com/retrieve/pii/0032063388900761 doi: 10.1016/0032-0633(88)90076-1
1061	Lockwood, M., & Cowley, S. W. H. (2022). Magnetosphere-Ionosphere Cou-
1062	pling: Implications of Non-Equilibrium Conditions. Frontiers in Astron-
1063	omy and Space Sciences, 9, 908571. Retrieved 2022-08-18, from https://
1064	www.frontiersin.org/articles/10.3389/fspas.2022.908571/full doi:
1065	10.3389/fspas.2022.908571
1066	Lockwood, M., Haines, C., Barnard, L. A., Owens, M. J., Scott, C. J., Cham-
1067	bodut, A., & McWilliams, K. A. (2021). Semi-annual, annual and Uni-
1068	versal Time variations in the magnetosphere and in geomagnetic activ-
1069	ity: 4. Polar cap motions and origins of the Universal Time effect. Jour-
1070	nal of Space Weather and Space Climate, 11, 15. Retrieved 2022-08-18,
1071	from https://www.swsc-journal.org/10.1051/swsc/2020077 doi:
1072	10.1051/swsc/2020077
1073	Lockwood, M., & McWilliams, K. A. (2021a). On optimum solar wind-
1074	magnetosphere coupling functions for transpolar voltage and planetary
1075	geomagnetic activity. Journal of Geophysical Research: Space Physics,
1076	126(12). Retrieved 2022-05-28, from https://onlinelibrary.wiley.com/
1077	doi/10.1029/2021JA029946 doi: 10.1029/2021JA029946
1078	Lockwood, M., & McWilliams, K. A. (2021b). A survey of 25 years' transpolar volt-
1079	age data from the SuperDARN radar network and the expanding-contracting
1080	polar cap model. Journal of Geophysical Research: Space Physics, 126(9). Re-
1081	trieved 2022-08-18, from https://onlinelibrary.wiley.com/doi/10.1029/
1082	2021JA029554 doi: 10.1029/2021JA029554
1083	Lockwood, M., McWilliams, K. A., Owens, M. J., Barnard, L. A., Watt, C. E.,
1084	Scott, C. J., Coxon, J. C. (2020). Semi-annual, annual and Universal Time
1085	variations in the magnetosphere and in geomagnetic activity: 2. Response to solar wind power input and relationships with solar wind dynamic pressure
1086 1087	and magnetospheric flux transport. Journal of Space Weather and Space Cli-
1088	mate, 10, 30. Retrieved 2022-08-18, from https://www.swsc-journal.org/
1089	10.1051/swsc/2020033 doi: 10.1051/swsc/2020033
1090	Lockwood, M., & Milan, S. (2023). Universal time variations in the magneto-
1091	sphere. Frontiers in Astronomy and Space Sciences, 10(9), 1139295. Re-
1092	trieved 2023-02-16, from https://www.frontiersin.org/articles/10.3389/
1093	fspas.2023.1139295/full doi: 10.3389/fspas.2023.1139295
1094	Lockwood, M., Owens, M., & Barnard, L. (2023). Universal Time variations in the
1095	magnetosphere and the effect of CME arrival time: Analysis of the February
1096	2022 event that led to the loss of Starlink satellites. J. Geophys. Res. Space
1097	Science, submitted. Retrieved 2023-01-05, from https://doi.org/10.1002/
1098	essoar.10512909.1 doi: 10.1002/essoar.10512909.1
1099	Lockwood, M., Owens, M. J., Barnard, L. A., Haines, C., Scott, C. J., McWilliams,
1100	K. A., & Coxon, J. C. (2020). Semi-annual, annual and Universal Time vari-
1101	ations in the magnetosphere and in geomagnetic activity: 1. Geomagnetic
1102	data. Journal of Space Weather and Space Climate, 10, 23. Retrieved 2022-
1103	08-18, from https://www.swsc-journal.org/10.1051/swsc/2020023 doi:
1104	10.1051/swsc/2020023
1105	Lockwood, M., Owens, M. J., Barnard, L. A., Watt, C. E., Scott, C. J., Coxon,
1106	J. C., & McWilliams, K. A. (2020). Semi-annual, annual and Universal Time
1107	variations in the magnetosphere and in geomagnetic activity: 3. Modelling.
1108	Journal of Space Weather and Space Climate, 10, 61. Retrieved 2022-08-
1109	18, from https://www.swsc-journal.org/10.1051/swsc/2020062 doi: 10.1051/swsc/2020062
1110	Lyatsky, W., Newell, P. T., & Hamza, A. (2001). Solar illumination as cause of
1111	the equinoctial preference for geomagnetic activity. <i>Geophysical Research Let-</i>
1112 1113	the equinoctial preference for geomagnetic activity. Geophysical Research Let- ters, 28(12), 2353–2356. Retrieved 2022-11-27, from http://doi.wiley.com/
1113	(12), 2000 2000. Removed 2022 II 21, non http://doi.witey.com/

1114	10.1029/2000GL012803 doi: 10.1029/2000GL012803
1115	Lyons, L. R., Zou, Y., Nishimura, Y., Gallardo-Lacourt, B., Angelopulos, V., &
1116	Donovan, E. F. (2018). Stormtime substorm onsets: occurrence and flow chan-
1117	nel triggering. Earth, Planets and Space, 70(1), 81. Retrieved 2022-12-19, from
1118	https://earth-planets-space.springeropen.com/articles/10.1186/
1119	s40623-018-0857-x doi: 10.1186/s40623-018-0857-x
1120	Mayaud, PN. (1972). The aa indices: A 100-year series characterizing the magnetic
1121	activity. J. Geophys. Res., 77(34), 6870-6874. Retrieved from https://doi
1122	.org/10.1029/ja077i034p06870 doi: 10.1029/ja077i034p06870
1123	McIntosh, D. (1959). On the annual variation of magnetic disturbance. Philo-
1124	sophical Transactions of the Royal Society of London. Series A, Mathemati-
1125	cal and Physical Sciences, 251(1001), 525–552. Retrieved 2022-12-09, from
1126	https://royalsocietypublishing.org/doi/10.1098/rsta.1959.0010 doi:
1127	10.1098/rsta.1959.0010
1128	Menvielle, M., & Berthelier, A. (1991). The K-derived planetary indices: Descrip-
1129	tion and availability. <i>Reviews of Geophysics</i> , 29(3), 415. Retrieved 2022-12-12,
1120	from http://doi.wiley.com/10.1029/91RG00994 doi: 10.1029/91RG00994
1131	Milan, S. E., Boakes, P. D., & Hubert, B. (2008). Response of the expand-
1131	ing/contracting polar cap to weak and strong solar wind driving: Implications
1132	for substorm onset. Journal of Geophysical Research: Space Physics, 113(A9),
1133	n/a-n/a. Retrieved 2022-10-23, from http://doi.wiley.com/10.1029/
1135	2008JA013340 doi: 10.1029/2008JA013340
1136	Milan, S. E., Carter, J. A., Sangha, H., Bower, G. E., & Anderson, B. J. (2021).
1130	Magnetospheric flux throughput in the Dungey cycle: Identification of con-
1138	vection state during 2010. Journal of Geophysical Research: Space Physics,
1139	126(2), e2020JA028437. Retrieved from https://agupubs.onlinelibrary
1140	.wiley.com/doi/abs/10.1029/2020JA028437 doi: https://doi.org/10.1029/
1141	2020JA028437
1141	2020JA028437 Milan, S. E., Walach, M., Carter, J. A., Sangha, H., & Anderson, B. J. (2019).
1142	Milan, S. E., Walach, M., Carter, J. A., Sangha, H., & Anderson, B. J. (2019).
1142 1143	Milan, S. E., Walach, M., Carter, J. A., Sangha, H., & Anderson, B. J. (2019). Substorm onset latitude and the steadiness of magnetospheric convection.
1142	 Milan, S. E., Walach, M., Carter, J. A., Sangha, H., & Anderson, B. J. (2019). Substorm onset latitude and the steadiness of magnetospheric convection. Journal of Geophysical Research: Space Physics, 124(3), 1738–1752. Retrieved
1142 1143 1144	 Milan, S. E., Walach, M., Carter, J. A., Sangha, H., & Anderson, B. J. (2019). Substorm onset latitude and the steadiness of magnetospheric convection. Journal of Geophysical Research: Space Physics, 124(3), 1738–1752. Retrieved 2022-12-19, from https://onlinelibrary.wiley.com/doi/abs/10.1029/
1142 1143 1144 1145	 Milan, S. E., Walach, M., Carter, J. A., Sangha, H., & Anderson, B. J. (2019). Substorm onset latitude and the steadiness of magnetospheric convection. <i>Journal of Geophysical Research: Space Physics</i>, 124(3), 1738–1752. Retrieved 2022-12-19, from https://onlinelibrary.wiley.com/doi/abs/10.1029/ 2018JA025969 doi: 10.1029/2018JA025969
1142 1143 1144 1145 1146	 Milan, S. E., Walach, M., Carter, J. A., Sangha, H., & Anderson, B. J. (2019). Substorm onset latitude and the steadiness of magnetospheric convection. Journal of Geophysical Research: Space Physics, 124 (3), 1738–1752. Retrieved 2022-12-19, from https://onlinelibrary.wiley.com/doi/abs/10.1029/ 2018JA025969 doi: 10.1029/2018JA025969 Mishin, V., & Karavaev, Y. (2017). Saturation of the magnetosphere dur-
1142 1143 1144 1145 1146 1147	 Milan, S. E., Walach, M., Carter, J. A., Sangha, H., & Anderson, B. J. (2019). Substorm onset latitude and the steadiness of magnetospheric convection. Journal of Geophysical Research: Space Physics, 124 (3), 1738–1752. Retrieved 2022-12-19, from https://onlinelibrary.wiley.com/doi/abs/10.1029/ 2018JA025969 doi: 10.1029/2018JA025969 Mishin, V., & Karavaev, Y. (2017). Saturation of the magnetosphere dur- ing superstorms: New results from the magnetogram inversion technique.
1142 1143 1144 1145 1146 1147 1148	 Milan, S. E., Walach, M., Carter, J. A., Sangha, H., & Anderson, B. J. (2019). Substorm onset latitude and the steadiness of magnetospheric convection. Journal of Geophysical Research: Space Physics, 124 (3), 1738–1752. Retrieved 2022-12-19, from https://onlinelibrary.wiley.com/doi/abs/10.1029/ 2018JA025969 doi: 10.1029/2018JA025969 Mishin, V., & Karavaev, Y. (2017). Saturation of the magnetosphere dur-
1142 1143 1144 1145 1146 1147 1148 1149	 Milan, S. E., Walach, M., Carter, J. A., Sangha, H., & Anderson, B. J. (2019). Substorm onset latitude and the steadiness of magnetospheric convection. Journal of Geophysical Research: Space Physics, 124(3), 1738–1752. Retrieved 2022-12-19, from https://onlinelibrary.wiley.com/doi/abs/10.1029/ 2018JA025969 doi: 10.1029/2018JA025969 Mishin, V., & Karavaev, Y. (2017). Saturation of the magnetosphere dur- ing superstorms: New results from the magnetogram inversion technique. Solar-Terrestrial Physics, 3(3), 28–36. Retrieved 2022-10-28, from http:// naukaru.ru/en/nauka/article/18490/view doi: 10.12737/stp-33201704
1142 1143 1144 1145 1146 1147 1148 1149 1150	 Milan, S. E., Walach, M., Carter, J. A., Sangha, H., & Anderson, B. J. (2019). Substorm onset latitude and the steadiness of magnetospheric convection. Journal of Geophysical Research: Space Physics, 124(3), 1738–1752. Retrieved 2022-12-19, from https://onlinelibrary.wiley.com/doi/abs/10.1029/ 2018JA025969 doi: 10.1029/2018JA025969 Mishin, V., & Karavaev, Y. (2017). Saturation of the magnetosphere dur- ing superstorms: New results from the magnetogram inversion technique. Solar-Terrestrial Physics, 3(3), 28–36. Retrieved 2022-10-28, from http:// naukaru.ru/en/nauka/article/18490/view doi: 10.12737/stp-33201704 Moen, J., & Brekke, A. (1993). The solar flux influence on quiet time conductances
1142 1143 1144 1145 1146 1147 1148 1149 1150	 Milan, S. E., Walach, M., Carter, J. A., Sangha, H., & Anderson, B. J. (2019). Substorm onset latitude and the steadiness of magnetospheric convection. Journal of Geophysical Research: Space Physics, 124 (3), 1738–1752. Retrieved 2022-12-19, from https://onlinelibrary.wiley.com/doi/abs/10.1029/ 2018JA025969 doi: 10.1029/2018JA025969 Mishin, V., & Karavaev, Y. (2017). Saturation of the magnetosphere dur- ing superstorms: New results from the magnetogram inversion technique. Solar-Terrestrial Physics, 3(3), 28–36. Retrieved 2022-10-28, from http:// naukaru.ru/en/nauka/article/18490/view doi: 10.12737/stp-33201704 Moen, J., & Brekke, A. (1993). The solar flux influence on quiet time conductances in the auroral ionosphere. Geophysical Research Letters, 20(10), 971-974. Re-
1142 1143 1144 1145 1146 1147 1148 1149 1150 1151	 Milan, S. E., Walach, M., Carter, J. A., Sangha, H., & Anderson, B. J. (2019). Substorm onset latitude and the steadiness of magnetospheric convection. Journal of Geophysical Research: Space Physics, 124(3), 1738-1752. Retrieved 2022-12-19, from https://onlinelibrary.wiley.com/doi/abs/10.1029/ 2018JA025969 doi: 10.1029/2018JA025969 Mishin, V., & Karavaev, Y. (2017). Saturation of the magnetosphere dur- ing superstorms: New results from the magnetogram inversion technique. Solar-Terrestrial Physics, 3(3), 28-36. Retrieved 2022-10-28, from http:// naukaru.ru/en/nauka/article/18490/view doi: 10.12737/stp-33201704 Moen, J., & Brekke, A. (1993). The solar flux influence on quiet time conductances in the auroral ionosphere. Geophysical Research Letters, 20(10), 971-974. Re- trieved 2022-12-19, from https://agupubs.onlinelibrary.wiley.com/doi/
1142 1143 1144 1145 1146 1147 1148 1149 1150 1151 1152	 Milan, S. E., Walach, M., Carter, J. A., Sangha, H., & Anderson, B. J. (2019). Substorm onset latitude and the steadiness of magnetospheric convection. Journal of Geophysical Research: Space Physics, 124(3), 1738–1752. Retrieved 2022-12-19, from https://onlinelibrary.wiley.com/doi/abs/10.1029/ 2018JA025969 doi: 10.1029/2018JA025969 Mishin, V., & Karavaev, Y. (2017). Saturation of the magnetosphere dur- ing superstorms: New results from the magnetogram inversion technique. Solar-Terrestrial Physics, 3(3), 28–36. Retrieved 2022-10-28, from http:// naukaru.ru/en/nauka/article/18490/view doi: 10.12737/stp-33201704 Moen, J., & Brekke, A. (1993). The solar flux influence on quiet time conductances in the auroral ionosphere. Geophysical Research Letters, 20(10), 971-974. Re- trieved 2022-12-19, from https://agupubs.onlinelibrary.wiley.com/doi/ abs/10.1029/92GL02109 doi: https://doi.org/10.1029/92GL02109
1142 1143 1144 1145 1146 1147 1148 1149 1150 1151 1152 1153 1154	 Milan, S. E., Walach, M., Carter, J. A., Sangha, H., & Anderson, B. J. (2019). Substorm onset latitude and the steadiness of magnetospheric convection. Journal of Geophysical Research: Space Physics, 124(3), 1738–1752. Retrieved 2022-12-19, from https://onlinelibrary.wiley.com/doi/abs/10.1029/ 2018JA025969 doi: 10.1029/2018JA025969 Mishin, V., & Karavaev, Y. (2017). Saturation of the magnetosphere dur- ing superstorms: New results from the magnetogram inversion technique. Solar-Terrestrial Physics, 3(3), 28–36. Retrieved 2022-10-28, from http:// naukaru.ru/en/nauka/article/18490/view doi: 10.12737/stp-33201704 Moen, J., & Brekke, A. (1993). The solar flux influence on quiet time conductances in the auroral ionosphere. Geophysical Research Letters, 20(10), 971-974. Re- trieved 2022-12-19, from https://agupubs.onlinelibrary.wiley.com/doi/ abs/10.1029/92GL02109 doi: https://doi.org/10.1029/92GL02109 Nagatsuma, T. (2004). Conductivity dependence of cross-polar potential saturation.
1142 1143 1144 1145 1146 1147 1148 1149 1150 1151 1152 1153 1154	 Milan, S. E., Walach, M., Carter, J. A., Sangha, H., & Anderson, B. J. (2019). Substorm onset latitude and the steadiness of magnetospheric convection. Journal of Geophysical Research: Space Physics, 124(3), 1738–1752. Retrieved 2022-12-19, from https://onlinelibrary.wiley.com/doi/abs/10.1029/ 2018JA025969 doi: 10.1029/2018JA025969 Mishin, V., & Karavaev, Y. (2017). Saturation of the magnetosphere dur- ing superstorms: New results from the magnetogram inversion technique. Solar-Terrestrial Physics, 3(3), 28–36. Retrieved 2022-10-28, from http:// naukaru.ru/en/nauka/article/18490/view doi: 10.12737/stp-33201704 Moen, J., & Brekke, A. (1993). The solar flux influence on quiet time conductances in the auroral ionosphere. Geophysical Research Letters, 20(10), 971-974. Re- trieved 2022-12-19, from https://agupubs.onlinelibrary.wiley.com/doi/ abs/10.1029/92GL02109 doi: https://doi.org/10.1029/92GL02109 Nagatsuma, T. (2004). Conductivity dependence of cross-polar potential saturation. Journal of Geophysical Research: Space Physics, 109(A4). Retrieved 2022-12-
1142 1143 1144 1145 1146 1147 1148 1149 1150 1151 1152 1153 1154 1155	 Milan, S. E., Walach, M., Carter, J. A., Sangha, H., & Anderson, B. J. (2019). Substorm onset latitude and the steadiness of magnetospheric convection. Journal of Geophysical Research: Space Physics, 124(3), 1738–1752. Retrieved 2022-12-19, from https://onlinelibrary.wiley.com/doi/abs/10.1029/ 2018JA025969 doi: 10.1029/2018JA025969 Mishin, V., & Karavaev, Y. (2017). Saturation of the magnetosphere dur- ing superstorms: New results from the magnetogram inversion technique. Solar-Terrestrial Physics, 3(3), 28–36. Retrieved 2022-10-28, from http:// naukaru.ru/en/nauka/article/18490/view doi: 10.12737/stp-33201704 Moen, J., & Brekke, A. (1993). The solar flux influence on quiet time conductances in the auroral ionosphere. Geophysical Research Letters, 20(10), 971-974. Re- trieved 2022-12-19, from https://agupubs.onlinelibrary.wiley.com/doi/ abs/10.1029/92GL02109 doi: https://doi.org/10.1029/92GL02109 Nagatsuma, T. (2004). Conductivity dependence of cross-polar potential saturation.
1142 1143 1144 1145 1146 1147 1148 1149 1150 1151 1152 1153 1154 1155 1156	 Milan, S. E., Walach, M., Carter, J. A., Sangha, H., & Anderson, B. J. (2019). Substorm onset latitude and the steadiness of magnetospheric convection. Journal of Geophysical Research: Space Physics, 124(3), 1738–1752. Retrieved 2022-12-19, from https://onlinelibrary.wiley.com/doi/abs/10.1029/ 2018JA025969 doi: 10.1029/2018JA025969 Mishin, V., & Karavaev, Y. (2017). Saturation of the magnetosphere dur- ing superstorms: New results from the magnetogram inversion technique. Solar-Terrestrial Physics, 3(3), 28–36. Retrieved 2022-10-28, from http:// naukaru.ru/en/nauka/article/18490/view doi: 10.12737/stp-33201704 Moen, J., & Brekke, A. (1993). The solar flux influence on quiet time conductances in the auroral ionosphere. Geophysical Research Letters, 20(10), 971-974. Re- trieved 2022-12-19, from https://agupubs.onlinelibrary.wiley.com/doi/ abs/10.1029/92GL02109 doi: https://doi.org/10.1029/92GL02109 Nagatsuma, T. (2004). Conductivity dependence of cross-polar potential saturation. Journal of Geophysical Research: Space Physics, 109(A4). Retrieved 2022-12- 19, from https://agupubs.onlinelibrary.wiley.com/doi/abs/10.1029/ 2003JA010286 doi: https://doi.org/10.1029/2003JA010286
1142 1143 1144 1145 1146 1147 1148 1149 1150 1151 1152 1153 1154 1155 1156	 Milan, S. E., Walach, M., Carter, J. A., Sangha, H., & Anderson, B. J. (2019). Substorm onset latitude and the steadiness of magnetospheric convection. Journal of Geophysical Research: Space Physics, 124 (3), 1738-1752. Retrieved 2022-12-19, from https://onlinelibrary.wiley.com/doi/abs/10.1029/ 2018JA025969 doi: 10.1029/2018JA025969 Mishin, V., & Karavaev, Y. (2017). Saturation of the magnetosphere dur- ing superstorms: New results from the magnetogram inversion technique. Solar-Terrestrial Physics, 3(3), 28-36. Retrieved 2022-10-28, from http:// naukaru.ru/en/nauka/article/18490/view doi: 10.12737/stp-33201704 Moen, J., & Brekke, A. (1993). The solar flux influence on quiet time conductances in the auroral ionosphere. Geophysical Research Letters, 20(10), 971-974. Re- trieved 2022-12-19, from https://agupubs.onlinelibrary.wiley.com/doi/ abs/10.1029/92GL02109 doi: https://doi.org/10.1029/92GL02109 Nagatsuma, T. (2004). Conductivity dependence of cross-polar potential saturation. Journal of Geophysical Research: Space Physics, 109(A4). Retrieved 2022-12- 19, from https://agupubs.onlinelibrary.wiley.com/doi/abs/10.1029/ 2003JA010286 doi: https://doi.org/10.1029/2003JA010286 Newell, P. T., & Gjerloev, J. W. (2011a). Evaluation of SuperMAG auroral electro-
1142 1143 1144 1145 1146 1147 1148 1149 1150 1151 1152 1153 1154 1155 1156 1157 1158	 Milan, S. E., Walach, M., Carter, J. A., Sangha, H., & Anderson, B. J. (2019). Substorm onset latitude and the steadiness of magnetospheric convection. Journal of Geophysical Research: Space Physics, 124 (3), 1738-1752. Retrieved 2022-12-19, from https://onlinelibrary.wiley.com/doi/abs/10.1029/ 2018JA025969 doi: 10.1029/2018JA025969 Mishin, V., & Karavaev, Y. (2017). Saturation of the magnetosphere dur- ing superstorms: New results from the magnetogram inversion technique. Solar-Terrestrial Physics, 3(3), 28-36. Retrieved 2022-10-28, from http:// naukaru.ru/en/nauka/article/18490/view doi: 10.12737/stp-33201704 Moen, J., & Brekke, A. (1993). The solar flux influence on quiet time conductances in the auroral ionosphere. Geophysical Research Letters, 20(10), 971-974. Re- trieved 2022-12-19, from https://agupubs.onlinelibrary.wiley.com/doi/ abs/10.1029/92GL02109 doi: https://doi.org/10.1029/92GL02109 Nagatsuma, T. (2004). Conductivity dependence of cross-polar potential saturation. Journal of Geophysical Research: Space Physics, 109(A4). Retrieved 2022-12- 19, from https://agupubs.onlinelibrary.wiley.com/doi/abs/10.1029/ 2003JA010286 doi: https://doi.org/10.1029/2003JA010286 Newell, P. T., & Gjerloev, J. W. (2011a). Evaluation of SuperMAG auroral electro- jet indices as indicators of substorms and auroral power. Journal of Geophysic
1142 1143 1144 1145 1146 1147 1148 1149 1150 1151 1152 1153 1154 1155 1156 1157 1158 1159 1159	 Milan, S. E., Walach, M., Carter, J. A., Sangha, H., & Anderson, B. J. (2019). Substorm onset latitude and the steadiness of magnetospheric convection. Journal of Geophysical Research: Space Physics, 124 (3), 1738–1752. Retrieved 2022-12-19, from https://onlinelibrary.wiley.com/doi/abs/10.1029/ 2018JA025969 doi: 10.1029/2018JA025969 Mishin, V., & Karavaev, Y. (2017). Saturation of the magnetosphere dur- ing superstorms: New results from the magnetogram inversion technique. Solar-Terrestrial Physics, 3(3), 28–36. Retrieved 2022-10-28, from http:// naukaru.ru/en/nauka/article/18490/view doi: 10.12737/stp-33201704 Moen, J., & Brekke, A. (1993). The solar flux influence on quiet time conductances in the auroral ionosphere. Geophysical Research Letters, 20(10), 971-974. Re- trieved 2022-12-19, from https://agupubs.onlinelibrary.wiley.com/doi/ abs/10.1029/92GL02109 doi: https://doi.org/10.1029/92GL02109 Nagatsuma, T. (2004). Conductivity dependence of cross-polar potential saturation. Journal of Geophysical Research: Space Physics, 109(A4). Retrieved 2022-12- 19, from https://agupubs.onlinelibrary.wiley.com/doi/abs/10.1029/ 2003JA010286 doi: https://doi.org/10.1029/2003JA010286 Newell, P. T., & Gjerloev, J. W. (2011a). Evaluation of SuperMAG auroral electro- jet indices as indicators of substorms and auroral power. Journal of Geophysi- cal Research: Space Physics, 116(A12), 2011JA016779. Retrieved 2022-11-06,
1142 1143 1144 1145 1146 1147 1148 1149 1150 1151 1152 1153 1154 1155 1156 1157 1158 1159 1160 1161	 Milan, S. E., Walach, M., Carter, J. A., Sangha, H., & Anderson, B. J. (2019). Substorm onset latitude and the steadiness of magnetospheric convection. Journal of Geophysical Research: Space Physics, 124 (3), 1738–1752. Retrieved 2022-12-19, from https://onlinelibrary.wiley.com/doi/abs/10.1029/ 2018JA025969 doi: 10.1029/2018JA025969 Mishin, V., & Karavaev, Y. (2017). Saturation of the magnetosphere dur- ing superstorms: New results from the magnetogram inversion technique. Solar-Terrestrial Physics, 3(3), 28–36. Retrieved 2022-10-28, from http:// naukaru.ru/en/nauka/article/18490/view doi: 10.12737/stp-33201704 Moen, J., & Brekke, A. (1993). The solar flux influence on quiet time conductances in the auroral ionosphere. Geophysical Research Letters, 20(10), 971-974. Re- trieved 2022-12-19, from https://agupubs.onlinelibrary.wiley.com/doi/ abs/10.1029/92GL02109 doi: https://doi.org/10.1029/92GL02109 Nagatsuma, T. (2004). Conductivity dependence of cross-polar potential saturation. Journal of Geophysical Research: Space Physics, 109(A4). Retrieved 2022-12- 19, from https://agupubs.onlinelibrary.wiley.com/doi/abs/10.1029/ 2003JA010286 doi: https://doi.org/10.1029/2003JA010286 Newell, P. T., & Gjerloev, J. W. (2011a). Evaluation of SuperMAG auroral electro- jet indices as indicators of substorms and auroral power. Journal of Geophysi- cal Research: Space Physics, 116(A12), 2011JA016779. Retrieved 2022-11-06, from https://onlinelibrary.wiley.com/doi/10.1029/2011JA016779 doi:
1142 1143 1144 1145 1146 1147 1148 1149 1150 1151 1152 1153 1154 1155 1155 1156 1157 1158 1159 1160 1161	 Milan, S. E., Walach, M., Carter, J. A., Sangha, H., & Anderson, B. J. (2019). Substorm onset latitude and the steadiness of magnetospheric convection. Journal of Geophysical Research: Space Physics, 124 (3), 1738–1752. Retrieved 2022-12-19, from https://onlinelibrary.wiley.com/doi/abs/10.1029/ 2018JA025969 doi: 10.1029/2018JA025969 Mishin, V., & Karavaev, Y. (2017). Saturation of the magnetosphere dur- ing superstorms: New results from the magnetogram inversion technique. Solar-Terrestrial Physics, 3(3), 28–36. Retrieved 2022-10-28, from http:// naukaru.ru/en/nauka/article/18490/view doi: 10.12737/stp-33201704 Moen, J., & Brekke, A. (1993). The solar flux influence on quiet time conductances in the auroral ionosphere. Geophysical Research Letters, 20(10), 971-974. Re- trieved 2022-12-19, from https://agupubs.onlinelibrary.wiley.com/doi/ abs/10.1029/92GL02109 doi: https://doi.org/10.1029/92GL02109 Nagatsuma, T. (2004). Conductivity dependence of cross-polar potential saturation. Journal of Geophysical Research: Space Physics, 109(A4). Retrieved 2022-12- 19, from https://agupubs.onlinelibrary.wiley.com/doi/abs/10.1029/ 2003JA010286 doi: https://doi.org/10.1029/2003JA010286 Newell, P. T., & Gjerloev, J. W. (2011a). Evaluation of SuperMAG auroral electro- jet indices as indicators of substorms and auroral power. Journal of Geophysi- cal Research: Space Physics, 116(A12), 2011JA016779. Retrieved 2022-11-06,
1142 1143 1144 1145 1146 1147 1148 1149 1150 1151 1152 1153 1154 1155 1155 1156 1157 1158 1159 1160 1161	 Milan, S. E., Walach, M., Carter, J. A., Sangha, H., & Anderson, B. J. (2019). Substorm onset latitude and the steadiness of magnetospheric convection. Journal of Geophysical Research: Space Physics, 124 (3), 1738–1752. Retrieved 2022-12-19, from https://onlinelibrary.wiley.com/doi/abs/10.1029/ 2018JA025969 doi: 10.1029/2018JA025969 Mishin, V., & Karavaev, Y. (2017). Saturation of the magnetosphere dur- ing superstorms: New results from the magnetogram inversion technique. Solar-Terrestrial Physics, 3(3), 28–36. Retrieved 2022-10-28, from http:// naukaru.ru/en/nauka/article/18490/view doi: 10.12737/stp-33201704 Moen, J., & Brekke, A. (1993). The solar flux influence on quiet time conductances in the auroral ionosphere. Geophysical Research Letters, 20(10), 971-974. Re- trieved 2022-12-19, from https://agupubs.onlinelibrary.wiley.com/doi/ abs/10.1029/92GL02109 doi: https://doi.org/10.1029/92GL02109 Nagatsuma, T. (2004). Conductivity dependence of cross-polar potential saturation. Journal of Geophysical Research: Space Physics, 109(A4). Retrieved 2022-12- 19, from https://agupubs.onlinelibrary.wiley.com/doi/abs/10.1029/ 2003JA010286 doi: https://doi.org/10.1029/2003JA010286 Newell, P. T., & Gjerloev, J. W. (2011a). Evaluation of SuperMAG auroral electro- jet indices as indicators of substorms and auroral power. Journal of Geophysic cal Research: Space Physics, 116(A12), 2011JA016779. Retrieved 2022-11-06, from https://onlinelibrary.wiley.com/doi/10.1029/2011JA016779 doi: 10.1029/2011JA016779
1142 1143 1144 1145 1146 1147 1148 1149 1150 1151 1152 1153 1154 1155 1156 1157 1158 1159 1160 1161 1162 1163	 Milan, S. E., Walach, M., Carter, J. A., Sangha, H., & Anderson, B. J. (2019). Substorm onset latitude and the steadiness of magnetospheric convection. Journal of Geophysical Research: Space Physics, 124 (3), 1738–1752. Retrieved 2022-12-19, from https://onlinelibrary.wiley.com/doi/abs/10.1029/ 2018JA025969 doi: 10.1029/2018JA025969 Mishin, V., & Karavaev, Y. (2017). Saturation of the magnetosphere dur- ing superstorms: New results from the magnetogram inversion technique. Solar-Terrestrial Physics, 3(3), 28–36. Retrieved 2022-10-28, from http:// naukaru.ru/en/nauka/article/18490/view doi: 10.12737/stp-33201704 Moen, J., & Brekke, A. (1993). The solar flux influence on quiet time conductances in the auroral ionosphere. Geophysical Research Letters, 20(10), 971-974. Re- trieved 2022-12-19, from https://agupubs.onlinelibrary.wiley.com/doi/ abs/10.1029/92GL02109 doi: https://doi.org/10.1029/92GL02109 Nagatsuma, T. (2004). Conductivity dependence of cross-polar potential saturation. Journal of Geophysical Research: Space Physics, 109(A4). Retrieved 2022-12- 19, from https://agupubs.onlinelibrary.wiley.com/doi/abs/10.1029/ 2003JA010286 doi: https://doi.org/10.1029/2003JA010286 Newell, P. T., & Gjerloev, J. W. (2011a). Evaluation of SuperMAG auroral electro- jet indices as indicators of substorms and auroral power. Journal of Geophysi- cal Research: Space Physics, 116(A12), 2011JA016779. Retrieved 2022-11-06, from https://onlinelibrary.wiley.com/doi/10.1029/2011JA016779 doi: 10.1029/2011JA016779 Newell, P. T., & Gjerloev, J. W. (2011b). Substorm and magnetosphere charac-
1142 1143 1144 1145 1146 1147 1148 1149 1150 1151 1152 1153 1154 1155 1156 1157 1158 1159 1160 1161 1162 1163	 Milan, S. E., Walach, M., Carter, J. A., Sangha, H., & Anderson, B. J. (2019). Substorm onset latitude and the steadiness of magnetospheric convection. Journal of Geophysical Research: Space Physics, 124 (3), 1738–1752. Retrieved 2022-12-19, from https://onlinelibrary.wiley.com/doi/abs/10.1029/ 2018JA025969 doi: 10.1029/2018JA025969 Mishin, V., & Karavaev, Y. (2017). Saturation of the magnetosphere dur- ing superstorms: New results from the magnetogram inversion technique. Solar-Terrestrial Physics, 3(3), 28–36. Retrieved 2022-10-28, from http:// naukaru.ru/en/nauka/article/18490/view doi: 10.12737/stp-33201704 Moen, J., & Brekke, A. (1993). The solar flux influence on quiet time conductances in the auroral ionosphere. Geophysical Research Letters, 20(10), 971-974. Re- trieved 2022-12-19, from https://agupubs.onlinelibrary.wiley.com/doi/ abs/10.1029/92GL02109 doi: https://doi.org/10.1029/92GL02109 Nagatsuma, T. (2004). Conductivity dependence of cross-polar potential saturation. Journal of Geophysical Research: Space Physics, 109(A4). Retrieved 2022-12- 19, from https://agupubs.onlinelibrary.wiley.com/doi/abs/10.1029/ 2003JA010286 doi: https://doi.org/10.1029/2003JA010286 Newell, P. T., & Gjerloev, J. W. (2011a). Evaluation of SuperMAG auroral electro- jet indices as indicators of substorms and auroral power. Journal of Geophysic al Research: Space Physics, 116(A12), 2011JA016779. Retrieved 2022-11-06, from https://onlinelibrary.wiley.com/doi/10.1029/2011JA016779 doi: 10.1029/2011JA016779 Newell, P. T., & Gjerloev, J. W. (2011b). Substorm and magnetosphere charac- teristic scales inferred from the SuperMAG auroral electrojet indices. Jour- inform https://onlinelibrary.wiley.com/doi/10.1029/2011JA016779

1169	Newell, P. T., & Gjerloev, J. W. (2012). SuperMAG-based partial ring cur-
1170	rent indices. Journal of Geophysical Research: Space Physics, 117(A5),
1171	2012JA017586. Retrieved 2022-12-11, from https://onlinelibrary.wiley
1172	.com/doi/10.1029/2012JA017586 doi: 10.1029/2012JA017586
1173	Newell, P. T., Sotirelis, T., Skura, J. P., Meng, CI., & Lyatsky, W. (2002). Ultravi-
1174	olet insolation drives seasonal and diurnal space weather variations. Journal of
1175	Geophysical Research, 107(A10), 1305. Retrieved 2022-12-09, from http://doi
1176	.wiley.com/10.1029/2001JA000296 doi: 10.1029/2001JA000296
1177	Ou, J., Du, A., Ge, Y., Luo, H., Zhang, Y., & Guo, Z. (2022). Statistical study
1178	on the North-South asymmetric distribution of the mid-low-latitude nightside
1179	disturbed magnetic fields. Journal of Geophysical Research: Space Physics,
1180	127(3). Retrieved 2022-12-19, from https://onlinelibrary.wiley.com/doi/
1181	10.1029/2021JA029970 doi: 10.1029/2021JA029970
1182	Park, K. S., Ogino, T., & Walker, R. J. (2006). On the importance of antiparallel
1183	reconnection when the dipole tilt and IMF B_{-y} are nonzero. Journal of Geo-
1184	physical Research, 111(A5), A05202. Retrieved 2022-12-12, from http://doi
1185	.wiley.com/10.1029/2004JA010972 doi: 10.1029/2004JA010972
1186	Ridley, A. J., Gombosi, T. I., & DeZeeuw, D. L. (2004). Ionospheric control of the
1187	magnetosphere: conductance. Annales Geophysicae, 22(2), 567–584. Retrieved
1188	2022-11-10, from https://angeo.copernicus.org/articles/22/567/2004/
1189	doi: 10.5194/angeo-22-567-2004
1190	Russell, C. T., & McPherron, R. L. (1973). Semiannual variation of geomagnetic
1190	activity. Journal of Geophysical Research, 78(1), 92–108. Retrieved 2022-11-
1191	03, from http://doi.wiley.com/10.1029/JA078i001p00092 doi: 10.1029/
1192	JA078i001p00092
1193	Russell, C. T., Wang, Y. L., & Raeder, J. (2003). Possible dipole tilt dependence of
1194	dayside magnetopause reconnection. <i>Geophysical Research Letters</i> , 30(18). Re-
1195	trieved 2022-12-12, from http://doi.wiley.com/10.1029/2003GL017725 doi:
1190	10.1029/2003GL017725
	Spence, H. E. (1996). The what, where, when, and why of magnetospheric substorm
1198	triggers. Eos, Transactions American Geophysical Union, 77(9), 81–86. Re-
1199 1200	trieved 2022-12-19, from http://doi.wiley.com/10.1029/96E000051 doi: 10
1200	.1029/96EO00051
1201	Stauning, P. (2007). A new index for the interplanetary merging electric field
1202	and geomagnetic activity: Application of the unified polar cap indices. Space
1203	Weather, 5(9), n/a-n/a. Retrieved 2023-02-19, from http://doi.wiley.com/
1204	10.1029/2007SW000311 doi: 10.1029/2007SW000311
1205	Tanaka, T., Ebihara, Y., Watanabe, M., Den, M., Fujita, S., Kikuchi, T.,
1200	Kataoka, R. (2021). Roles of the M-I coupling and plasma sheet dissipa-
1207	tion on the growth-phase thinning and subsequent transition to the onset.
1200	Journal of Geophysical Research: Space Physics, 126(12). Retrieved 2022-12-
1209	19, from https://onlinelibrary.wiley.com/doi/10.1029/2021JA029925
1210	doi: 10.1029/2021JA029925
1211	Thébault, E., Finlay, C. C., Beggan, C. D., Alken, P., Aubert, J., Barrois, O.,
1212	Zvereva, T. (2015). International Geomagnetic Reference Field: the
1213	12th generation. Earth, Planets and Space, 67(1), 79. Retrieved 2022-11-
1214	25, from http://www.earth-planets-space.com/content/67/1/79 doi:
	10.1186/s40623-015-0228-9
1216	Trattner, K. J., Petrinec, S. M., Fuselier, S. A., & Phan, T. D. (2012). The lo-
1217	cation of reconnection at the magnetopause: Testing the maximum mag-
1218	netic shear model with THEMIS observations. Journal of Geophysical Re-
1219	search: Space Physics, 117(A1), 2011JA016959. Retrieved 2023-04-09, from
1220	https://onlinelibrary.wiley.com/doi/10.1029/2011JA016959 doi:
1221	10.1029/2011JA016959
1222	Troshichev, O. (2022). PC index as a ground-based indicator of the solar wind

1224	energy incoming into the magnetosphere: (1) relation of PC index to the so-
1225	lar wind electric field EKL. Frontiers in Astronomy and Space Sciences,
1226	9, 1069470. Retrieved 2023-02-19, from https://www.frontiersin.org/
1227	articles/10.3389/fspas.2022.1069470/full doi: 10.3389/fspas.2022
1228	.1069470
1229	Tulegenov, B., Raeder, J., Cramer, W. D., Ferdousi, B., Fuller-Rowell, T. J.,
1230	Maruyama, N., & Strangeway, R. J. (2023). Storm time polar cap expansion:
1231	interplanetary magnetic field clock angle dependence. Annales Geophysicae,
1232	41(1), 39-54. Retrieved 2023-01-20, from https://angeo.copernicus.org/
1233	articles/41/39/2023/ doi: 10.5194/angeo-41-39-2023
1234	Wang, H., & Lühr, H. (2007). Seasonal-longitudinal variation of substorm occur-
1235	rence frequency: Evidence for ionospheric control. Geophysical Research Let-
1236	ters, 34(7), L07104. Retrieved 2022-11-27, from http://doi.wiley.com/10
1237	.1029/2007GL029423 doi: 10.1029/2007GL029423
1238	Wang, H., Zhang, K. D., Wan, X., & Lühr, H. (2017). Universal time variation
1239	of high-latitude thermospheric disturbance wind in response to a substorm.
1240	Journal of Geophysical Research: Space Physics, 122(4), 4638–4653. Retrieved
1241	2022-11-27, from http://doi.wiley.com/10.1002/2016JA023630 doi:
1242	10.1002/2016JA023630
1243	Zhang, B., Lotko, W., Brambles, O., Wiltberger, M., & Lyon, J. (2015). Electron
1244	precipitation models in global magnetosphere simulations. Journal of Geo-
1245	physical Research: Space Physics, 120(2), 1035–1056. Retrieved 2022-12-09,
1246	from https://onlinelibrary.wiley.com/doi/10.1002/2014JA020615 doi:
1247	10.1002/2014JA020615
1248	Zhao, H., & Zong, QG. (2012). Seasonal and diurnal variation of geomagnetic
1249	activity: Russell-McPherron effect during different IMF polarity and/or ex-
1250	treme solar wind conditions. Journal of Geophysical Research: Space Physics,
1251	117(A11), n/a-n/a. Retrieved 2022-12-29, from http://doi.wiley.com/
1252	10.1029/2012JA017845 doi: 10.1029/2012JA017845
1253	Zhu, C. B., Zhang, H., Ge, Y. S., Pu, Z. Y., Liu, W. L., Wan, W. X., Wang,
1254	Y. F. (2015). Dipole tilt angle effect on magnetic reconnection locations on
1255	the magnetopause. Journal of Geophysical Research: Space Physics, $120(7)$,
1256	5344-5354. Retrieved 2023-04-09, from https://onlinelibrary.wiley.com/
1257	doi/10.1002/2015JA020989 doi: 10.1002/2015JA020989
1258	Zou, Y., Lyons, L., Conde, M., Varney, R., Angelopoulos, V., & Mende, S. (2021).
1259	Effects of substorms on high-latitude upper thermospheric winds. Journal
1260	of Geophysical Research: Space Physics, 126(1). Retrieved 2023-04-09, from
1261	https://onlinelibrary.wiley.com/doi/10.1029/2020JA028193 doi:
1262	10.1029/2020JA028193

1263 7 Open Research

The data used in this study are all openly available. The interplanetary data are available from the Physics Data Facility (SPDF) at NASA's Goddard Space Flight Center as the Omni composite from https://omniweb.gsfc.nasa.gov/ow_min.html. The SuperMAG SML and SMU indices and the substorm onset lists are available from the SuperMAG project website at the Johns Hopkins University Applied Physics Laboratory at http://supermag.jhuapl.edu/indices/.

1270 Acknowledgments

1271The authors are grateful to the many instrument scientists and engineers who make1272the datasets employed in this study possible and the staff of a number of datacentres who1273allow easy access to the data: in particular the Space Physics Data Facility (SPDF) at1274NASA's Goddard Space Flight Center for the Omni composite of interplanetary obser-

vations and the SuperMAG project staff coordinated at The Johns Hopkins University

1276 Applied Physics Laboratory, for the SMR and SML indices. The author thanks the many

PIs and instrument teams who contribute data to the SuperMAG project. This work is

 $_{1278}$ supported by a number of grants: consolidated grants number ST/R000921/1 and ST/V000497/1

¹²⁷⁹ from the United Kingdom Science and Technology Facilities Council (UKRI/STFC) and

the SWIGS Directed Highlight Topic Grant number NE/P016928/1/ and grant NE/S010033/1

¹²⁸¹ from the United Kingdom Natural Environment Research Council (UKRI/NERC).

Figure 1.

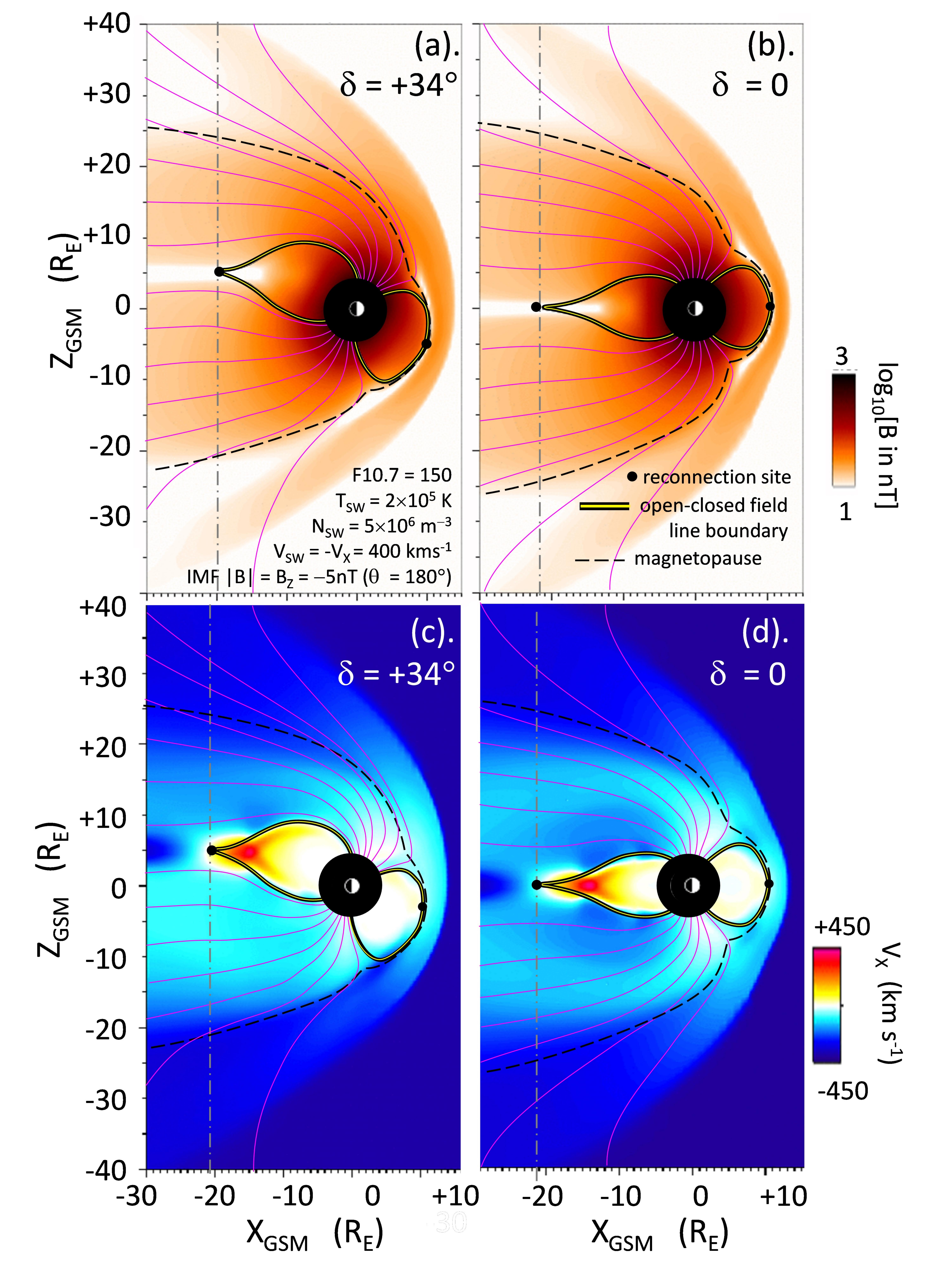
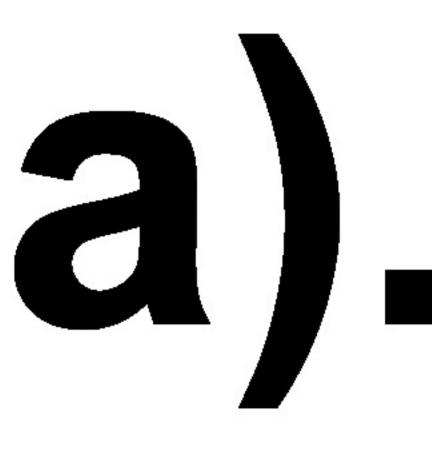


Figure 2.



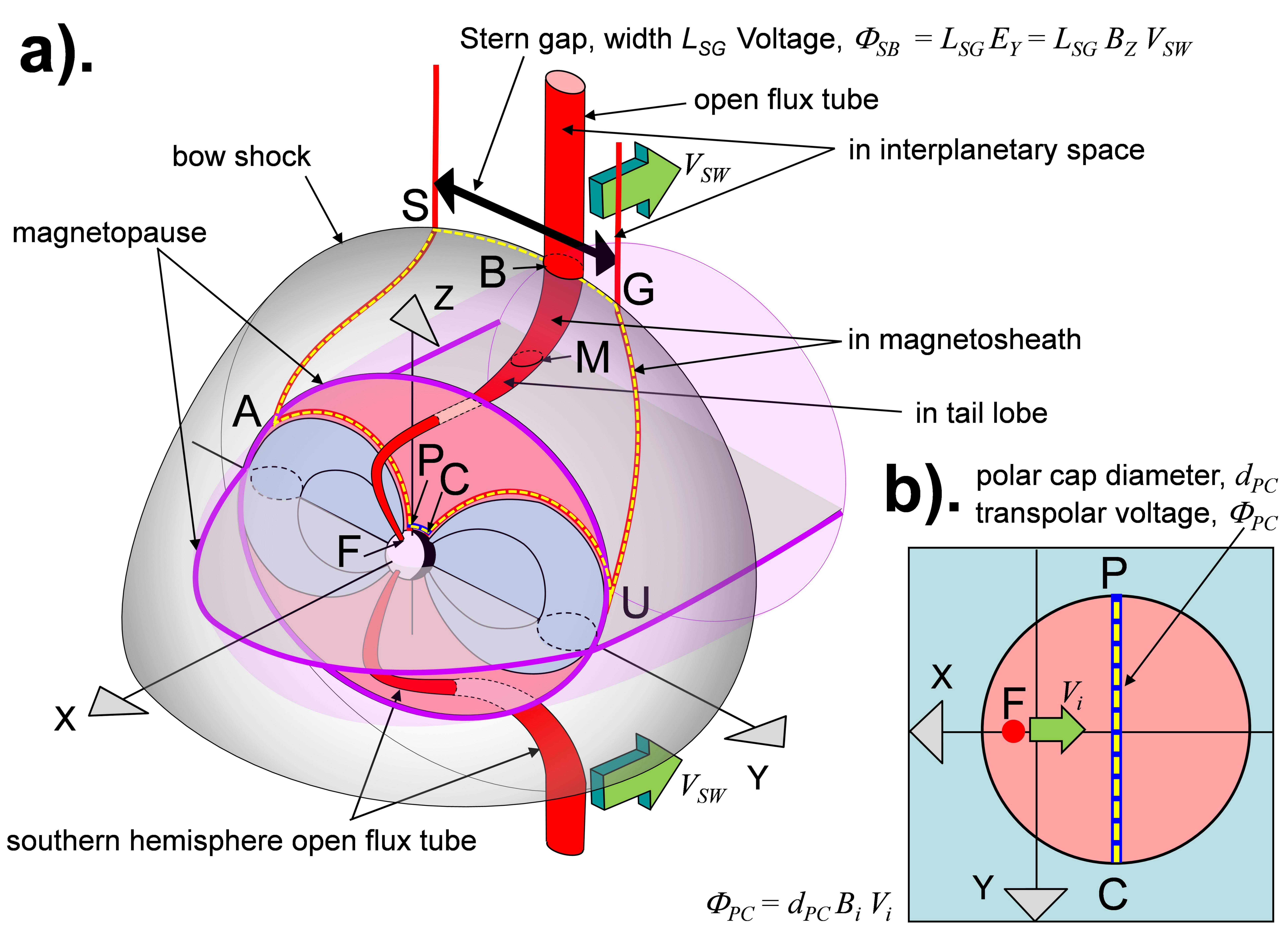


Figure 3.

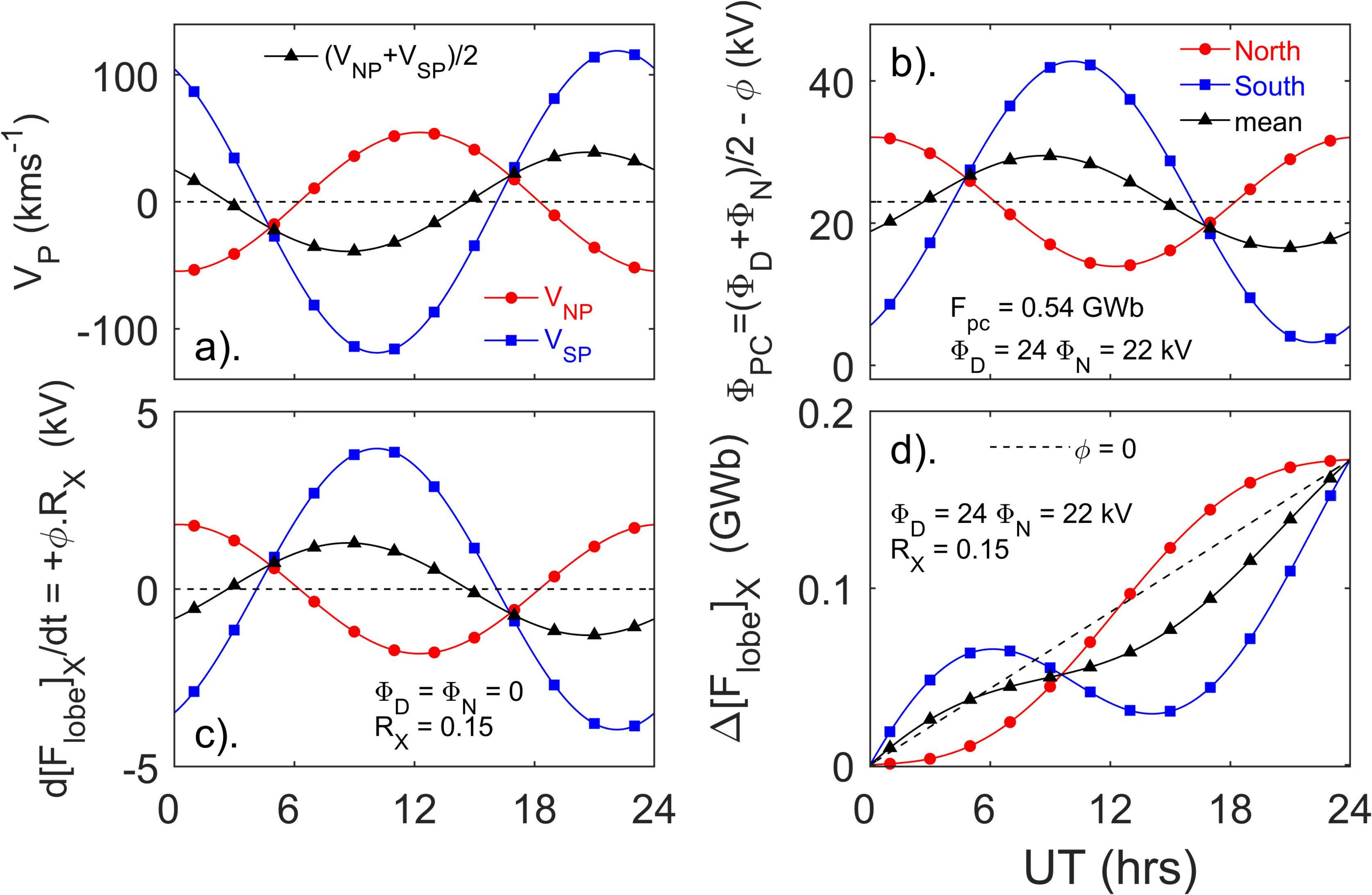


Figure 4.

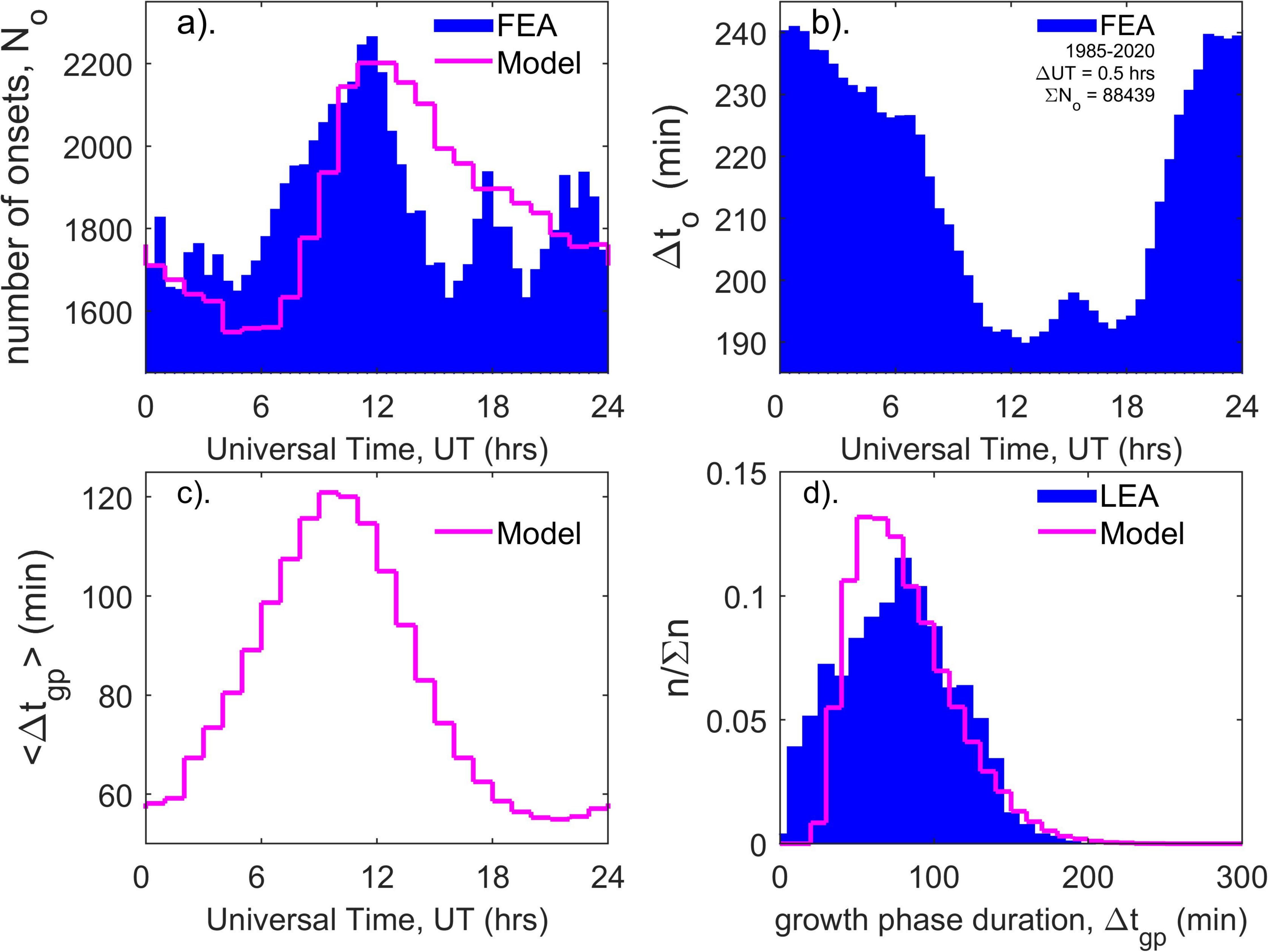


Figure 5.

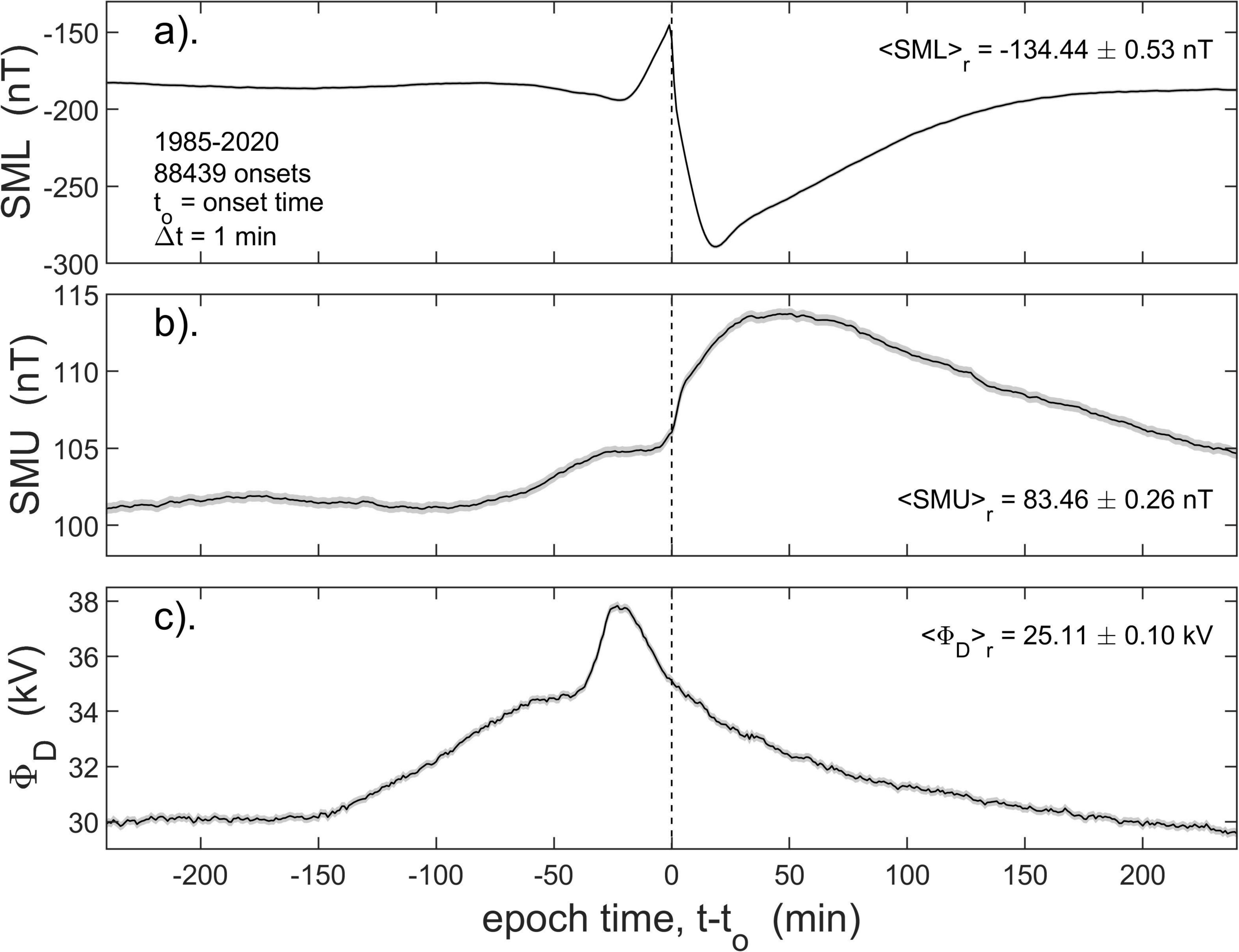
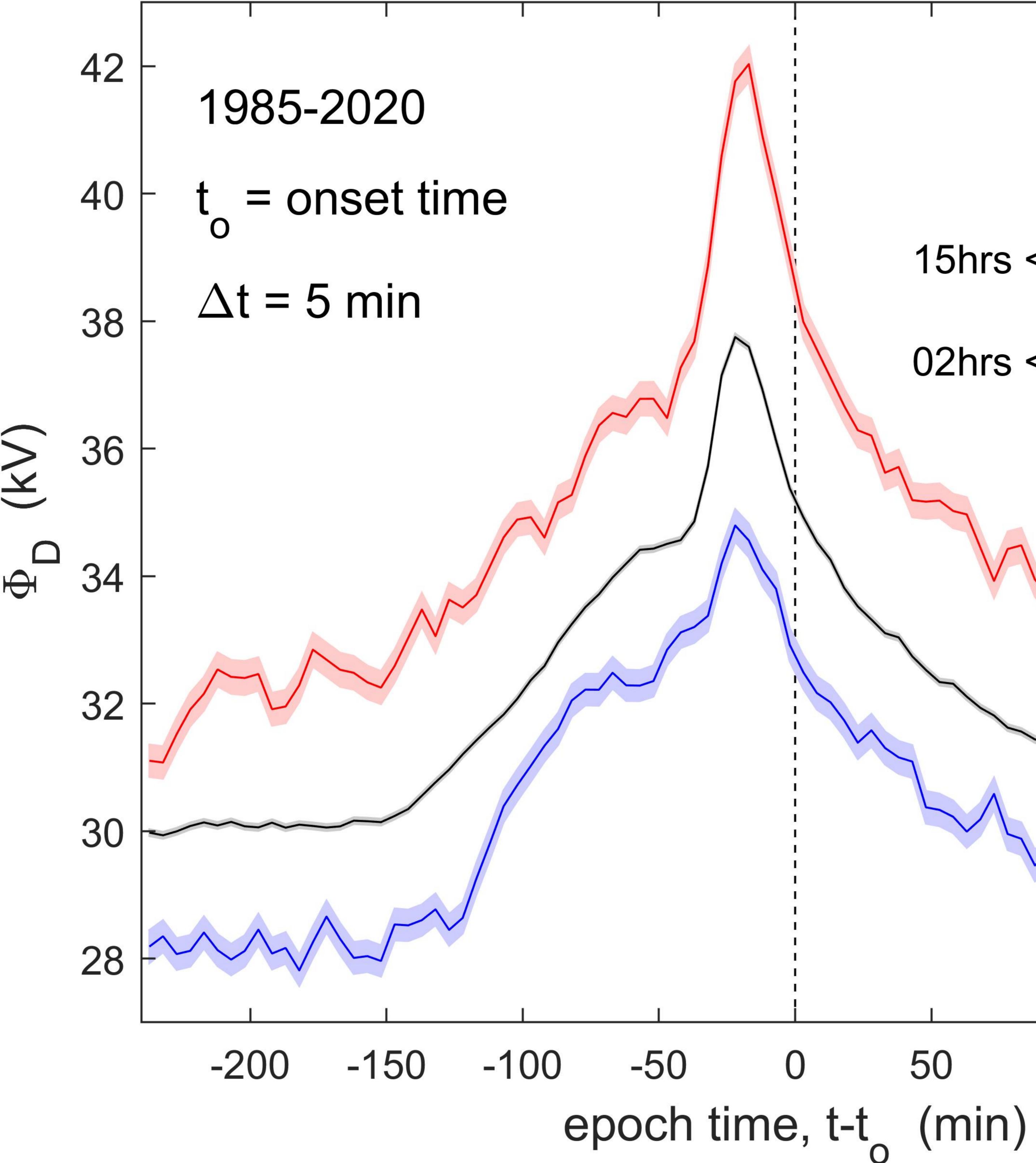


Figure 6.



all onsets 15hrs < UT < 16hrs 02hrs < UT < 03hrs

100

150

50

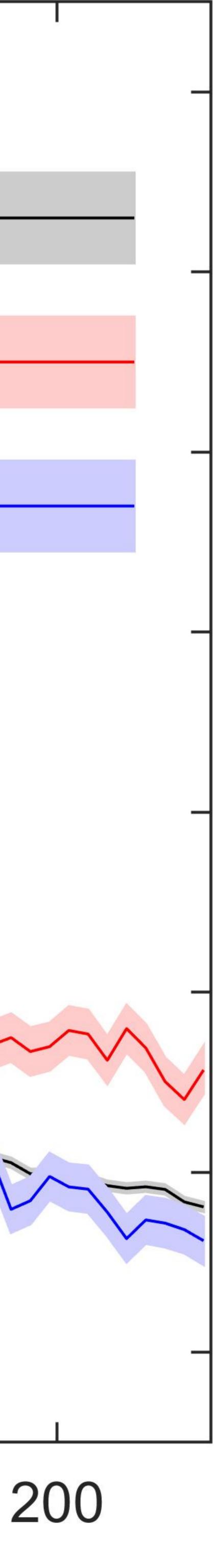


Figure 7.

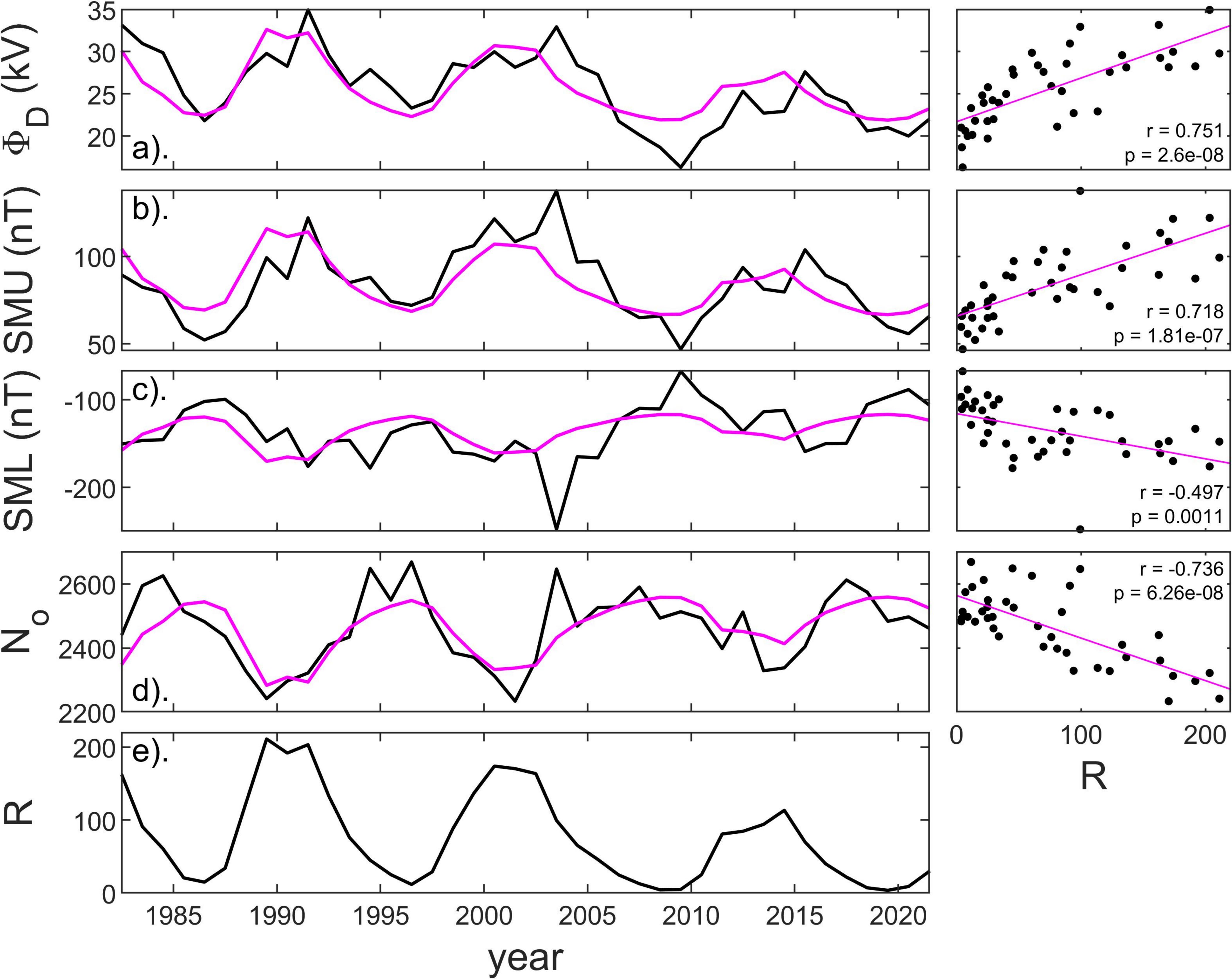


Figure 8.

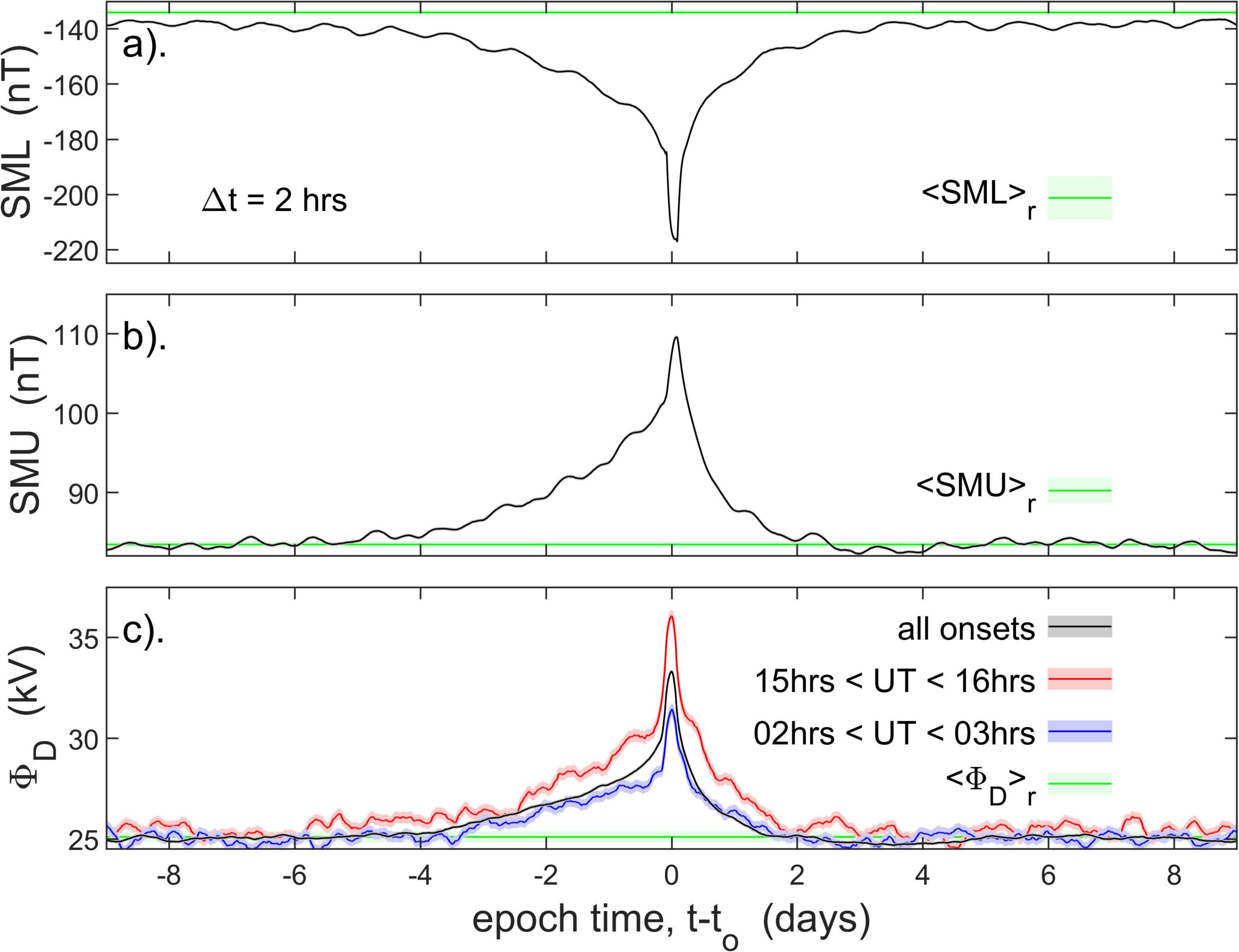


Figure 9.

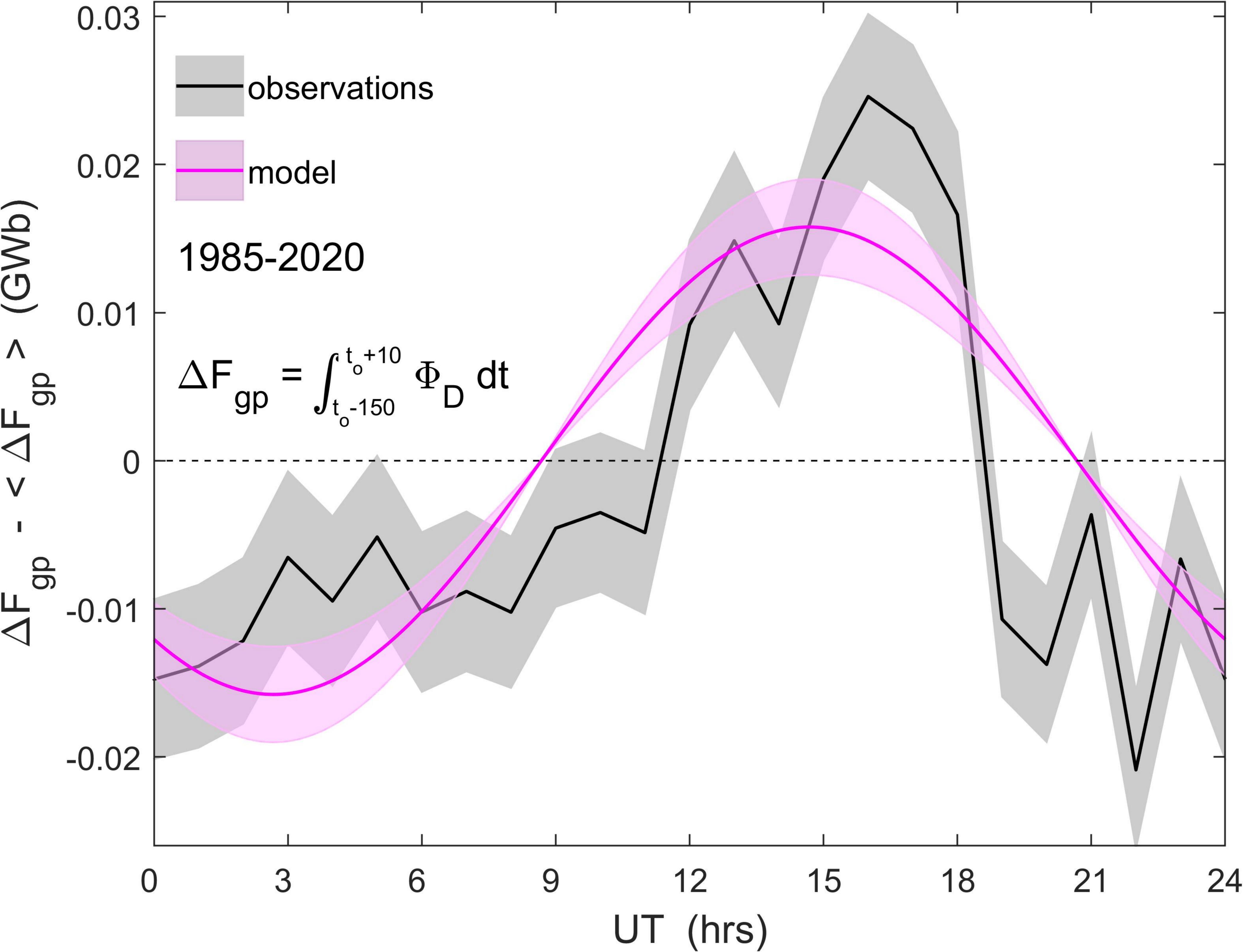


Figure 10.

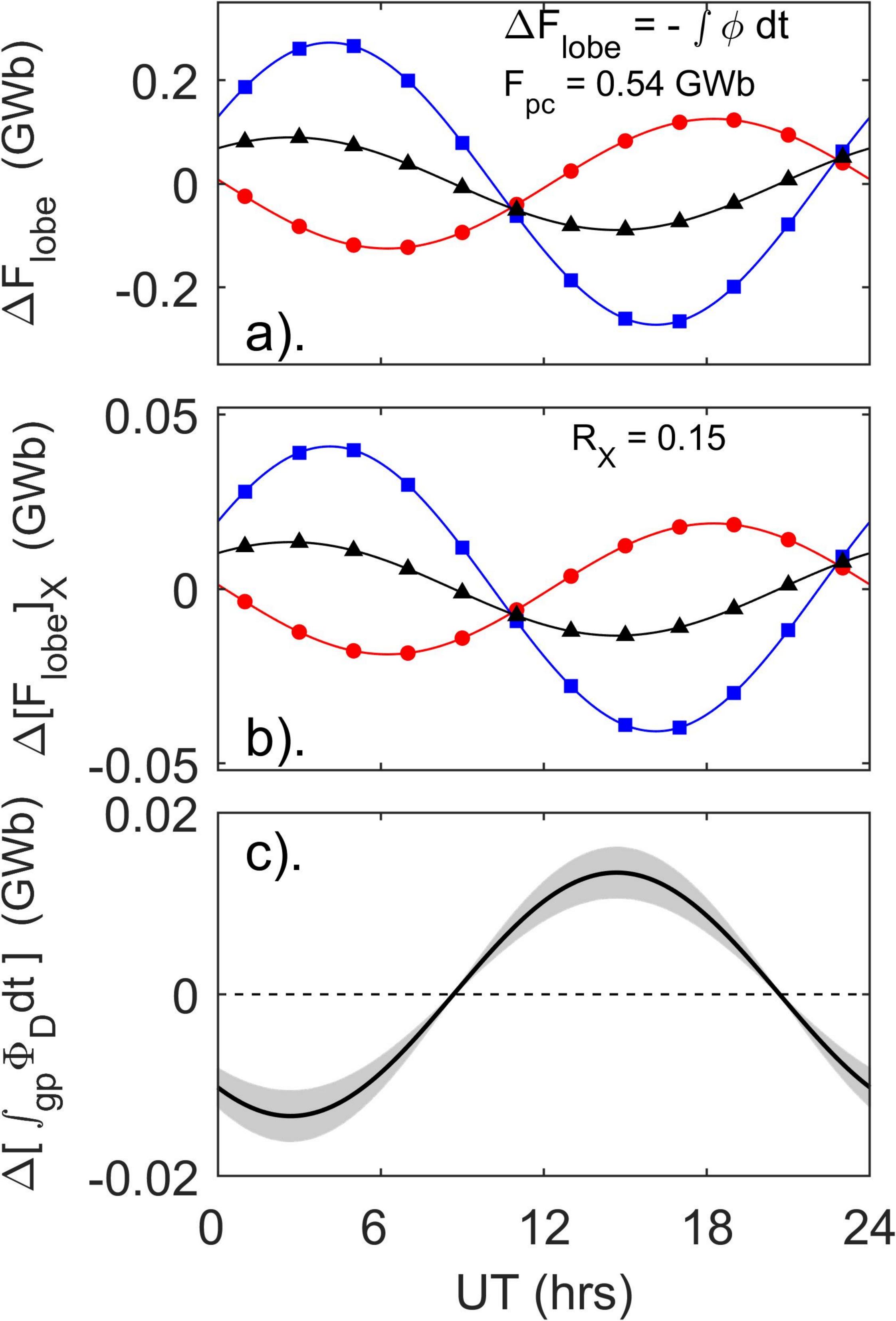


Figure 11.

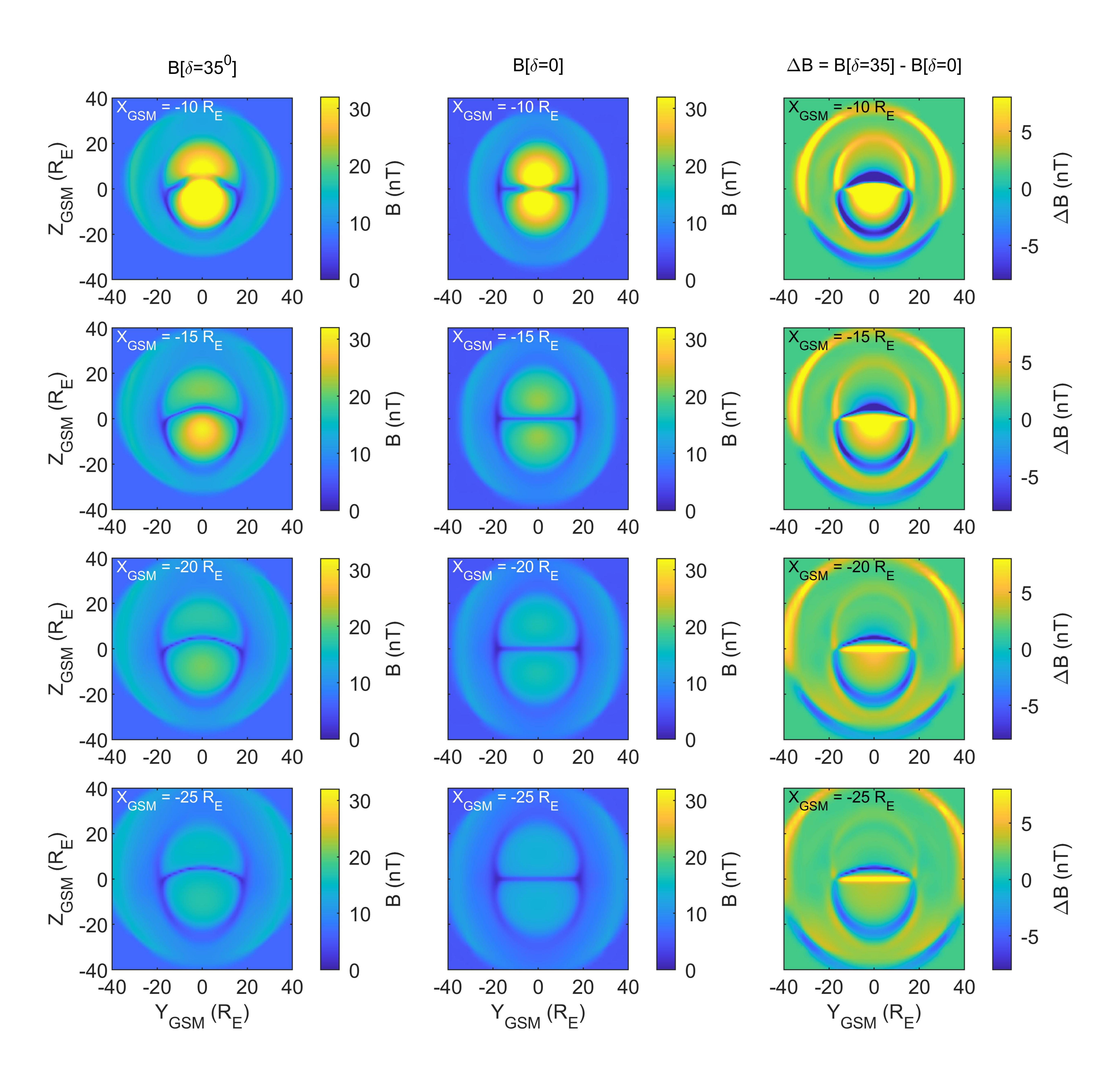


Figure 12.

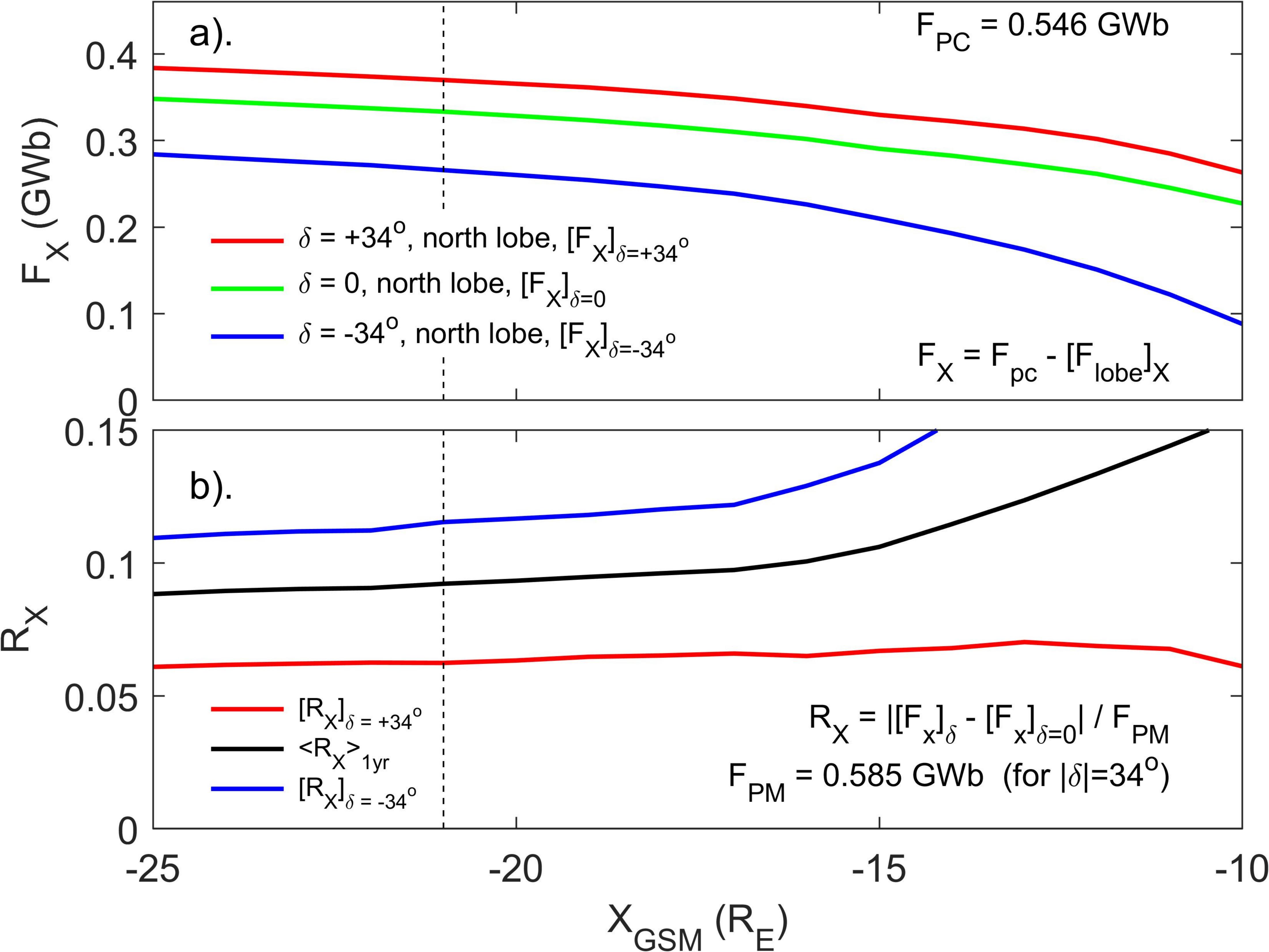


Figure 13.

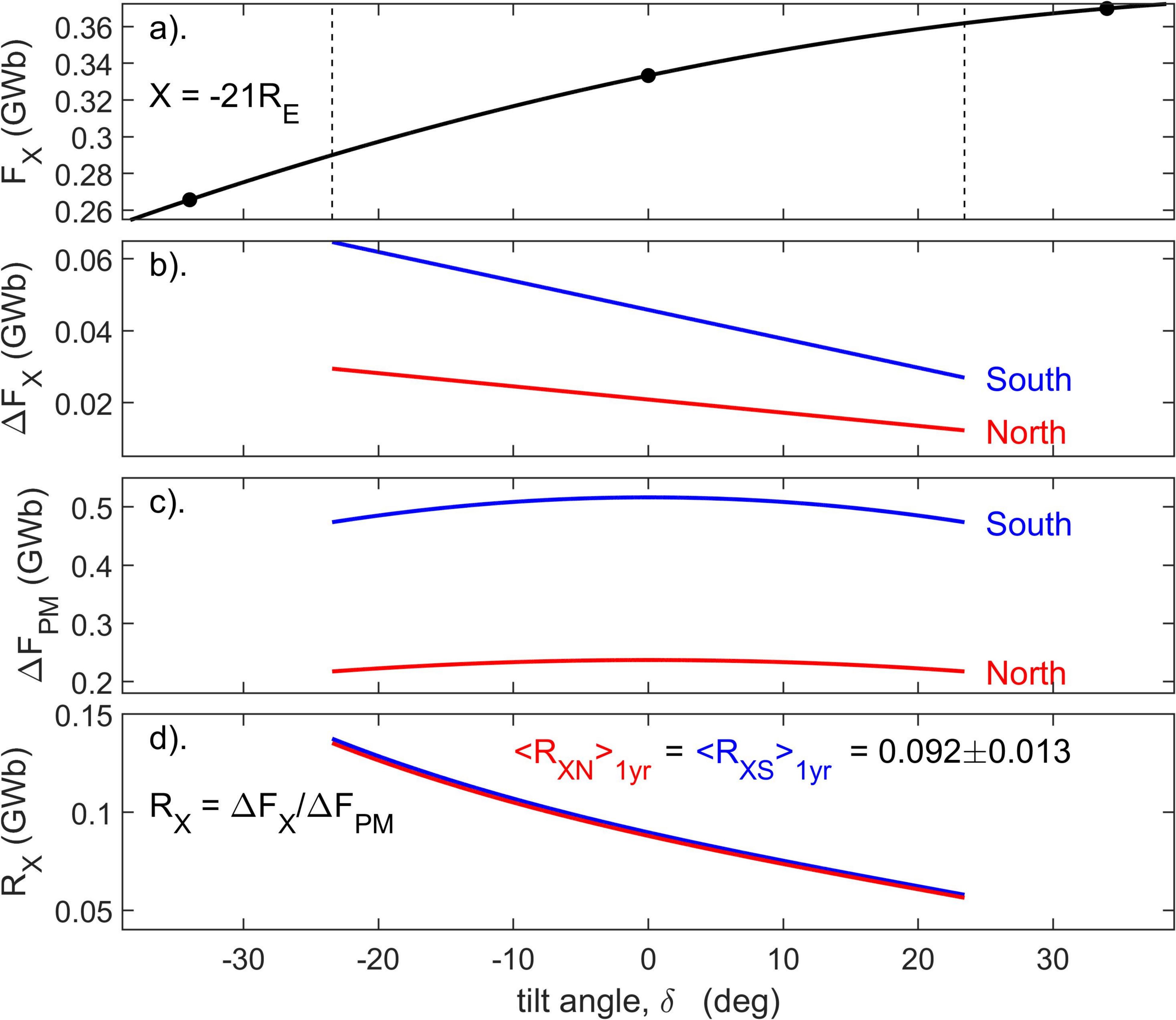
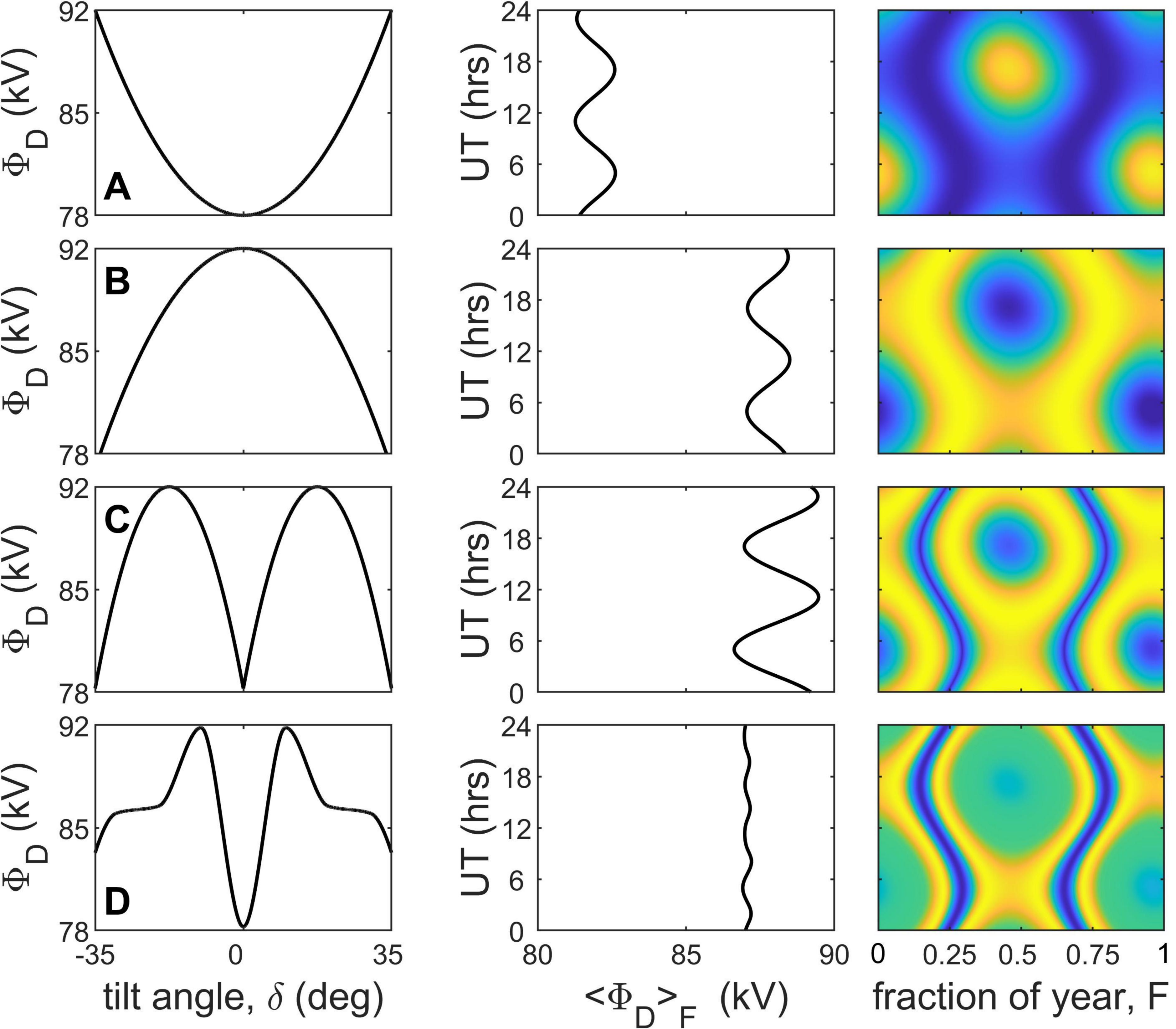
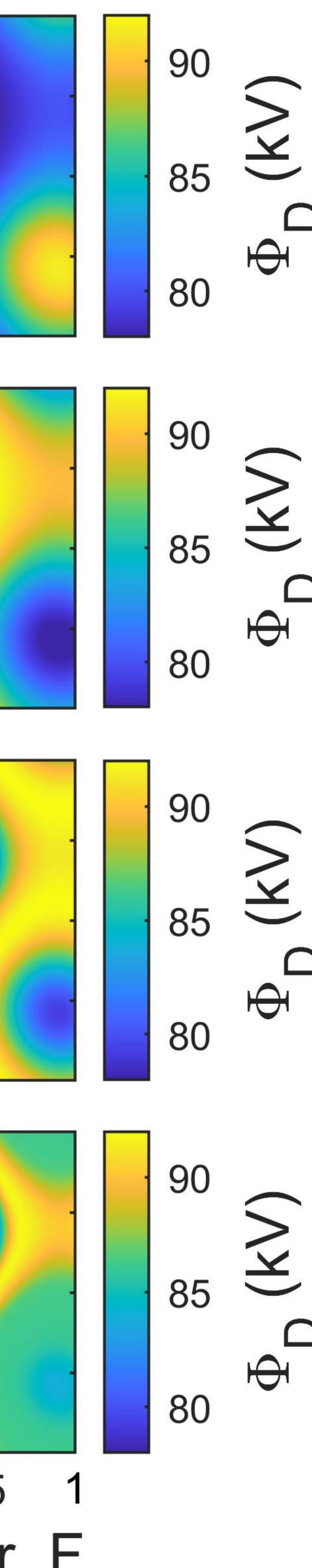


Figure 14.





Universal Time effects on substorm growth phases and onsets

$\mathbf{M}.\ \mathbf{Lockwood}^1$

 $^1\mathrm{Department}$ of Meteorology, University of Reading, Reading, Berkshire, RG6 6BB, UK

Key Points:

3

4

5

6	•	1 Universal Time effects in the magnetosphere are caused by the eccentric nature
7		of Earth's intrinsic magnetic field
8	•	2 There is a Universal Time dependence of the integrated magnetopause recon-
9		nection voltage needed to trigger substorm onset
10	•	3 Growth phases that lead to substorm onset show considerable preconditioning
11		by prior reconnection

Corresponding author: Mike Lockwood, m.lockwood@reading.ac.uk

12 Abstract

Universal Time (UT) variations in many magnetospheric state indicators and indices have 13 recently been reviewed by Lockwood and Milan (2023). Key effects are introduced into 14 magnetospheric dynamics by the eccentric nature of Earth's magnetic field, features that 15 cannot be reproduced by a geocentric field model. This paper studies the UT variation 16 in the occurrence of substorm onsets and uses a simple Monte-Carlo model to show how 17 it can arise for an eccentric field model from the effect of the diurnal motions of Earth's 18 poles on the part of the geomagnetic tail where substorms are initiated. These motions 19 are in any reference frame that has an X axis that points from the centre of the Earth 20 to the centre of the Sun and are caused by Earth's rotation. The premise behind the model 21 is shown to be valid using a super-posed epoch study of the conditions leading up to on-22 set. These studies also show the surprising degree of preconditioning required, ahead of 23 the growth phase, for onset to occur. A key factor is the extent to which pole motions 24 caused by Earth's rotation influence the near-Earth tail at the relevant X coordinate. 25 Numerical simulations by a global MHD model of the magnetosphere reveal the required 26 effect to generate the observed UT variations and with right order of amplitude, albeit 27 too small by a factor of about one third. Reasons why this discrepancy may have arisen 28 for the simulations used are discussed. 29

³⁰ Plain Language Summary

Earth's magnetic field is eccentric in that the main magnetic (dipole) axis does not pass through the centre of the Earth. This introduces a wobble into many aspect of near-Earth space as Earth rotates. Many consequences of this have been noted in previous papers. This paper investigates the effect of the eccentricity on the phenomenon of magnetospheric substorms. It is shown that the explosive releases of energy stored in tail are more likely to start ("onset") at some Universal Times (and therefore geographic longitudes) than others and an explanation of why is provided.

38 1 Introduction

39

1.1 Universal Time variations in the magnetosphere

Lockwood and Milan (2023) have recently reviewed Universal Time (UT) varia-40 tions in magnetospheric observations and indices. Their study included: the am plan-41 etary geomagnetic index (Mayaud, 1972; Lockwood et al., 2019); the SML auroral elec-42 trojet index (Newell & Gjerloev, 2011a, 2011b); the SMR partial ring current indices (Newell 43 & Gjerloev, 2012); the polar cap indices (Stauning, 2007; Troshichev, 2022), transpolar 44 voltage observations from Low-Earth Orbit (LEO) spacecraft (e.g., Hairston & Heelis, 45 1993; Boyle et al., 1997), Φ_{PC} ; field aligned-current maps derived from measurements 46 by magnetometers on the Iridium LEO satellites by the AMPERE (Active Magnetosphere 47 and Planetary Electrodynamics Response Experiment) project (Coxon et al., 2018); and 48 substorm onset occurrence (Forsyth et al., 2015; Newell & Gjerloev, 2011a, 2011b). In 49 addition, Lockwood et al. (2021) have modelled the UT variations in the am index and 50 its hemispheric sub-indices an and as and Lockwood et al. (2023) have studied at how 51 UT variations in the magnetosphere-ionosphere-thermosphere coupled system influence 52 the upper atmosphere Joule heating response to terrestrial Coronal Mass Ejection (CME) 53 impacts. 54

UT effects arise in the coupled magnetosphere-ionosphere-thermosphere system because the Earth's magnetic poles are offset from its rotational axis. The most commonly used model of the intrinsic field of Earth is a geocentric dipole, for which this offset is the same in the two hemispheres. This means effects of Earth's rotation in the northern polar regions are equal and opposite to those in the southern polar regions and taking a global average means that many effects cancel and show no net UT variation. How-

ever, constraining Earth's magnetic dipole axis pass through the centre of the Earth is 61 only a useful approximation and eccentric dipole models show that this is not generally 62 valid. The standard way of describing an eccentric dipole, introduced by (Bartels, 1936), 63 is to use the first 8 coefficients that define a spherical harmonic expansion of the magnetic scalar potential, such as the International Geomagnetic Reference Field IGRF (Thébault 65 et al., 2015). This is compared to the first three used to define a centered dipole. In such 66 models the "axial" poles (where the dipole axis threads the Earth surface) are offset from 67 the rotational axis by different amounts in the two hemispheres and these magnetic poles 68 are not separated by 180° in longitude as they are for a geocentric dipole. The eccen-69 tric dipole model of (Koochak & Fraser-Smith, 2017a) gives the latitudinal offset of the 70 axial magnetic pole and the rotational pole of 8.23° in the northern hemisphere in 1980 71 and this fell to 5.91° in 2015. On the other hand, the corresponding values in the south-72 ern hemisphere were 15.29° in 1980 and 14.59° in 2015. Hence the ratio of the South/North 73 magnetic pole offsets has risen from 1.86 to 2.47 in just 35 years because the northern 74 magnetic pole has migrated towards the rotational axis. Many effects of the offset of the 75 rotational and magnetic poles in the two hemispheres that cancel for a geocentric dipole 76 do not cancel for an eccentric one leaving net UT variations. Thus the recent changes 77 in the Earth's intrinsic field mean that UT effects in the magnetosphere-ionosphere-thermosphere 78 system are of increasing importance. There are a number of potential effects discussed 79 in the following subsections. 80

1.2 Ionospheric conductivity effects

81

The most commonly-invoked effect of the offsets of the magnetic and rotational poles 82 is that of the changes in ionospheric conductivity at given polar and auroral locations 83 in geomagnetic coordinates. This is because of the changes in solar zenith angles χ at 84 such locations, which modulates the solar-EUV-generated ionospheric conductivities. This 85 effect has been invoked a great many times in the context of UT variations in geomag-86 netic activity (e.g. Lyatsky et al., 2001; Newell et al., 2002; Wang & Lühr, 2007). This 87 mechanism applies to enhanced conductivity that is generated by solar EUV illumina-88 tion (Ridley et al., 2004) and the effects at a given geomagnetic location are ordered by 89 time-of-year (here quantified by the fraction of a calendar year, F) and UT. However, 90 conductivity is also enhanced by particle precipitation. This second source is ordered in 91 magnetic coordinates and is highly variable in time (Carter et al., 2020). At certain places 92 and times, the precipitation source is dominant over the EUV source (Kubota et al., 2017). 93 Both EUV and precipitation effects show transient events, the former mainly due to so-94 lar flare effects and the latter associated with magnetospheric storms and substorms. In 95 both cases, strong UT variations occur as the event evolves but the timing of the events 96 are essentially random in the UT of their occurrence and so regular, systematic UT vari-97 ations are not seen. We have had good models of EUV-generated conductivity for many 98 years (e.g., Brekke & Moen, 1993) but the variability, in time and space, of precipitation-99 induced conductivity has made the development of equivalent models much more diffi-100 cult and complex (Zhang et al., 2015; Carter et al., 2020). 101

The dependence of EUV-generated conductivity at given geomagnetic coordinates 102 on solar zenith angle means there is a dependence on the dipole tilt angle δ with which 103 the Earth's magnetic axis is tipped towards the Sun. In the Solar Geocentric Ecliptic 104 (GSE) frame, the X axis points from the center of the Earth towards the center of the 105 Sun, the Z axis is the northward normal to the ecliptic and Y makes up the right hand 106 set (and so is antiparallel to Earth's orbital motion). In three dimensions, the Earth's 107 magnetic dipole axis \hat{M} makes an angle ψ with the GSE Z-axis and we here define the 108 dipole tilt angle δ to be the angle that the projection of $-\dot{M}$ onto the GSE XZ plane 109 makes with the Z axis. (Note that this definition means that positive δ means that the 110 northern magnetic pole is tilted towards the Sun and the southern away from it and neg-111 ative δ means the southern/northern pole is tilted towards/away from the Sun). Because 112 Earth's rotational axis is inclined at 23.44° with respect to the Z axis, this gives an an-113

nual contribution to the variation in δ of $\pm 23.44^{\circ}$ which depends on the fraction of the 114 calendar year, F. The present paper considers data for 1985-2021, the middle of that in-115 terval being 2003. In that year, Earth's geocentric dipole axis made an angle of 10.32° 116 with the rotational axis which gives an additional diurnal variation in δ of this ampli-117 tude, making the total range in δ over the year of $\pm 33.76^{\circ}$. For an eccentric dipole, off-118 sets of the north and south magnetic poles in 2003 were 6.81° and 14.96° , respectively, 119 which gives total ranges of δ of $\pm 30.25^{\circ}$ and $\pm 38.40^{\circ}$ for the north and south poles re-120 spectively. 121

122 Low values of $|\delta|$ form a characteristic pattern called the "McIntosh" or "equinoctial" pattern with F and UT. This pattern is also observed in geomagnetic activity, first 123 reported by McIntosh (1959) and frequently discussed since (for example Berthelier, 1976; 124 de La Sayette & Berthelier, 1996; Cliver et al., 2000; Lockwood, Owens, Barnard, Haines, 125 et al., 2020; Lockwood, McWilliams, et al., 2020; Lockwood et al., 2021). The equinoc-126 tial pattern is most clearly seen in the *am* index, which responds primarily to the sub-127 storm current wedge (Menvielle & Berthelier, 1991). The reason why am is the optimum 128 index for observing this pattern is that it has the most uniform F-UT response pattern 129 of all geomagnetic indices because it is constructed using homogeneous rings of stations 130 in both hemispheres with weighting function corrections to allow for any unavoidable lon-131 gitudinal inhomogeneities in the siting of stations due to oceans (Lockwood et al., 2019). 132

Low δ gives larger solar zenith angles χ at high latitudes which gives lower values 133 in EUV-generated ionospheric conductivity (Moen & Brekke, 1993; Ridley et al., 2004). 134 However, the conductivity pattern depends on δ and not $|\delta|$ and so it is not obvious how 135 conductivities could generate an equinoctial pattern in geomagnetic activity. The pro-136 posal of Lyatsky et al. (2001) and Newell et al. (2002) is that global geomagnetic activ-137 ity is enhanced when the midnight sector of both auroral ovals, where substorms are ini-138 tiated, are in darkness at E-region heights (solar zenith angles χ greater than about 101°) 139 and so have a lower conductivity, and this only occurs when $|\delta|$ is small. Alternatively, 140 the conductivity variation with χ proposed by Nagatsuma (2004) has, due to slant path 141 effects, a minimum at $\chi = 90^{\circ}$ (which would be more common at low $|\delta|$). However, 142 this minimum is not present in the models and observations of Brekke and Moen (1993), 143 Moen and Brekke (1993) and Ridley et al. (2004). 144

It should be noted that, as discussed in the following subsections, EUV-enhanced conductivities in polar regions is far from the only proposed mechanism by which the *F-UT* equinoctial pattern of $|\delta|$ can be imprinted on global geomagnetic activity.

148

1.3 Dipole tilt effects in the geomagnetic tail

The near-Earth tail is orientated with respect to the Earth's magnetic axis whereas the mid-tail and far-tail regions are orientated with respect to the solar wind flow (with a small aberration due to Earth's orbital motion). Consequently, between the near-Earth and the mid-tail regions the tail bends through the "hinge angle" which is very close to being the same as the dipole tilt angle δ . Hence this tail hinge angle also shows the equinoctial pattern.

Kivelson and Hughes (1990) proposed that the hinge angle plays a role in the sta-155 bility of the tail and the triggering of substorm onsets, an idea investigated further by 156 a number of authors (Danilov et al., 2013; Kubyshkina et al., 2015, 2022; Korovinskiy 157 et al., 2018). To fit the observations, substorm occurrence and strength (and hence also 158 global geomagnetic activity) would need to be enhanced when the hinge angle is small 159 160 (i.e., when $|\delta|$ is small). A variant of this idea was proposed by Alexeev et al. (1996) and Ou et al. (2022) who suggested the dipole tilt effect was through a change in the prox-161 imity of the ring current and the closest auroral electrojet. 162

A different mechanism for generating the equinoctial pattern in the geomagnetic 163 tail has been proposed by Lockwood, McWilliams, et al. (2020); Lockwood, Owens, Barnard, 164 Watt, et al. (2020). This uses the fact that the dipole tilt influences how quickly open 165 field lines are appended to the tail because of the shift with δ in the magnetic latitude 166 of the magnetic reconnection site in the dayside magnetopause, as has been modelled in 167 numerical MHD simulations (Park et al., 2006; Hoilijoki et al., 2014; Lockwood, Owens, 168 Barnard, Watt, et al., 2020; Eggington et al., 2020) and also observed in satellite data 169 (Trattner et al., 2012; Zhu et al., 2015; Kitamura et al., 2016). In the hemisphere in which 170 the dipole axis is tipped toward the Sun ($\delta > 0$ for the northern hemisphere), open field 171 lines take longer than those in the other hemisphere or for when $\delta = 0$: this is because 172 they have further to travel and because, initially, the open field lines are moving under 173 the magnetic curvature force against, rather than with, the magnetosheath flow. As a 174 result, a larger fraction of the open flux threads the dayside magnetopause sunward of 175 a given X in the tail in the hemisphere tipped towards the Sun (and hence a smaller frac-176 tion threads the tail lobe at that X). Numerical simulations show that the total field, in 177 both lobes, is smaller for larger $|\delta|$ and so the magnetic shear across the cross-tail cur-178 rent sheet is greatest for $\delta = 0$ and this too yields an equinoctial F-UT pattern (Lockwood, 179 Owens, Barnard, Watt, et al., 2020). This mechanism is supported by the observation 180 that the equinoctial pattern is enhanced by solar wind dynamic pressure which also en-181 182 hances the magnetic shear across the near-Earth cross-tail current sheet by squeezing the near-Earth tail (Lockwood, McWilliams, et al., 2020; Lockwood, Owens, Barnard, 183 Watt, et al., 2020). 184

1.4 Ion-neutral momentum exchange

There are other effects of the Earth's dipole tilt. The dynamics of ionospheric plasma 186 is ordered relative to the geomagnetic pole whereas the dynamics of the neutral thermo-187 spheric gas is ordered relative to the rotational pole. Both ion-neutral and electron-neutral 188 collisions contribute to ionospheric conductivities, but ion-neutral collisions have an ad-189 ditional role in momentum exchange between the ionosphere and thermosphere (specif-190 ically ions because their greater mass means that they carry much greater momentum 191 than electrons). As a result, plasma convection influences thermospheric winds which, 192 in turn influence the deposition of energy because ion-neutral frictional heating depends 193 on the vector difference between the velocities of ions and neutrals. Hence both the wind 194 response and the effect on energy deposition depend on UT (see review in Wang et al., 195 2017). An important factor in these effects is temporal variability in the ionospheric con-196 vection because the greater number densities of neutrals atoms compared to ions, results 197 in the response times of thermospheric winds to changes in ionospheric flow being larger 198 than the response times of ionospheric flows to changes in magnetospheric dynamics (Lockwood 199 et al., 1988; Zou et al., 2021). Förster and Cnossen (2013) noted that the hemispheric 200 intrinsic magnetic field differences were probably more important for polar thermospheric 201 neutral winds than ionospheric plasma convection but can still influence currents, con-202 vection and power dissipation rates in the upper atmosphere and have implications that 203 have been invoked by Chossen et al. (2012), Förster and Chossen (2013) and Laundal 204 et al. (2017). 205

206

185

1.5 The Russell-McPherron effect

The Russell-McPherron (R-M) effect (Russell & McPherron, 1973) is central to understanding the semi-annual variation in geomagnetic activity. A review of the evidence for this mechanism and of its influence has recently been given by Lockwood, Owens, Barnard, Haines, et al. (2020) and Lockwood, McWilliams, et al. (2020). The R-M effect arises because the IMF is ordered, on average, in a solar frame (the Parker Spiral configuration) but coupling into the magnetosphere depends in its orientation relative to Earth's magnetic dipole axis (in a frame such as Geocentric Solar Magnetospheric,

GSM). The most appropriate solar frame is the Geocentric Solar Equatorial (GSEQ). 214 The key effect is that the Earth's dipole tilt means that at the March equinox, negative 215 IMF $[B_Y]_{GSEQ}$ gives a southward IMF component in GSM (hence enhancing solar wind-216 magnetosphere coupling) whereas at the September equinox it is positive $[B_Y]_{GSEQ}$ that 217 does this. Geomagnetic activity shows, very clearly and very strongly, this preference 218 for high geomagnetic activity at one or other equinox, depending on the polarity of the 219 $[B_Y]_{GSEQ}$ component (Zhao & Zong, 2012; Lockwood, Owens, Barnard, Haines, et al., 220 2020; Lockwood, McWilliams, et al., 2020). This confirms the key importance of the R-221 M effect. The diurnal dipole tilt variation due to Earth's rotation means that the Septem-222 ber peak (for $[B_Y]_{GSEQ} > 0$) is at around 10hrs UT (with a minimum around 22 hrs 223 UT) whereas the March peak (for $[B_Y]_{GSEQ} < 0$) is at around 22 hrs UT (with a min-224 imum around 10 hrs UT). 225

226

1.6 Other dipole tilt effects on magnetopause reconnection voltage

The R-M effect has a characteristic F-UT pattern which is quite different to the 227 equinoctial pattern in $|\delta|$. Hence the R-M effect does not generate the equinoctial pat-228 tern. Another proposal to explain the observed equinoctial pattern in geomagnetic ac-229 tivity is that the magnetopause reconnection voltage Φ_D varies with the dipole tilt (Crooker 230 & Siscoe, 1986; Russell et al., 2003). However, (Finch et al., 2008) analysed the F-UT231 patterns in data from a very large number of individual magnetometer stations and showed 232 that the equinoctial pattern arises in the nightside auroral oval and that it was absent 233 absent in data from dayside stations. Similarly, (Lockwood, Owens, Barnard, Haines, 234 et al., 2020) and (Lockwood, McWilliams, et al., 2020) used the mid-latitude $a\sigma$ indices, 235 which cover 6-hour ranges in Magnetic Local Time (MLT) and showed the equinoctial 236 pattern was strongest in the midnight sector but hardly detectable in the noon sector. 237 This argues against the equinoctial pattern being generated by dipole tilt effects on day-238 side magnetopause coupling and the magnetopause reconnection voltage Φ_D . These re-239 sults strongly indicate that the equinoctial pattern in indices such as *am* is not consis-240 tent with dipole tilt modulation of the reconnection rate in the dayside magnetopause. 241 However, this does not mean that such effects do not occur and numerical simulations 242 by global MHD models have found dipole tilt modulation of magnetopause reconnection 243 voltage; however, Figure 7a of Eggington et al. (2020) shows that the modelled Φ_D vari-244 ation with δ is in the wrong sense to explain the equinoctial pattern of enhanced geo-245 magnetic activity. The effect of dipole tilt on the magnetopause reconnection voltage is 246 discussed further in Section 6. 247

248

1.7 Inductive effect of pole motions

Recently another mechanism has been added to this list. This is, in effect, a dif-249 ferent manifestation of the effect of dipole tilt on the evolution of open flux tubes into 250 the tail proposed by Lockwood, Owens, Barnard, Watt, et al. (2020) and that was dis-251 cussed in Section 1.3. Lockwood et al. (2021) have noted that models and observations 252 show that the ionospheric polar caps and auroral ovals undergo almost the same diur-253 nal sunward and antisunward sequence of motion due to Earth's rotation as the geomag-254 netic pole in a geocentric-solar frame (meaning any frame that has an X axis that points 255 from the centre of the Earth to the centre of the Sun, such as GSE, GSM and GSEQ). 256 At first sight the velocities of these motions appear negligible, being smaller than typ-257 ical solar wind flow speeds in the same frame by a factor of order 2×10^{-4} . However, the 258 flow-transverse magnetic field is larger in the ionosphere than in interplanetary space by 259 a factor that is typically 10^4 and hence in terms of electric fields and voltages the pole 260 motions give values that are typically about half those in interplanetary space. 261

As demonstrated by (Kabin et al., 2004), the effect of dipole tilt on the location of the open-closed field line boundary is readily seen in simulations made by numerical, global, MHD models of the magnetosphere. Figure 1 shows simulations by the SWMF

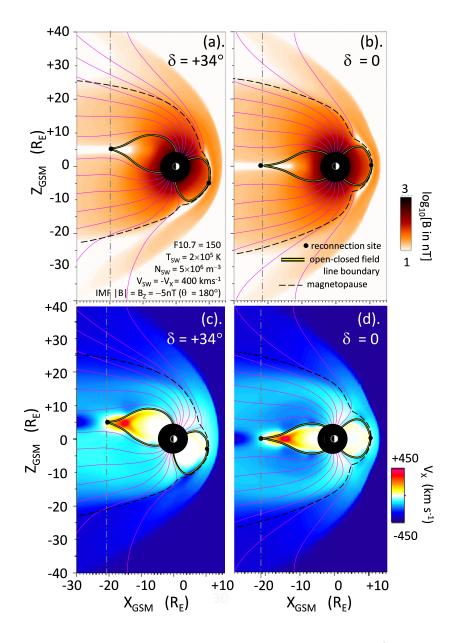


Figure 1. Numerical MHD model results from the SWMF model (version v20140611 - also known as BATSRUS) for run time 90 min in the simulations described by (Lockwood, Owens, Barnard, Watt, et al., 2020). Note these simulations use a geocentric dipole model of the Earth's intrinsic field. The plots show noon-midnight cuts in the GSE XZ plane (Y=0), parts a and b give color contours of the magnetic field strength, B (on a logarithmic scale) and parts c and d give colour contours of the sunward flow speed, V_X . Parts a and c are for a dipole tilt of $\delta = +34^{\circ}$ and parts b and d are for $\delta = 0$. The magnetopause, defined from the plasma beta, flow and the magnetopause current in the Y direction, is shown as dashed lines and reconnection sites, identified by polarity flips in fast flows in the relevant direction, by black dots. The black and yellow line is the open-closed field line boundary. In addition, open magnetic field lines, reconnected 4 min apart, are shown in mauve. The vertical grey dot-dash line is at the X value of the tail reconnection X-line (at Y=0) which is at $X = -20.5R_E$ for $\delta = +34^{\circ}$ and $X = -21R_E$ for $\delta = 0$.

numerical MHD model (version v20140611, also known as BATSRUS) with a geocen-265 tric dipole model of the intrinsic geomagnetic field. The solar wind at (and before) the 266 run time used here (90 min) was steady at $400 km s^{-1}$ with an IMF pointing due south-267 ward in the GSM frame and of magnitude 5nT. The solar wind number density was 3×10^6 268 m^{-3} and the mean ion mass 1.1 amu. Using the empirical relation by Lockwood and McWilliams 269 (2021a), the predicted magnetopause reconnection voltage Φ_D is constant at 56kV. Note 270 that in order to isolate the effects of the dipole tilt angle δ , these simulations were car-271 ried out with two fixed values of δ (0 and 34°) and not one that varies with UT. Note 272 also that the model has been run over 90 min to give a near steady-state with the effect 273 of initial conditions removed. 274

Figure 1 shows noon-midnight cuts (i.e., in the XZ plane of the GSE frame) of the 275 modelled structure in field strength (top panels) and antisunward flow speed (bottom 276 panels) with the left-hand panels for a dipole tilt of $\delta = +34^{\circ}$ and the right-hand pan-277 els for $\delta = 0$. Plots for $\delta = -34^{\circ}$ are not shown because, for the geocentric dipole used. 278 the results for the northern hemisphere are the same as for the southern for $\delta = +34^{\circ}$. 279 The magnetopause is shown by the black dashed line and the X value of the tail recon-280 nection site by the vertical grey dot-dash line. The mauve lines are open field lines that 281 were reconnected 4 minutes apart. The symmetry of the $\delta = 0$ case means that the open 282 field line motion into the tail is the same in the two hemispheres and Figure 1d shows 283 that in both hemispheres open field lines have the same antisunward speed at the mag-284 netopause at all X and that in both hemispheres open field lines take about 12.5 min 285 for the point where they thread the magnetopause to reach the X coordinate of the tail 286 reconnection site $(X \approx -21R_E)$: as a result, in Parts b and d for both hemispheres the 287 two most recently-reconnected field lines shown thread the magnetopause sunward of this 288 X value, and the other 5 of the open field lines shown are appended to the tail lobe by 289 this X: hence roughly $(5/7) \approx 70\%$ of the open flux is appended to both tail lobes at this 290 X in this case. 291

Parts a and c of Figure 1 show how radically the dipole tilt alters this hemispheric 292 symmetry. The field lines in the northern hemisphere reach a flow speed of $V_X = 200 km s^{-1}$ 293 at a GSE latitudes near 80° latitude (approximately 12 min after reconnection) whereas 294 those in the southern hemisphere reach it at near 45° (after only 2.5 min). This is be-295 cause the shift of the magnetopause reconnection site into the southern hemisphere means 296 that for southern hemisphere open field lines the sheath flow and the tension force act 297 together to move open flux tailward whereas initially the sheath flow is opposing the mo-298 tion of northern hemisphere open flux towards the tail. As a result of this hemispheric 299 difference in open flux evolution, only 4 out of the 7 open field lines are inside the tail 300 lobe at the X of the tail reconnection site (approximately 60%) in the northern hemi-301 sphere, whereas in the southern hemisphere this figure is 6 out of 7 (approximately 86%). 302

The tilt of $\delta = 34^{\circ}$ used in Figure 1 is an extreme deviation from $\delta = 0$, slightly larger than the peak-to-peak diurnal variation of the southern ionospheric polar cap over 12 hours of 29.92° (for the pole offset in an eccentric dipole in 2003) and a bit over twice the corresponding diurnal range for the northern polar cap of 13.62°. However it clearly demonstrates how the polar caps move sunward and antisunward with the value of δ . The model runs shown in Figure 1 will be used in Section 5 to check that a best-fit value of a parameter used in this paper (R_X , defined in Section 2.1) is reasonable.

There is also diurnal motion of the ionospheric polar caps in the Y-direction, but this is different in the GSE, GSM and GSEQ frames as they differ in their Y-axis definition; however, they share the same X axis and so the polar cap motion in this direction (towards/away from the Sun) is the same in all these frames and here termed V_P (V_{PN} in the Northern hemisphere, V_{PS} in the southern). Assuming there is no change in the polar cap shape, the voltage across the polar cap generated by these pole motions in all three frames is

$$\phi = V_P B_i d_{PC} \tag{1}$$

where B_i is the ionospheric magnetic field and d_{PC} is the maximum diameter of the po-317 lar cap in the dawn-dusk direction, perpendicular to X. Note that d_{PC} , V_P and B_i are 318 all values for the same altitude. We define V_P as positive for motion towards the Sun 319 which is in the opposite direction to the solar wind flow (which is close to the -X direc-320 tion). For this definition, the voltage ϕ given by Equation 1 is subtracted from that gen-321 erated across the polar cap by the solar wind flow because it is positive when the po-322 lar cap is moving sunward. Using the Expanding-Contracting polar cap model of iono-323 spheric convection excitation (Cowley & Lockwood, 1992; Milan et al., 2021; Lockwood 324 & McWilliams, 2021b; Lockwood & Cowley, 2022), the total voltage across the polar cap 325 allowing for this pole motion effect becomes 326

$$\Phi_{PC} = f_D \Phi_D + f_N \Phi_N + \Phi_V - \phi \tag{2}$$

where Φ_D is the reconnection voltage in the subsolar dayside magnetopause (the rate 327 of production of open flux), Φ_N is the reconnection voltage in the cross-tail current sheet 328 that is between open flux in the tail lobes (the rate of loss of open flux), Φ_V is the "viscous-329 like" voltage induced by all non-reconnection mechanisms of solar wind-magnetosphere 330 interaction. The factors f_D and f_N are the fractions of reconnection voltages (Φ_D and 331 Φ_N , respectively) placed across the maximum diameter of the polar cap. These factors 332 depend upon the shape of the polar cap and how it is changing: for the approximation 333 of a polar cap that remains circular at all times $f_D = f_N = 0.5$ (Lockwood, 1993) but 334 in general the polar cap boundary shape is always evolving (Tulegenov et al., 2023) and 335 so the factors f_D and f_N are not constant. 336

Figure 2 looks at the implications of these pole motions by considering a Faraday 337 loop PASGUC that is fixed in the GSM frame (shown by the vellow dashed line). The 338 segment PC is the polar cap diameter and the voltage across (i.e. the magnetic flux trans-339 fer rate across it) is $\Phi_{PC} = V_i B_i d_{PC}$ where V_i is the plasma and frozen-in field veloc-340 ity across it. The segment SG is just outside the bow shock in interplanetary space (some-341 times referred to as the "Stern Gap") and the voltage across it is $\Phi_{SG} = V_{SW} B_Z d_{SG}$, 342 where V_{SW} is the solar wind speed in the -X direction, B_Z is the interplanetary mag-343 netic field (IMF) component in the GSM Z direction and d_{SG} is the spatial separation 344 of S and G in the GSM Y direction (the width of the Stern gap). The segments of the 345 loop PAS and GUC are the open field lines on the dawn and dusk extremities of the po-346 lar cap and neglecting any field-aligned voltages (that will be very small compared to 347 Φ_{SG} and Φ_{PC}), Faraday's law tells us the difference in the flux transfer rates $\Phi_{SG} - \Phi_{PC}$ 348 is equal to the rate of growth of flux threading the loop PASGUC. Because the solar wind 349 and relevant sheath flow are supersonic and super-Alfvénic, the solar wind flow and volt-350 age Φ_{SG} is not influenced by any change in Φ_{PC} caused by the pole motion. Hence, in 351 addition to reducing the transpolar voltage Φ_{PC} by ϕ , the effect of a sunward pole mo-352 tion $(\phi > 0)$ is to increase the lobe flux by ϕ . 353

Hence the diurnal cycle of sunward and then antisunward pole motion caused by the rotation of the Earth generates a diurnal cycle of decrease then increase of the ionospheric transpolar voltage with an associated cycle of increase and then decrease in the rate at which open flux is added to the tail lobe.

1.8 Universal Time variations

Many of the effects discussed above generate systematic UT variations when a subset of the data are considered but not when averages of all data are considered. For example, the R-M effect generates UT variations if we consider the two polarities of the

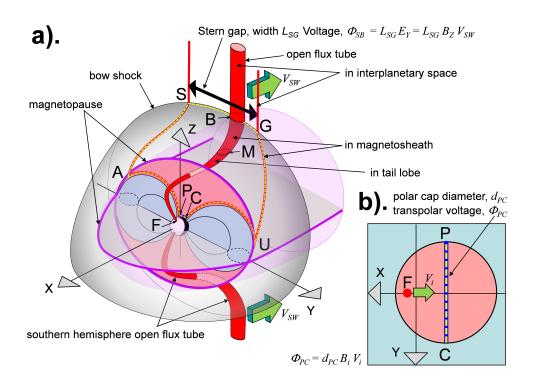


Figure 2. (a). Schematic of inductive decoupling of the "Stern Gap" voltage across open field lines in interplanetary space, Φ_{SG} and the transpolar voltage in the ionosphere Φ_{PC} . The magnetosphere is here viewed from northern middle latitudes in the mid-afternoon sector. The loops PASGUC (shown by the yellow dashed line) and PAUC (enclosing the northern tail lobe cross-section shaded pink) are fixed in the XYZ GSM frame, where P and C are the dawn and dusk extremes of the northern ionospheric polar cap, AP and UC are field-aligned in the magnetosphere, SA and GU are field-aligned in the magnetosheath, SG lies in the bow shock and AU in the tail magnetopause. The red flux tubes are open field lines and the northern-hemisphere tube threads the bow shock at B and the magnetopause at M and has an ionospheric footpoint, F. The solar wind flow is in the -X direction at speed V_{SW} . (b) is a view looking down (in the -Zdirection) on the northern hemisphere polar cap in which the antisunward ionospheric convection velocity of the footpoint F is V_i . After Lockwood and Milan (2023).

IMF separately, but because the distribution of IMF B_Y values is very close to symmetric around zero, the effects of the two polarities almost completely cancel in a full dataset and so the R-M effect does not give a net systematic UT variation if all data are considered.

Indeed, because the dipole tilt angle averages to zero over a full year, this is true for any mechanism that depends linearly on the dipole tilt. However, EUV-induced ionospheric conductivities have a non-linear dependence on solar zenith angle and hence on the dipole tilt. This means that the conductivity effects can give a net systematic UTvariation even after averaging over a whole number of years. However, this depends on location, as demonstrated by Figure 6 of Lockwood and Milan (2023).

The pole-motion effect is different because the diurnal variation of the sunward velocities V_{PN} and V_{PS} are almost independent of the time of year (Lockwood et al., 2021) and so their diurnal effect is not reduced or eliminated by averaging over a whole number of years.

Because the offset of the rotational and magnetic pole in the southern hemisphere 376 is approximately twice that in the northern, the amplitude of the sinusoidal variation 377 in the pole motion speed V_{PS} is approximately twice that in V_{PN} and so the effects on 378 ionospheric transpolar voltage and lobe flux growth rate are roughly twice as large in 379 the south than the north. In addition, whereas the sinusoidal variations would be in ex-380 act antiphase (and of equal amplitude) for a geocentric dipole model of the field (and 381 hence would be equal and opposite and so cancel at any one time), the longitudinal sep-382 aration of the axial poles for an eccentric dipole is not 180° and the hemispheric vari-383 ations are not in exact antiphase as well as being different in amplitude. Thus there is 384 a net UT variation for a global average for an eccentric dipole that is absent for a geo-385 centric dipole. The longitudinal separation of the poles from the Koochak and Fraser-386 Smith (2017b) eccentric dipole model has fallen from 152° in 1985 to 145° in 2015. This 387 means that the phase difference between the sinusoidal variations in V_{PS} and V_{PN} has 388 decreased from 0.85π to 0.81π , compared to the constant value of π for a geocentric dipole. 389

³⁹⁰ 2 The effect of pole motions on substorm growth phases

391

392

2.1 A simple Monte-Carlo model of substorm growth phases and onsets

Lockwood and Milan (2023) have recently proposed a simple Monte-Carlo model 393 of how pole motions influence substorm growth phases and so introduce a UT variation 394 into substorm onset occurrence. This section refines that model slightly and Section 3 395 provides an independent test of the concepts it is based on. In this model, the magne-396 topause reconnection voltage Φ_D is assumed constant and, because we are aiming to re-397 produce average behaviour, we use the overall average $\langle \Phi_D \rangle$ of 24 kV. In Lockwood and 398 Milan (2023), the night ide reconnection voltage Φ_N was also held constant. In the present 399 paper the linear open flux loss found by Lockwood et al. (2023) for times of small |SML|400 is used, with the loss time constant of $\tau_N = 6.8$ hrs $= 2.448 \times 10^4$ sec reported in that 401 paper. Thus the open flux continuity equation for the growth phases simulated is 402

$$dF_{PC}/dt = \Phi_D - \Phi_N = \Phi_D - F_{PC}/\tau_N \tag{3}$$

The questions then arise 'when do growth phases end?' and 'what triggers substorm onset?'. This has been discussed for many years and many mechanisms proposed (Spence, 1996; Lyons et al., 2018; Milan et al., 2019; Tanaka et al., 2021). To determine when onset occurs, the model uses the concept from the analysis of F_{PC} values at the time of onset by Boakes et al. (2009): this does not define the precise time of onset but does give us a usable statistical relationship. These authors found that for values of F_{PC} below ⁴⁰⁹ 0.3*GWb*, the probability of a substorm onset occurring was negligible but that as F_{PC} ⁴¹⁰ rose above this level the probability increased linearly and was undefined above 0.9*GWb*. ⁴¹¹ Lockwood and Milan (2023) took the probability of onset to become unity at $F_{PC} = 1.2$ GWb, ⁴¹² the maximum possible open flux estimated by Mishin and Karavaev (2017). The impli-⁴¹³ cation is that the magnitude of the open flux F_{PC} that causes onset through its effect ⁴¹⁴ on the total lobe flux in the tail and hence the magnitude of the cross-tail current. The ⁴¹⁵ flux in one tail lobe, $[F_{lobe}]_X$, at a given (negative) value of X in the tail, is given by

$$[F_{lobe}]_X = F_{PC} - F_X \tag{4}$$

where F_X is the open flux connected to the ionospheric polar cap in that hemisphere that still threads the dayside magnetopause sunward of X. Differentiating with time t gives

$$d[F_{lobe}]_X/dt = dF_{PC}/dt - dF_X/dt$$
(5)

The pole motion influence on F_X depends on the value of X considered and will decline with distance away from the Earth down the tail. We can allow for this with a factor that depends on X, R_X , which is the ratio $(dF_X/dt)/\phi$,

$$d[F_{lobe}]_X/dt = dF_{PC}/dt - R_X\phi \tag{6}$$

⁴²² The factor R_X will, in general, depend on how much of the open flux was recently ⁴²³ opened and hence the prior history of the voltage Φ_D . However, the constant Φ_D used ⁴²⁴ in this simple model means that R_X will be constant for a given X. Substituting from ⁴²⁵ equation 3 gives

$$d[F_{lobe}]_X/dt = \Phi_D - F_{PC}/\tau_N - R_X\phi \tag{7}$$

⁴²⁶ Note that Equation 7 applies to both hemispheres and that, because of Maxwell's ⁴²⁷ equation $\nabla . \vec{B} = 0$, Φ_D and F_{PC} are the same for both hemispheres, as is the loss time ⁴²⁸ constant τ_N , whereas we need to separately consider $(R_{XN}\phi_N)$ for the northern hemi-⁴²⁹ sphere and $(R_{XS}\phi_S)$ for the southern in order to compute the total tail lobe flux $[F_{tail}]_X$, ⁴³⁰ which is the sum of the north and south lobe fluxes at X, $[F_{lobe}]_{XN}$ and $[F_{lobe}]_{XS}$:

$$d[F_{tail}]_X/dt = d[F_{lobe}]_{XN}/dt + d[F_{lobe}]_{XS}/dt = 2\Phi_D - 2F_{PC}/\tau_N - R_{XN}\phi_N - R_{XS}\phi_S$$
(8)

The survey by Boakes et al. (2009) found that substorm onset probability increased 431 with the open flux F_{PC} . The model of substorm growth phases employed here uses the 432 equivalent of the Boakes et al. (2009) result but also allows for the open magnetic flux 433 that threads the dayside magnetopause, F_X and how it is influenced by the dipole tilt. 434 It is proposed that the probability of onset being triggered primarily depends on the level 435 of $[F_{tail}]_X$, rather than F_{PC} . In order to demonstrate the principle, the ratios (R_{XS} and 436 $(R_{XN}$ are taken to be equal and held constant. The value was varied and the optimum 437 fit to the observed UT variation of substorm onset (see Section 2.3) was found for $(R_{XS} =$ 438 $R_{XN} = 0.15$ for the X coordinate relevant to substorm onset. In Section 3 this value 439 is also shown to be consistent with a superposed epoch analysis of substorms onsets. 440

Because sequences of upstream IMF variation are independent of the phase of Earth's rotation, the model initiates each growth phase at a UT that is selected using a random number generator. The integration of Equation 8 is started from an initial tail lobe flux

(in each lobe) of $F_i = 0.2 GWb$ ($[F_{tail}]_X = 0.4 GWb$) which is consistent with typical 444 quiet time values of F_{PC} . Note that, in reality, this value will vary but that lowering F_i 445 increases the average length of the growth phases but does not influence the distribu-446 tion of onset UTs because the start UT values of growth phases are randomly selected. Using equation 3, the value of F_{PC} throughout the growth phase is also computed and 448 by assuming a circular polar cap this yields the polar cap diameter, d_{PC} (using the equa-449 tion by Lockwood et al. (2023), based on the work of Milan et al. (2021)). This is used 450 in Equation 1 to compute ϕ_N and ϕ_S at each time. The model calculates $[F_{tail}]_X$ ev-451 ery 1 second using Equation 8 and onset is determined to have occurred or not at each 452 time step using a random number generator constrained to select onset occurrence based 453 on the probability set by the $[F_{tail}]_X$ value. Note that there are three improvements in 454 the model used here, compared to that used by Lockwood and Milan (2023): (1) it al-455 lows for the effect of growth in F_{PC} on the open flux loss rate Φ_N and (2) it allows for 456 the effect of changing polar cap diameter d_{PC} on the pole-motion voltage ϕ (equation 457 1) and (3) it allows for the R_X factors. 458

This model is purely a model of substorm growth phases and onset and so cannot 459 reproduce the intervals between onsets, Δt_o , because they also include the durations of 460 the subsequent expansion and recovery phases (or alternatively the period of driven re-461 connection as discussed by Milan et al. (2021)) and any interval of quiet (northward IMF) 462 conditions between the substorms. Also notice that each substorm growth phase in the 463 model starts from the same initial tail flux $2F_i$ and at a randomly-selected UT. Hence 464 the model cannot account for recurrent substorms during periods of persistent south-465 ward IMF, where a growth phase of a substorm starts immediately after the recovery 466 phase of the prior substorm. 467

468 469

2.2 Effects of pole motions on transpolar voltages and the accumulation of magnetic flux in the tail lobes

Figure 3b and 3d show idealised variations that give an indication of how the pole 470 motions influence the transpolar voltage and the accumulation of lobe flux at the X rel-471 evant to onset. This plot is illustrative and for constant values of the reconnection volt-472 ages Φ_D and Φ_N . The value of Φ_N and of the polar cap diameter d_{PC} employed would 473 apply for a polar cap flux of $F_{PC} = 0.54 \ GWb$. The key point is that effects of the pole-474 motions in the two hemispheres are not of equal amplitude nor in perfect antiphase, as 475 they would be for a geocentric dipole. As a result, there is a sinusoidal variation in both 476 the average Φ_{PC} and the average $\Delta[F_{lobe}]_X$ which is the integral of $R_X \phi$ with time. Fig-477 ure 3c is for steady-state ($\Phi_D = \Phi_N$) whereas Figure 3d is for a growing polar cap with 478 $\Phi_D=24$ kV and $\Phi_N=22$ kV. Figure 3d shows that the net effect of the pole motions is 479 to reduce the rate at which flux is added to the tail, compared to the case without pole 480 motions (the dashed black line) between 2.5hrs UT and 14.5hrs UT but to enhance it 481 at all other UTs. 482

483

2.3 The UT distribution of substorm onsets

Figure 4a shows the histograms of the numbers of substorm onsets N_{α} in UT bins 484 0.5hrs wide, derived for 1985-2020 (inclusive) from the SML index and using the algo-485 rithm byForsyth et al. (2015) (hereafter FEA). The onset list by Newell and Gjerloev 486 (2011a, 2011b) (hereafter N&G) gives a very similar variation. The total number of sub-487 storm onsets ΣN_o is 88439 for the FEA list and 62532 for the N&G list. Hence the FEA 488 list is including more and smaller events that are not counted as distinct onsets in the 489 490 N&G list. Despite this difference, the distribution in UT is similar in the two cases with a large peak near 12hrs UT. This is broadly reproduced by the simple Monte-Carlo model. 491 as shown by the mauve lines in Figure 4a. In the model, this occurs because the slow-492 ing of the rate of accumulation of tail lobe flux means that more simulated growth phases 493 (that remember were started at randomly-chosen UTs) are reaching the required tail lobe

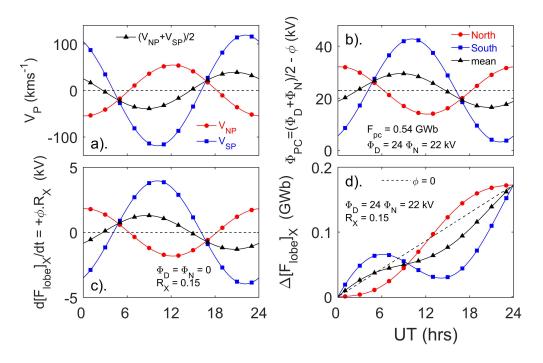


Figure 3. Plots of idealised Universal Time (UT) variations caused by pole motions. In all plots the red lines with red circle symbols are for the northern hemisphere polar cap, blue lines with blue square symbols are for the southern hemisphere polar cap and black lines with triangle symbols are for the global average of the two. Note that the symbols are added to aid readers with impaired colour vision and spaced considerably further apart than the UT resolution of the plots which is 1 min. Variations are based on the eccentric dipole model of Koochak and Fraser-Smith (2017b) for the year 2003. (a) the speed of sunward motion in the GSM frame of the geomagnetic poles at 120 km altitude in the E-region ionosphere, V_{NP} in the north, V_{SP} in the south and the average of the two in black. (b) The polar cap voltages Φ_{PC} from Equations 1 and 2 for constant dayside reconnection voltages of $\Phi_D = 24kV$ and a constant night voltage of $\Phi_N = 22$ kV (the value we would expect at low -SML activity levels for an open flux of $F_{PC} = 0.54 GWb$ for the linear loss dependence with time constant $\tau_N = 6.8 hrs$). The viscouslike voltage Φ_V is set to zero. For a circular polar cap this F_{PC} gives a polar cap diameter of d_{PC} = 3.71×10^6 m. (c) The contribution of the pole motions to the rate of accumulation tail lobe flux at X (for $R_X = 0.15$), $d[F_{lobe}]_X/dt = R_X \cdot \phi$ that would be the only change if steady state applied with $\Phi_N = \Phi_N$. (d) The total accumulation of lobe flux $\Delta[F_{lobe}]_X$ for the values of Φ_D , Φ_N in part (b). The dashed black line is for $\phi = 0$.

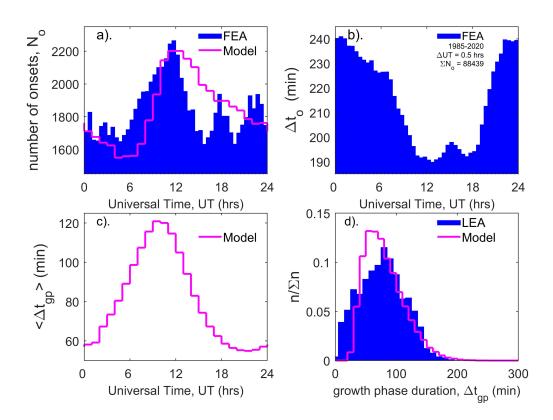


Figure 4. The blue histograms in the top panels show observed distributions with UT of (a) substorm onset times and (b) the interval after the prior onset from the list of such events compiled for 1985-2020 (inclusive) using the *SML* index and the algorithm by Forsyth et al. (2015). These plots both show a marked UT variation. The mauve line in (a) is the variation predicted by the simple Monte-Carlo model described in Section 2.1. (c) Means of the modelled growth phase duration in bins $\Delta UT = 1hr$ wide, $\langle \Delta t_{gp} \rangle$, as a function of UT. (d) The probability distribution of modelled growth phase durations Δt_{gp} (mauve line), where n is the number in bins 10min-wide bins and Σn is the total number (equal to 200,000 for the model simulations). Also shown by the blue histogram is the distribution for $\Sigma n = 368$ observed growth phase durations compiled by Li et al. (2013).

flux to give a high probability of onset at those UTs. After 12 hrs UT this number in 495 a set time falls as the rate of increase in tail flux increases. The observed mean time be-496 tween onsets Δt_o is shown by the blue histogram in Part b: as discussed in Section 2.1, 497 this cannot be reproduced by the model. Δt_o also shows a marked variation with UT: it decreases from near 4 hrs to close to 3 hrs over the interval 5-12 UT while the num-499 ber of onsets N_o rises. However after 12 UT it remains low even though N_o falls again. 500 This shows that although substorm onsets are rarer by 15 UT, the events that do oc-501 cur tend to recur in short succession. As discussed in Section 2.1, this behaviour can-502 not be captured in the model which restarts each growth phase at a random UT and so 503 it is not surprising the observed variation cannot be reproduced by the model at these 504 UTs in Figure 4a. However, the model does explain how the dipole tilt effect gives the 505 observed peak in onset occurrence at around 12 UT. 506

It is interesting to note what is happening in the growth-phase model. Initially the 507 open flux F_{PC} is low and so the night reconnection voltage Φ_N is considerably smaller 508 than the dayside voltage Φ_D . This means the polar cap flux grows rapidly. However, the 509 rise in F_{PC} increases the value of Φ_N and the rise in F_{PC} slows. Eventually the differ-510 ence between Φ_D and Φ_N becomes small and so the lobe flux variations due to the di-511 urnal pole motions and, in particular, the variations that they cause in $[F_{lobe}]_X$ become 512 significant. Hence although variations in $[F_{lobe}]_X$ due to the pole motions are small they 513 have a significant impact on when the total tail field $([F_{lobe}]_{XN} + [F_{lobe}]_{XS}$ reaches a 514 value that makes the probability of an onset occurring high. 515

Figure 4c presents the UT variation in the mean of the modeled growth phase du-516 rations Δt_{qp} . Unfortunately, we do not have a large observational database to compare 517 these predictions to. However, the plot confirms the above interpretation of the model 518 predictions, with the growth phases coming to an end at around 12 UT having greater 519 durations on average. Figure 4d shows the overall distribution of the 200,000 simulated 520 Δt_{ap} values (in mauve) is quite similar to that of the 368 values observed by Li et al. (2013) 521 (hereafter LEA), shopwn by the blue histogram. LEA divided the onsets into a high, medium 522 and low subsets of the interplanetary electric field, E_{SW} , and showed that the distribu-523 tion of Δt_{ap} values shifted to lower values for the larger E_{SW} cases, as we would expect. 524 The distribution shown by the blue histogram in Figure 4d is the total for all three E_{SW} 525 subsets. The mean value of the LEA distribution is 77 min which is close to the value 526 of 81 min for the modelled distribution. The major difference is that the modelled dis-527 tribution has fewer very short growth phases which suggests that either the initial to-528 tal lobe flux F_i is slightly too low or that the threshold tail flux of 0.6 GWb for the prob-529 ability of onset rising above zero is slightly too high. 530

⁵³¹ 3 Superposed epoch analysis of substorms

Section 2.3 shows that the simple Monte-Carlo model described in section 2.1, whilst 532 not fully modelling the observed UT variation of substorm onsets, provides an impor-533 tant insight into dipole tilt effects. In this section we look for more direct evidence of 534 such an effect using analysis of the variations in the SMU and SML geomagnetic indices 535 and in the magnetopause reconnection voltage estimated from interplanetary measure-536 ments, Φ_D , using a superposed-epoch analysis (also known as Chree analysis or composit-537 ing). This paper presents the plots made using the FEA onset list, but results for the 538 N&G list were similar. 539

Figure 5 presents superposed-epoch plots of the variations in (a) SML, (b) SMUand (c) Φ_D . The epoch time is relative to the times t_o of each of the 88439 substorm onsets in the FEA list for the years 1985 to 2020, inclusive. The mean value and the standard error in the mean are computed at epoch times $(t-t_o)$ between -240 min and +240 min in steps of $\delta t = 1$ min. This was repeated using randomly-selected epoch times t_o as a test of significance: because of the very large numbers of samples these random tests

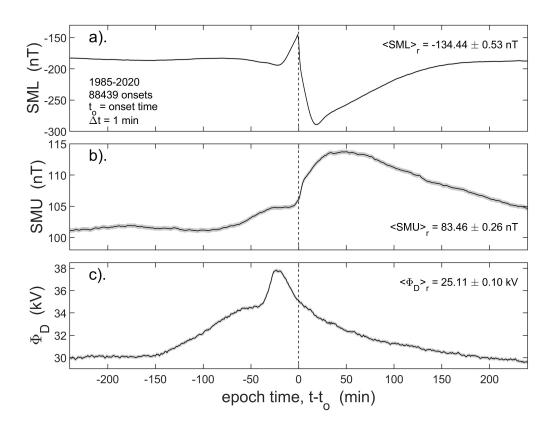


Figure 5. Superposed-epoch plots of substorms using the FEA list of substorm onsets for 1985-2020, inclusive. The mean value is shown as a function of epoch time $(t - t_o)$, where t is the observation time and t_o is the time of onset, for: (a) the *SML* index; (b) the *SMU* index; and (c) the estimated reconnection voltage, Φ_D , lagged by a nominal propagation lag of $\delta t_p =$ 19 min from the nose of the bow shock. The grey areas under the plotted black line are between plus and minus one standard error in the mean, but because of the very large number of samples (88439) these areas are smaller than the line width used for the case of *SML* and cannot be seen.

gave a completely flat variation: these are not shown in Figure 5 as values are considerably lower and so showing them suppresses detail in the plots for the real t_o ; however each plot gives the mean for the randomly-selected epoch times (respectively, $\langle SML \rangle_r$, $\langle SMU \rangle_r$ and $\langle \Phi_D \rangle_r$ in parts a, b and c), plus and minus the value of the mean of the corresponding standard errors. The randomly-selected onset values are shown in Figure 8 which presents the superposed-epoch plots at lower time resolution but over considerably larger ranges of epoch time, $(t - t_o)$.

In Figure 5, the black lines are the mean values over-plotted on top of grey bands 553 that are plus and minus the standard error in the mean. Because of the very large num-554 bers of samples, the gray band is hardly visible, especially for SML. The vertical black 555 dashed line is at epoch time $(t-t_o) = 0$. The Φ_D data have been lagged by a nominal 556 propagation lag of $\delta t_p = 19$ min from the nose of the bow shock. This value is appro-557 priate to the transpolar voltage Φ_{PC} and SML response to Φ_D (Lockwood & McWilliams, 558 2021b), but values near 30-40 min would be more appropriate to the delay before sub-559 storm onset and SML. Hence in relation to onset the Φ_D curve in part c may need to 560 be shifted to the left by an additional lag of about 10-20 min in some considerations. 561

The variation in SML in Figure 5a is as expected with some small changes in the 562 growth phase shortly before onset and a big perturbation to large negative values start-563 ing at onset. It should be remembered the onset times are determined from SML and 564 so we would expect SML to be well ordered by the onset times t_o derived from it. The 565 variation in SMU is also as expected with small increases in the growth phase and then 566 larger positive values after onset. Note that for the randomly-selected values of t_o the 567 values (almost identical at all epoch times) are $\langle SML \rangle_r = -134.44 \pm 0.53$ nT and so larger 568 (less negative) than for the real epoch times and values of $\langle SMU \rangle_r = 83.46 \pm 0.26$ are 569 considerably lower. Hence in all of the 8 hours of epoch time shown, the disturbance lev-570 els of SML and SMU are considerably above the overall average values. Similarly $\langle \Phi_D \rangle_n$ 571 is 25.11 ± 0.10 kV at all epoch times and so considerably lower than for the 8 hour-period 572 around substorm onset. 573

Figure 6 is the same as Figure 5c, but also shows the results for two one hour win-574 dows of the UT of the onset. The windows shown are 15-16 UT (in red) and 02-03 UT575 (in blue). These UT ranges are chosen as they give the maximum deviation either side 576 of the values for all onsets. The means are taken over Δt of 5 min (rather than the 1 min 577 used in Figure 5) because the higher time resolution is not needed and the 1-hour win-578 dows have fewer samples by a factor of roughly 24. The plot clearly shows that, on av-579 erage, larger Φ_D is needed ahead of substorm onsets at 15-16 UT than is needed ahead 580 of onsets at 02-03 UT. The difference between the two is roughly constant at about 4 581 kV at all negative values of $t-t_o$ shown and over that time this is a difference in opened 582 flux of 0.058 GWb which is of order 10% of an average open polar cap flux, F_{PC} (Milan 583 et al., 2008; Boakes et al., 2009). 584

At the start and end of the period shown Φ_D is 30 kV (4.9 kV above average) and 585 starts to rise above this at $t-t_o$ near -150 min. Thus the contribution of enhanced mag-586 netopause reconnection to the enhanced tail flux at onset, on average, begins at this time 587 and increases until about 1 hour before onset (for the nominal propagation lag of δt_p = 588 19 min). It then reaches a plateau for about half an hour before rising to a peak at t-589 $t_o = -25 \min$ (for the nominal $\delta t_p = 19 \min$). This marks the southward turning of the 590 IMF that is usually taken to be the start of the growth phase. However, the plot reveals 591 two levels of "preconditioning" by enhanced Φ_D before this time. The first is the 4.9 kV 592 by which Φ_D is elevated above average values 4 hours ahead of onset. The second is the 593 594 reconnection taking place in the 2 hours before ther inferred southward turning (between $t - t_o = -150$ min and $t - t_o = -30$ min on average). Thus the open flux gained only 595 between the southward turning and onset is not the only contribution to the tail lobe 596 flux at the time of onset. 597

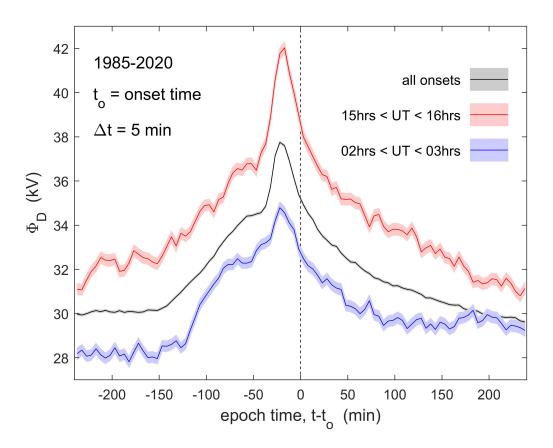


Figure 6. The same as Figure 5 but showing the values for onset UT between 15 and 16 hrs (in red) and between 02 and 03 hrs (in blue). The pink and pale blue shaded areas are plus and minus one standard error in the mean. The averages are here taken over $\Delta t = 5$ min windows in epoch time, $t - t_o$. The black line and grey shaded area is for all UT (also shown in Figure 5c).

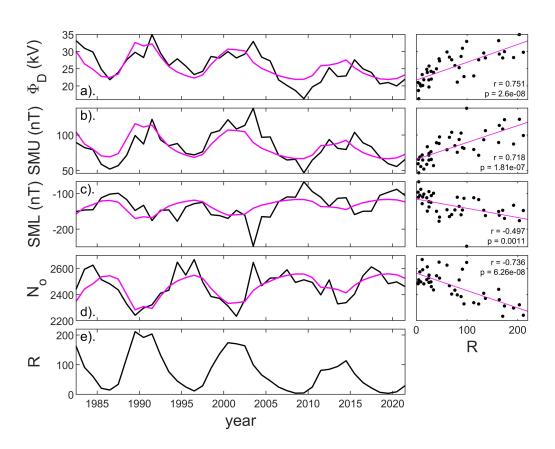


Figure 7. The left-hand column shows the Solar cycle variations in annual means (black lines) of: (a) the estimated magnetopause reconnection voltage, Φ_D ; (b) the *SMU* index; (c) the *SML* index; (d) the number of substorm onsets, N_o and (e) the international sunspot number, R. In panels a-d the mauve lines show the linear regression fit of R to the parameter. The right-hand column gives the scatter plots of the annual means with R, the mauve line being the linear regression fit. In each case, the correlation coefficient r and the p-value of the null hypothesis that there is no correlation are given.

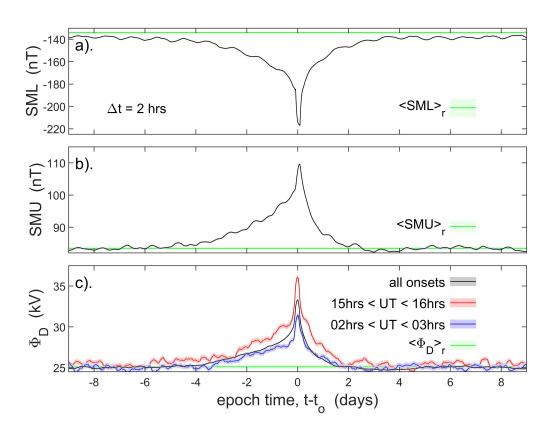


Figure 8. Super-posed epoch plots like those in Figures 5 and 6, but for integration intervals $\Delta t = 2$ hrs and covering epoch times $(t - t_o)$ between -9days and +9 days, where t is the observation time and t_o is the time of onset, for: (a) the *SML* index; (b) the *SMU* index; and (c) the estimated reconnection voltage, Φ_D , lagged by a nominal propagation lag of $\delta t_p = 19$ min from the nose of the bow shock. The black lines are the means for all data and grey areas are plus and minus one standard error in the means. The green lines are for randomly selected epoch times. In Part c, the red and blue lines are means of Φ_D for onset *UT* between 15 and 16 hrs (in red) and between 02 and 03 hrs (in blue): the pink and pale blue shaded areas are plus and minus one standard error in the means.

The first preconditioning, seen as the 4.9 kV by which Φ_D is elevated at $t-t_o =$ 598 -240 min appears be a solar cycle effect; however, Figure 7 shows that this is not the case. 599 Such an effect would arise if onsets were more frequent as higher solar activity, as one 600 might expect, and so the long-term averages of Φ_D , SMU and -SML would all be increased 601 above their overall means. Figure 7 plots the solar cycle variations in annual means for 602 the dataset used here (1985-2021) and although Φ_D , SMU and -SML are all correlated 603 with sunspot number R as we would expect, surprisingly, the number of onsets per year, 604 N_o is anticorrelated with more onsets occurring at sunspot minimum. (Note that SML605 not -SML is plotted in Figure 7 and that the anticorrelation for SML is weaker than the 606 other correlations (larger p value of the null hypothesis) largely because of the anoma-607 lous year 2003 for which the mean SML was exceptionally low. 608

Figure 7 shows that the enhanced Φ_D at the start of Figures 5 and 6 (over the over-609 all mean value which is very close to the value for random selection of epoch times be-610 cause the number of onsets is so high) is not due to the solar cycle variation in the num-611 bers of onsets. Figure 8 looks at the origin of this by extending the interval covered by 612 the superposed epoch study and including the plots for the random selection of epoch 613 times (the green lines with pale green areas showing plus and minus one standard error; 614 however, in most cases these are smaller than the line width and not visible). In these 615 plots the averaging interval was increased to $\Delta t = 2$ hrs. Part a shows that at epoch times 616 well away from onset $t-t_o = -9$ days and $t-t_o = +9$ days, SML is very close to is over-617 all mean and the randomly sampled value $\langle SML \rangle_r$. Part b shows the same is true for 618 SMU, the average vale being found at $(t - t_o) < -5$ days and $(t - t_o) > +2.5$ days. The 619 black line in part c shows that Φ_D is the same as its randomly-selected mean for (t - t)620 t_o <-5 days and that the variation for 15-16 UT is not elevated above that for 02-03 621 UT for $(t - t_0) < -6$ days. Hence the UT variation in the voltage needed to cause an 622 onset depends, to some degree, on a preconditioning (by prior magnetopause reconnec-623 tion) of the substorm growth phase over an interval of about 6 days before the south-624 ward turning that traditionally marks the start of the growth phase. The average effect 625 of that preconditioning can be seen to increase considerably after $(t-t_o) = -2.5$ days. 626 Magnetopause reconnection is likely to continue after onset and only at $(t-t_o) > 2$ days 627 does the mean value of Φ_D fall back to is overall mean value. Hence substorm onsets tend 628 to sit in intervals about 4.5 days long in which Φ_D is enhanced over the overall mean value. 629

It is interesting to note that integrating Φ_D over the interval between the appar-630 ent southward turning of the IMF (at $(t-t_o) = -35$ min, when mean values of Φ_D start 631 to rise sharply to the pre-onset peak) and $(t-t_o) = 10$ min, we find a total of 0.1 GWb 632 of open flux is generated. If we look at the total opened over the preconditioning inter-633 val -4 days $< (t-t_o) < -35$ min, it is 9.3 GWb. Much of this open flux will be lost and 634 Figure 8a shows that average -SML increases with the increasing Φ_D over this interval, 635 indicating enhanced open flux loss by enhanced nightside reconnection. However it is in-636 teresting how little open flux is, on average, generated in the growth phase and how much 637 the occurrence of a substorm onset relies on open flux accumulated during the precon-638 ditioning phase. The growth phase adds the final flux that triggers onset, but the role 639 of prior open flux and preconditioning appears to be very significant. 640

641

3.1 UT variations in the reconnection voltage Φ_D prior to onset

The black line in Figure 9 shows the variation of mean open flux generated in the 642 interval 150 min before onset to 10 min after, ΔF_{ap} , evaluated in bins of UT that are 643 1 hr wide. This is surrounded by a grey area that is plus and minus one standard error 644 in these means. Because the variations of average Φ_D with elapsed time $(t-t_o)$ are very 645 similar in form for all UTs (as in Figure 6), the results are insensitive to the interval of 646 elapsed times that is adopted. Indeed the same form is even seen if take the integral over 647 the whole preconditioning interval of 4 days before onset, as discussed above; however, 648 just as the total fluxes opened in that longer interval are roughly ten times larger than 649

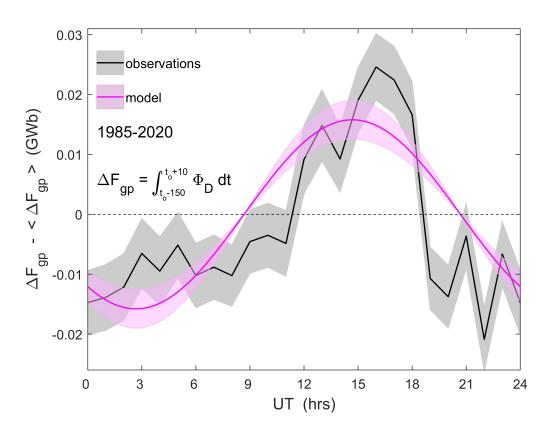


Figure 9. The variation of the open flux ΔF_{gp} generated in the substorm growth phase, taken to be the interval between 150 min before onset and 10 min after (using the nominal propagation lag of $\delta t_p = 19$ min from the nose of the bow shock), which is the integral of Φ_D over that interval. Values are shown as a function of UT for 1-hour intervals of UT and with the mean for all UT, $\langle \Delta F_{gp} \rangle$, subtracted. The black lines are mean values from the data, with the grey area showing plus and minus one standard error in the mean. The mauve line is the model prediction (see section 4) of text).

in the hour before onset (as discussed in the previous section), so the amplitude of the UT variation is also ten times larger.

This plot shows that there is a significant UT variation in the flux that is opened 652 ahead of substorm onsets. The mauve line (with an estimated error shown by the pink 653 area) is the predicted variation for pole motion effect. This uses a value of R_X of 0.15 654 in both hemispheres and was derived in Section 4 using the model used to predict the 655 onset occurrence (see Figure 4a) and described in Section 2.1. The uncertainty of $\pm 20\%$ 656 that is derived in Section 5 from the numerical model predictions shown in Figure 1. It 657 can be seen that this model prediction is not matching all the detail of the observed vari-658 ation, but both the phase and the amplitude of the main component is well reproduced. 659 Hence the UT variations in both the occurrence of onset and the integrated reconnec-660 tion voltage needed to trigger a substorm can be predicted by the model based on the 661 effect of pole motions. 662

$_{663}$ 4 Analysis of UT variation of flux added in substorm growth phase

Figure 10a gives the changes in the lobe fluxes (at X near zero) caused by the mo-664 tions of the poles, ΔF_{lobe} . This is the integral of the pole motion voltage ϕ with time. 665 The colours and symbols are as used in Figure 3. Figure 10b is the variation of the lobe 666 flux at $X = -21R_E$, $\Delta[F_{lobe}]_X$, obtained by multiplying the variations in Part a by R_X 667 = 0.15. The black line is the average of the two which will be half the UT variation of 668 the total lobe flux in the tail, $\Delta[F_{tail}]_X$. The model assumes that it is this total flux that 669 sets the probability of substorm onset occurring. To compensate for the UT variation 670 in $\Delta[F_{tail}]_X$ and give the same probability of onset requires a UT variation in the to-671 tal open flux produced by magnetopause reconnection which is given by the black line 672 in part c of Figure 10. This is the integral of the magnetopause reconnection voltage Φ_D 673 needed, which has been derived from the superposed epoch analysis of the data in Sec-674 tion 3.1. The uncertainty band shown by the grey area is for a $\pm 20\%$ variation in R_X 675 which is derived in the next Section 5. 676

The variation shown in Figure 10c is reproduced in Figure 9 as the mauve line with the uncertainty plotted in pink. It can be seen that the model is reproducing main phase and amplitude of the variation in prior reconnected flux with UT. The amplitude depends on value of R-X of 0.15 which agrees with the simple Monte-Carlo model of onset occurrence and which, in the next section, is found to be a reasonable value using the numerical simulations which gave Figure 1.

5 Numerical modelling the magnetotail response to dipole tilt

This section uses the results of a numerical, global, MHD model of the magnetosphere, shown in Figure 1, to gain some understanding of the factors R_{SX} and R_{NX} in Equation 8.

The simulations used are for tilt angles δ of 0, 34° and -34°. (Note that the use of 687 a geocentric dipole field means that the third simulation for $\delta = -34^{\circ}$ gave identical re-688 sults to $\delta = +34^{\circ}$ but with the north and south hemispheres reversed). All three simu-689 lations were started (at simulation time $t_s=0$) with a large open flux of $F_{PC}=0.85$ GWb 690 which decayed until near steady state was achieved shortly after $t_s=90$ min. The decay 691 was greater for $\delta = \pm 34^{\circ}$ than for $\delta = 0$ largely because the dayside reconnection voltage 692 Φ_D was persistently lower for $\delta = \pm 34^{\circ}$ and the night loss rate was high in both cases 693 because F_{PC} was high. At simulation time $t_s = 90$ min, F_{PC} was 0.583 GWb for $\delta = 0$ 694 and 0.509 GWb for $\delta = \pm 34^{\circ}$, a ratio of 1.145. At this time Φ_D was 90.8 kV for $\delta = 0$ and 695 78.3 kV for $\delta = \pm 34^{\circ}$. Hence the ratio of the reconnection voltages in the two cases was 696 1.160, similar to the ratio for F_{PC} . To allow for the different reconnection rate and make 697 comparisons, all open magnetic fluxes are adjusted so that the F_{PC} is the average of the 698

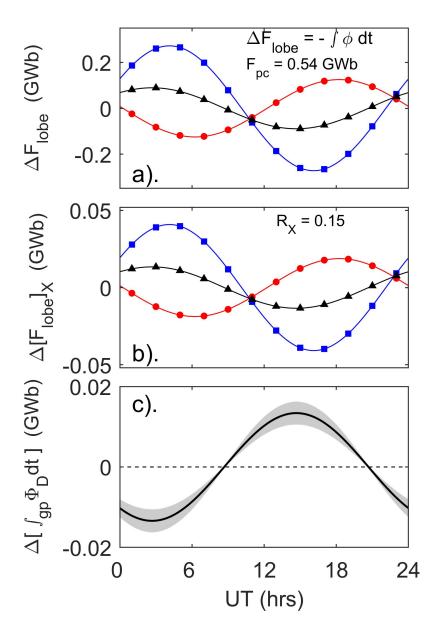


Figure 10. Variations giving the model prediction of the UT variation of flux opened during the growth phase, ΔF_{gp} shown in Figure 9. (a) the flux added to the lobes by the pole motions, ΔF_{lobe} , shown using the same colours and symbols as in Figure 3 (namely: red lines with red circle symbols are for the northern hemisphere polar cap, blue lines with blue square symbols are for the southern hemisphere polar cap and black lines with triangle symbols are for the global average of the two). This is the integral of ϕ with time for an average polar cap flux of F_{PC} of 0.54 GWb (giving a polar cap diameter d_{PC} of 3.73×10^6 m). (b) The variation in $[F_{lobe}]_X$, at the X coordinate of the tail reconnection site ($X = -21R_E$) in the numerical simulation shown in Figure 1. The value of R_X is 0.15, also used to make the model predictions in Figure 4. The variation in the integrated growth phase reconnection voltage needed to offset the variation in the average tail $[F_{lobe}]_X$, show by the black line in part (b). The uncertainty band is derived in Section 5.

 $\delta = 34^{\circ}$ and $\delta = 0$ cases (i.e., 0.546 GWb) which means multiplying the open flux for $\delta = 0$ by 0.937 and that for $\delta = \pm 34^{\circ}$ by 1.073. We also apply these factors to the two parts that add up to the total open flux (Equation 4), F_X and $[F_{lobe}]_X$. The analysis was repeated without these flux normalisation factors and the results for R_X were very similar because their effects on the fluxes F_X , ΔF_{PM} and F_{PC} are very similar. As well as using the mean of the open flux for $\delta = 0$ and $\delta = 34^{\circ}$, the value for each was employed and used to set an uncertainty on the R_X values derived.

The input solar wind parameters in the simulations were held constant and were 706 solar wind speed V_{SW} =400 kms⁻¹, solar wind number density N_{SW} =3×10⁶ m⁻³, mean 707 ion mass $m_{SW}=1.1$ amu, IMF flow-transverse component $B_t=5$ nT and an IMF clock 708 angle in GSM θ =180°. Note that the dayside reconnection voltages of 90.8 kV and 74.3 709 kV generated by the model are both larger than we would expect from these input so-710 lar wind parameters using the empirical relationship by Lockwood and McWilliams (2021a) 711 which gives 56.1 kV for Φ_D but are more similar to the total polar cap voltage Φ_{PC} from 712 the same study (which includes the effect of nightside reconnection and any viscous-like 713 voltage) of 69.6 kV. 714

Figure 1 gives an indication of how dipole tilt effects influence the magnetosphere 715 but it is not the whole story as it only shows the (XZ) plane at Y=0 and does not re-716 veal the behaviour closer to the dawn and dusk flanks. Figure 11 uses the same simu-717 lations to show how the total flux in the tail can be computed. It shows the magnetic 718 field B in cross sections of the tail (YZ planes at various X) in which the minima in B 719 clearly reveal the locations of the magnetopause currents and the cross tail current sep-720 arating the lobes. (Both are also clearly identified from the simulated currents). The mid-721 dle panel is for dipole tilt $\delta = 0$ and the two lobes are symmetrical and the cross-tail 722 current lies at Z=0 at all X and Y. 723

The left-hand panel shows that for dipole tilt angle $\delta = +34^{\circ}$ the cross tail cur-724 rent sheet is warped, such that its displacement to positive Z seen at Y=0 in parts a 725 and c of Figure 1 is a maximum but this displacement in Z is close to zero at the dawn 726 and dusk flank of the tail where it connects to the magnetopause currents. It can be seen 727 that for $\delta = +34^{\circ}$ the field in the southern lobe is considerably enhanced at all X com-728 pared to the $\delta = 0$ case, whereas in the northern hemisphere it is decreased. Because 729 this simulation is for an geocentric dipole field, the southern hemisphere for $\delta = +34^{\circ}$ 730 is identical to the northern hemisphere for $\delta = -34^{\circ}$ (Lockwood, Owens, Barnard, Watt, 731 et al., 2020). 732

In both cases, the field in the tail decreases with increasingly negative X. From the integral of the field threading the cross sections of the tail (the B_X component) we obtain the magnetic flux in each lobe at each x, $[F_{lobe}]_X$. At X below about $-20R_E$ there is no closed flux in the tail and so the decrease in this flux with increasingly negative X is only because of open flux F_X that threads the magnetopause sunward of the X in question.

From equation 4 we can compute the flux threading the magnetopause sunward of X, F_X and this is shown as a function of X in Figure 12a for the northern hemisphere for dipole tilt angles (positive for northern hemisphere tipped towards the Sun) of (red) $\delta = +34^\circ$, (green) $\delta = 0$ and (blue) $\delta = -34^\circ$. This plot shows that the magnitude of the effect on F_X of a tilt towards the Sun is somewhat smaller than a tilt of the same magnitude away from it. Hence the variation in the tail is not linear with δ .

From these variations we can compute the R_X factors. By integration of the definition of R_X with time, we have:

$$R_X = (dF_X/dt)/\phi = F_X/\int \phi dt = F_X/F_{PM} = \Delta F_X/\Delta F_{PM}$$
(9)

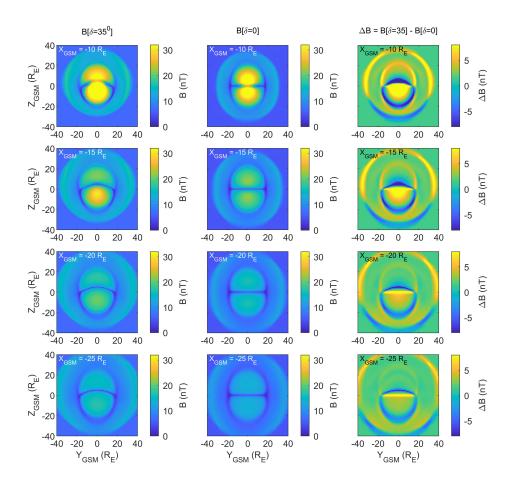


Figure 11. Cross-sections of the tail showing the field strength B in the GSM YZ plane from the simulations shown in Figure 1. From top to bottom the rows are for X of $-10R_E$, $-15R_E$, $-20R_E$, and $-25R_E$. The left-hand column is for dipole tilt angle $\delta = +34^\circ$, the middle column is for $\delta = 0$ and the right-hand column shows the difference between the two, ΔB .

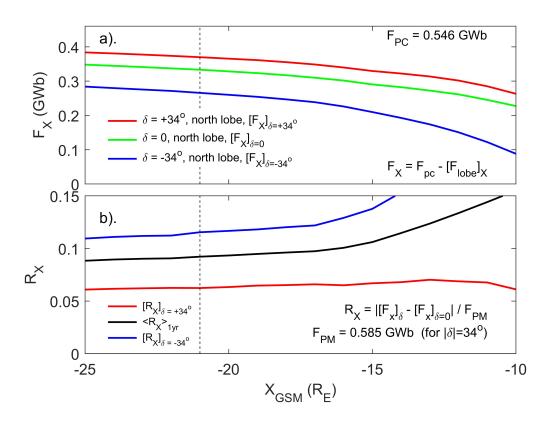


Figure 12. (a). Variation of the fluxes threading the dayside magnetopause F_X with X for a fixed polar cap flux F_{PC} of 0.546 GWb: red, green and blue are for dipole tilt angles (positive for northern hemisphere tipped towards the Sun) of $\delta = +34^{\circ}$, $\delta = 0$ and $\delta = -34^{\circ}$. The X of the tail reconnection site $(-21R_E)$ is shown by the vertical dashed line. (b) The values of R_X derived from Part a for (red) $\delta = +34^{\circ}$ and (blue) $\delta = -34^{\circ}$. The black line is the annual mean of the R_X values that are due to diurnal motions, $\langle R_X \rangle_{1yr}$, the derivation of which is explained in Figure 13.

where in this case we consider the deviation from the $\delta = 0$ case, $\Delta F_X = [F_X]_{\delta} - [F_X]_{\delta=0}$. 747 The corresponding flux ΔF_{PM} is given by $d_{PC}.B_i.\Delta X$ where ΔX is the difference in the 748 X coordinate of the diameter of the polar cap for tilt angles of δ and of $\delta = 0$. This yields 749 $|\Delta F_{PM}|$ of 0.585 GWb for the 34° change in δ . The red lines in Figure 12b gives the val-750 ues of R_X for tilting the polar cap sunward from $\delta = 0$ to $\delta = +34^{\circ}$ (or antisuward the 751 other way) and the blue line the value of R_X for tilting the polar cap sunward from δ 752 = -34° to $\delta = 0$ (or, again, antisuward the other way). The black line gives the average 753 over a whole year of R_X for the daily sunward/antisunward motion, $\langle R_X \rangle_{1ur}$. The deriva-754 tion of this from the simulation results is explained by Figure 13. 755

Figure 13 is for the example X of $-21R_E$. The points in Part a are the values of 756 the flux threading the dayside magnetopause F_X for $\delta = +34^\circ$, $\delta = 0$ and $\delta = -34^\circ$ 757 at this X, as given in Figure 12a. The line is a second order polynomial fit to these points. 758 This has been extended out to $\pm 39^{\circ}$, which is the full range of possible δ values that the 759 south pole can have. The vertical dashed lines mark the range of the annual variation 760 due to Earth's orbital motion ($\pm 23.44^{\circ}$). For each value of δ between the dashed lines, 761 the diurnal variation in δ is added and the diurnal change in F_X (ΔF_X) that it causes 762 is then scaled from the polynomial fit in Part a and the corresponding change in the pole 763 motion flux F_{PM} (ΔF_{PM}) (the integral of ϕ calculated from Equation 1): ΔF_X and ΔF_{PM} 764 are shown in parts b and c, respectively, as a function of the daily mean δ , and the ra-765 tio of the two, (equal to R_X by Equation 9) is shown in Part d. 766

A total of 365 values of R_X were computed for the daily average of δ of each day of the year and the mean taken to give the average value over a full year caused by the diurnal variation. The results show the means are the same for the two hemispheres and equal to 0.092. The analysis was re-run using the F_{PC} of the $\delta = +34^{\circ}$ simulation and then again using that for $\delta = 0$ (rather than the mean of the two which is used in Figures 12 and 13). This yield an uncertainty range in the R_X value of ± 0.013 .

The R_X value is of 0.092 is of the required order of magnitude but is smaller than 773 the 0.15 used and we need to look for potential missing factors of 1.6. There are a num-774 ber of considerations that can, individually or collectively, explain this factor. The val-775 ues of R_X depend on how much recently opened flux is present and so the time history 776 of Φ_D is important: larger fluxes of more-recent opened field lines give a higher F_X for 777 a given F_{PM} . The simulations are for near constant Φ_D whereas in substorm growth phases 778 Φ_D has increased with time, giving a higher fraction F_X/F_{PC} . However, from the time 779 variations of Φ_D shown in Figure 5, this factor gives, at most, a rise by a factor of only 780 about 1.05 in R_X . A bigger factor is the value of the open flux F_{PC} which is only 0.546 781 GWb in the simulations but Boakes et al. (2009) find is typically 0.75-0.9 at the time 782 of onset. The value of F_X is close to being proportional to F_{PC} and, for a circular po-783 lar cap, ϕ (and hence F_{PM}) is proportional to $F_{PC}^{0.5}$. Hence, by Equation 9, R_X is pro-784 portional to $F_{PC}^{0.5}$. This gives a factor of between 1.2-1.3. Another factor is the number 785 density of the solar wind, N_{SW} which controls the magnetosheath density at the day-786 side magnetopause, and hence the Alfvén speed with which newly-opened field lines move 787 over the dayside magnetopause away from the reconnection site. In the simulation, a low 788 value was used $(3 \times 10^6 \text{ m}^3)$ whereas the average value is roughly twice this. Increasing 789 N_{SW} by a factor of 2 would lower the Alfvén speed at the dayside magnetopause by a 790 factor of $2^{0.5} = 1.4$ and this would increase the F_X for a given F_{PC} and δ . This would 791 therefore also increase the R_X . Lastly, the value of $R_X = 0.092$ is derived from the sim-792 ulations for the reconnection X-line position in those simulations at the steady state achieved 793 at simulation time $t_s = 90$ min. As shown in Figure 1, this is at $X = -21R_E$. It is highly probable that the X-line at substorm onset forms closer to the Earth than this and Fig-795 ure 12 shows that the simulations give $R_X = 0.11$ at $X = -15R_E$ and $R_X = 0.12$ at X 796 $= -13R_{E}.$ 797

These considerations mean that the simulations can only be used as an order of magnitude guide but we can conclude that they give R_X values that are reasonably consis-

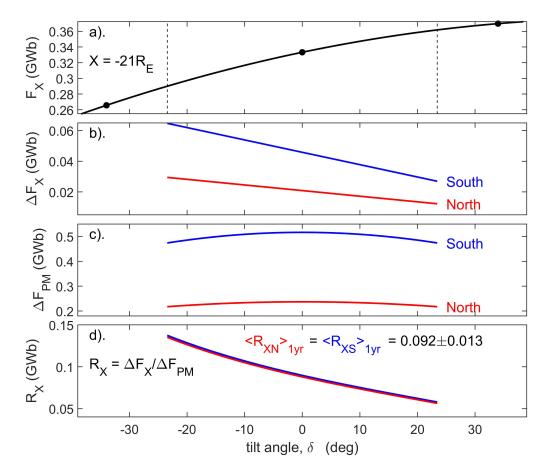


Figure 13. The derivation of the annual mean of the R_X values due to diurnal motions, $\langle R_X \rangle_{1yr}$ (the black line in Figure 12b) shown here for the example X of $-21R_E$. The points in part a are the values of the fluxes threading the dayside magnetopause F_X for δ = $+34^{\circ},$ $\delta = 0$ and $\delta = -34^{\circ}$, as given in Figure 12a and the line is a second order polynomial fit to these points. The plot covers the full potential range of δ (for the southern pole) and the vertical dashed lines mark the range of the annual variation due to Earth's orbital motion. For each value of δ in this range the maximum and minimum δ due to the diurnal variation is considered and the change that the diurnal motions cause in F_X , ΔF_X is scaled from the polynomial fit in part a and shown in b as a function of the daily mean of δ . The corresponding change in the pole motion flux caused by the diurnal motion in the polar cap (the integral of ϕ) is calculated from Equation 1 ΔF_{PM} , and shown in Part c. Part d gives $R_X = \Delta F_X / \Delta F_{PM}$. The mean value over a whole year for both hemispheres is 0.092. An uncertainty is derived using the open flux for each of the two runs, rather than the mean of the two. This yield an uncertainty in idered and the change that the diurnal motions cause in R_X of ± 0.013 .

tent with the empirically-derived value of 0.15, particularly if we take all the factors that are likely to increase the value of R_X into account.

⁸⁰² 6 Discussion and Conclusions

This paper has studied systematic *UT* variations in magnetospheric substorms, using a simple Monte-Carlo model, a global numerical MHD model and 1-minute observations taken over a 34-year interval. All reveal an effect consistent with the effect of diurnal motions of the magnetic poles in a geocentric-solar frame of reference caused by Earth's rotation and the eccentric dipole nature of the intrinsic geomagnetic field.

The analysis has focused on the effect of dipole tilt on the tail flux as an explana-808 tion of UT effects but we should also remember that the num, erical simulations give a 809 dayside reconnection voltage Φ_D that is 16% higher (92kV) for $\delta=0$ than for $\delta=\pm 34^{\circ}$ 810 (78 kV). As discussed in Section 1.6 such a variation in Φ_D with δ has been invoked as 811 the origin of the equinoctial pattern and we need to be clear what this means for aver-812 age variations with UT. By Maxwell's equation $\nabla \vec{B} = 0$, Φ_D must be the same for both 813 hemispheres (as must Φ_N) but note that transpolar voltages Φ_{PC} can differ in the two 814 polar caps because of induction effects associated with field changes in the magnetosphere. 815 for simplicity of explanation, we here consider a geocentric dipole (epoch 2003) and the 816 fact that Φ_D must be the same for the two hemispheres means that the variation of Φ_D 817 with δ must be symmetrical about zero, such that the value for a given tilt δ is the same 818 as that for $-\delta$. The left hand column in Figure 14 shows four model variations of Φ_D 819 with δ that meet this condition. In row (A) there is a minimum in Φ_D at $\delta=0$. The right 820 hand panel shows the F-UT pattern of Φ_D (F being the fraction of a calendar year) that 821 this generates. Averaging over all 365 days of a year at a given UT yields the means $\langle \Phi_D \rangle_F$ 822 shown as a function of UT in the middle panel the middle panel. The F-UT pattern is 823 an "inverse equinoctial" pattern: inverse because the contours of low $|\delta|$ give minima. 824 The variation with UT shows a semi-diurnal form with minima near 11 and 23 UT. 825

Row (**B**) shows the case for a maximum in Φ_D at $\delta=0$. This is the case that was revealed by the numerical simulations discussed in Section 5 and, indeed, the variation has been scaled to the values obtained in that section for $|\delta|=0$ and $|\delta|=\pm 34^{\circ}$. This does give the equinoctial pattern, with low $|\delta|$ giving maxima, as seen for geomagnetic activity. The UT variation again has a semi-diurnal form, but this time it is maxima at 11 hrs UT and 23 hrs UT.

Row (C) shows what happens when the peak Φ_D is at an intermediate δ (here $\pm 17.5^{\circ}$). The *F*-*UT* pattern is like an equinoctial form but is more complex, having a deep minimum embedded within the bands of the maximum Φ_D . The *UT* variation is, however, the same in form as for (**B**).

Row (**D**) shows the results for the variation of Φ_D with δ from the simulation results of Eggington et al. (2020). Thee have been scaled up to the same range as the other variations in the Figure. At first sight we would expect the results to be similar to those in row (**C**) for peak Φ_D at intermediate δ and indeed, the *F*-*UT* plot has similarities but the features are much narrower and sharper. This has a major effect when we average over all *F* and no consistent variation of $\langle \Phi_D \rangle_F$ with *UT* is seen.

Figure 14 shows that variations of Φ_D with δ can give an equinoctial pattern but the diurnal variation seen when data for a given UT are averaged over all F gives two peaks a day. These are at 10.8 hrs UT and 22.8 hrs UT for a geocentric dipole and at 9.0 hrs UT and 21.0 hrs UT for an eccentric dipole (times for 2003). Figure 9 shows the dominant variation is diurnal and not semidiurnal which eliminates variations in the magnetopause reconnection rate as the cause. That being said, the deviations from a pure sinusoidal form in Figure 9 might well be explained by a semi-diurnal oscillation in Φ_D ,

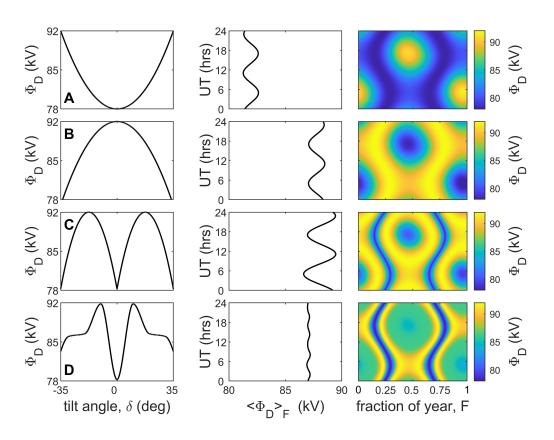


Figure 14. Analysis of the effects of various variations of the magnetopause reconnection voltage, Φ_D , with the tilt angle δ . The left-hand column gives the variation of Φ_D with δ . The right-have column gives the resulting *F*-*UT* pattern of Φ_D (where *F* is the fraction of a calendar year). The middle column gives Φ_D averaged over a year (x-axis) as a function of *UT* (y-axis). The input variations are all scaled between a maximum of 92 kV and a minimum of 78 kV to match the results of the numerical MHD simulations shown in Figures 1, 11 and 12 and a geocentric dipole is used for simplicity. the top row (**A**) is for a minimum Φ_D at δ =0; row (**B**) is for a maximum at δ =0 (the variation consistent with the numerical simulation results) row (**C**) is for a maximum at δ =17.5° and row (**D**) is the variation from the numerical simulations by Eggington et al. (2020) (scaled to the same minimum-to-maximum range as the other panels).

but that would be a considerably smaller amplitude modulation than the dominant diurnal one shown.

Another reason why we can discount the effects of modulation of Φ_D by δ for the 851 effects studied here comes from the superposed epoch plots shown on Figure 8. If the 852 difference between the variations at a given UT were due to semi-diurnal variations in 853 Φ_D , we would expect the superposed epoch variations to show oscillations with a 1-day 854 period. These are not seen. We do note, however, that tilt angle effects on Φ_D can give 855 the equinoctial pattern. That having been said, the same is true of potential tilt angle 856 857 effects of the night reconnection voltage Φ_N , be it through enhanced instability in the tail to substorm onset, i.e. through lowering the tail flux threshold needed for on-858 set to occur - as proposed by Kivelson and Hughes (1990), or through the effect of dipole 859 tilt on the tail field, as modelled by Lockwood, Owens, Barnard, Watt, et al. (2020). 860

On the other hand, the paper has shown that the UT variations are consistent with the diurnal pole motions of an eccentric dipole. Using a simple Monte-Carlo model based on the idea that the probability of onset is raised by the total magnetic flux in both lobes in the near-Earth tail, we can model the observed UT variation in the number of onsets (Figure 4) except the model as yet has no way of including recurrent substorms due to persistent southward IMF and instead re-starts each growth phase at a random time.

This idea (of the probability of substorm onset being raised by the tail lobe field 867 which is modulated by the dipole tilt) is supported by the superposed epoch studies. These 868 clearly show larger magnetopause reconnection voltages are required for onsets at some 869 $UT_{\rm s}$ than at others. Figure 8 shows that the average behaviour is that after a substorm 870 onset the reconnection voltage has fallen back to it average value in about 2 days. How-871 ever, before onset a considerably longer period of enhanced opening of magnetospheric 872 flux is required. The plots (Figures 5 and 8) reveal a rise in Φ_D , on average, of order 30 873 min ahead on an onset. this is consistent with the southward turning that traditionally 874 starts substorm growth phases. However there seems to be two levels of precondition-875 ing before this. The first is an average rise in Φ_D in the 100 min prior to the southward 876 turning. The second is a preconditioning from overall average levels that increases over 877 the prior 6 days. Analysis of solar cycles shows, somewhat surprisingly, substorm onsets 878 are more common at sunspot minimum and hence this cannot be attributed to the vari-879 ation of average solar wind conditions with the sunspot cycle. 880

A theory that allows us to accommodate the effect of pole motions and an eccen-881 tric dipole into magnetospheric dynamics has been presented. In relation to substorm 882 growth phase termination and onsets, the majotr unknown is the extent to which dipole 883 tilts influence the tail and X coordinates that influence onset. This has been allowed for 884 in the present paper with the factor R_X . The Monte-Carlo model of onsets requires $R_X \approx 0.15$, 885 a value that is shown here to agree well with the UT variation found from the super-886 posed epoch studies. A test of this value using a numerical MHD model of the magne-887 to sphere is shown to result in a value near 0.10. However, there are a number of factors 888 that could be invoked to increase this number and make it consistent with the 0.15 value. 889 The present paper does no more than establish that the numerical model simulations show 890 an effect that gives the required diurnal variation with the correct phase, but the am-891 plitude is smaller than needed to fit the observations by a factor of about a third. Fur-892 ther work is needed to establish if indeed $R_X=0.15$ is the correct value. 893

894 **References**

 Alexeev, I. I., Belenkaya, E. S., Kalegaev, V. V., Feldstein, Y. I., & Grafe, A. (1996).
 Magnetic storms and magnetotail currents. Journal of Geophysical Research: Space Physics, 101 (A4), 7737–7747. Retrieved 2022-12-12, from http://doi
 .wiley.com/10.1029/95JA03509 doi: 10.1029/95JA03509

Bartels, J. (1936). The eccentric dipole approximating the Earth's magnetic field. Journal of Geophysical Research, 41(3), 225-250. Retrieved 2023-01-20, from http://doi.wiley.com/10.1029/TE041i003p00225 doi: 10.1029/TE041i003p00225

- Berthelier, A. (1976). Influence of the polarity of the interplanetary magnetic field
 on the annual and the diurnal variations of magnetic activity. Journal of Geophysical Research, 81(25), 4546-4552. Retrieved 2022-12-09, from http://doi
 .wiley.com/10.1029/JA081i025p04546 doi: 10.1029/JA081i025p04546
- Boakes, P. D., Milan, S. E., Abel, G. A., Freeman, M. P., Chisham, G., & Hubert,
 B. (2009). A statistical study of the open magnetic flux content of the magnetosphere at the time of substorm onset. *Geophysical Research Letters*,
 36(4), L04105. Retrieved 2022-10-23, from http://doi.wiley.com/10.1029/
 2008GL037059 doi: 10.1029/2008GL037059
- Boyle, C. B., Reiff, P. H., & Hairston, M. R. (1997). Empirical polar cap potentials. Journal of Geophysical Research: Space Physics, 102(A1), 111–125. Retrieved 2022-12-19, from http://doi.wiley.com/10.1029/96JA01742 doi: 10.1029/ 915 96JA01742
- Brekke, A., & Moen, J. (1993). Observations of high latitude ionospheric conductances. Journal of Atmospheric and Terrestrial Physics, 55 (11-12), 1493-1512.
 Retrieved 2022-12-09, from https://linkinghub.elsevier.com/retrieve/
 pii/002191699390126J doi: 10.1016/0021-9169(93)90126-J
- 920Carter, J. A., Milan, S. E., Paxton, L. J., Anderson, B. J., & Gjerloev, J. (2020).921Height-integrated ionospheric conductances parameterized by interplanetary922magnetic field and substorm phase. Journal of Geophysical Research: Space923Physics, 125(10). Retrieved 2022-11-10, from https://onlinelibrary.wiley924.com/doi/10.1029/2020JA028121
- Cliver, E. W., Kamide, Y., & Ling, A. G. (2000). Mountains versus valleys: Semiannual variation of geomagnetic activity. Journal of Geophysical Research: Space Physics, 105(A2), 2413-2424. Retrieved 2022-11-27, from http://doi.wiley
 .com/10.1029/1999JA900439 doi: 10.1029/1999JA900439
- Cnossen, I., Wiltberger, M., & Ouellette, J. E. (2012). The effects of seasonal and diurnal variations in the Earth's magnetic dipole orientation on solar
 wind-magnetosphere-ionosphere coupling. Journal of Geophysical Research: Space Physics, 117(A11), n/a-n/a. Retrieved 2022-12-19, from http:// doi.wiley.com/10.1029/2012JA017825 doi: 10.1029/2012JA017825
- Cowley, S. W. H., & Lockwood, M. (1992). Excitation and decay of solar winddriven flows in the magnetosphere-ionosphere system. Annales Geophysicae, 10, 103-115. Retrieved 2022-08-18, from https://ui.adsabs.harvard.edu/ abs/1992AnGeo..10..103C (ADS Bibcode: 1992AnGeo..10..103C)
- Coxon, J. C., Milan, S. E., & Anderson, B. J. (2018, March). A review of Birkeland current research using AMPERE. In A. Keiling, O. Marghitu, & M. Wheatland (Eds.), *Geophysical Monograph Series* (pp. 257–278). Hoboken, NJ, USA: John Wiley & Sons, Inc. Retrieved 2023-04-08, from https://onlinelibrary
 .wiley.com/doi/10.1002/9781119324522.ch16 doi: 10.1002/9781119324522
 .ch16
- Crooker, N. U., & Siscoe, G. L. (1986). On the limits of energy transfer through
 dayside merging. Journal of Geophysical Research, 91 (A12), 13393. Retrieved
 2022-12-12, from http://doi.wiley.com/10.1029/JA091iA12p13393 doi: 10
 .1029/JA091iA12p13393
- Danilov, A. A., Krymskii, G. F., & Makarov, G. A. (2013). Geomagnetic

949 950	activity as a reflection of processes in the magnetospheric tail: 1. The source of diurnal and semiannual variations in geomagnetic activity. Ge-
951	omagnetism and Aeronomy, 53(4), 441–447. Retrieved 2022-11-27,
952	from http://link.springer.com/10.1134/S0016793213040051 doi:
953	10.1134/S0016793213040051
954	de La Sayette, P., & Berthelier, A. (1996). The am annual-diurnal variations 1959-
955	1988: A 30-year evaluation. Journal of Geophysical Research: Space Physics,
956	101(A5), 10653-10663. Retrieved 2022-12-09, from http://doi.wiley.com/10
957	.1029/96JA00165 doi: 10.1029/96JA00165
958	Eggington, J. W. B., Eastwood, J. P., Mejnertsen, L., Desai, R. T., & Chittenden,
959	J. P. (2020). Dipole tilt effect on magnetopause reconnection and the steady-
960	state magnetosphere-ionosphere system: Global MHD simulations. Journal
961	of Geophysical Research: Space Physics, 125(7). Retrieved 2022-12-11, from
962	https://onlinelibrary.wiley.com/doi/10.1029/2019JA027510 doi:
963	10.1029/2019JA027510
964	Finch, I. D., Lockwood, M. L., & Rouillard, A. P. (2008). Effects of solar wind mag-
965	netosphere coupling recorded at different geomagnetic latitudes: Separation
966	of directly-driven and storage/release systems. Geophysical Research Letters,
967	35(21), L21105. Retrieved 2022-08-18, from http://doi.wiley.com/10.1029/
968	2008GL035399 doi: 10.1029/2008GL035399
969	Forsyth, C., Rae, I. J., Coxon, J. C., Freeman, M. P., Jackman, C. M., Gjerloev,
970	J., & Fazakerley, A. N. (2015). A new technique for determining Substorm Onsets and Phases from Indices of the Electrojet (SOPHIE). Journal of
971	Onsets and Phases from Indices of the Electrojet (SOPHIE). Journal of Geophysical Research: Space Physics, 120(12), 10,592–10,606. Retrieved
972	2022-12-13, from http://doi.wiley.com/10.1002/2015JA021343 doi:
973 974	10.1002/2015JA021343
	Förster, M., & Cnossen, I. (2013). Upper atmosphere differences between north-
975 976	ern and southern high latitudes: The role of magnetic field asymmetry. <i>Journal</i>
977	of Geophysical Research: Space Physics, 118(9), 5951–5966. Retrieved 2022-
978	12-19, from http://doi.wiley.com/10.1002/jgra.50554 doi: 10.1002/jgra
979	.50554
980	Hairston, M. R., & Heelis, R. A. (1993). High-latitude electric field studies using
981	DMSP data. University of Texas at Dallas, Richardson Center for Space Sci-
982	ences Report. Retrieved 2022-12-19, from https://apps.dtic.mil/sti/pdfs/
983	ADA265032.pdf
984	Hoilijoki, S., Souza, V. M., Walsh, B. M., Janhunen, P., & Palmroth, M. (2014).
985	Magnetopause reconnection and energy conversion as influenced by the dipole
986	tilt and the IMF B_x . Journal of Geophysical Research: Space Physics,
987	119(6), 4484-4494. Retrieved 2022-12-11, from http://doi.wiley.com/
988	10.1002/2013JA019693 doi: 10.1002/2013JA019693
989	Kabin, K., Rankin, R., Rostoker, G., Marchand, R., Rae, I. J., Ridley, A. J., L.,
990	D. D. (2004). Open-closed field line boundary position: A parametric study
991	using an MHD model. Journal of Geophysical Research, 109(A5), A05222.
992	Retrieved 2022-10-27, from http://doi.wiley.com/10.1029/2003JA010168
993	doi: 10.1029/2003JA010168
994	Kitamura, N., Hasegawa, H., Saito, Y., Shinohara, I., Yokota, S., Nagai, T.,
995	Burch, J. L. (2016). Shift of the magnetopause reconnection line to the minter hereignberg under control IME conditions. Costail and MMS ab
996	winter hemisphere under southward IMF conditions: Geotail and MMS ob-
997	servations. <i>Geophysical Research Letters</i> , 43(11), 5581–5588. Retrieved 2022-12-12, from http://doi.wiley.com/10.1002/2016GL069095 doi:
998	10.1002/2016GL069095
999	Kivelson, M. G., & Hughes, W. J. (1990). On the threshold for triggering substorms.
1000 1001	Planetary and Space Science, 38(2), 211–220. Retrieved 2022-11-27, from
1001	https://linkinghub.elsevier.com/retrieve/pii/0032063390900855 doi:
1003	10.1016/0032-0633(90)90085-5

Koochak, Z., & Fraser-Smith, A. C. (2017a).An update on the centered and 1004 eccentric geomagnetic dipoles and their poles for the years 1980–2015. 1005 Earth and Space Science, 4(10), 626–636. Retrieved 2022-10-27, from 1006 https://onlinelibrary.wiley.com/doi/10.1002/2017EA000280 doi: 1007 10.1002/2017EA000280 1008 Koochak, Z., & Fraser-Smith, A. C. (2017b). An update on the centered and 1009 eccentric geomagnetic dipoles and their poles for the years 1980–2015. 1010 Earth and Space Science, 4(10), 626–636. Retrieved 2022-10-27, from 1011 https://onlinelibrary.wiley.com/doi/10.1002/2017EA000280 doi: 1012 10.1002/2017EA000280 1013 Korovinskiy, D. B., Semenov, V. S., Erkaev, N. V., Ivanov, I. B., & Kiehas, 1014 S. A. Current sheet bending as destabilizing factor in magne-(2018).1015 totail dynamics. *Physics of Plasmas*, 25(9), 092901. Retrieved 2022-1016 12-11, from http://aip.scitation.org/doi/10.1063/1.5046175 doi: 1017 10.1063/1.5046175 1018 Kubota, Y., Nagatsuma, T., Den, M., Tanaka, T., & Fujita, S. (2017). Polar cap po-1019 tential saturation during the Bastille Day storm event using global MHD sim-1020 Journal of Geophysical Research: Space Physics, 122(4), 4398–4409. ulation. 1021 Retrieved 2022-12-09, from http://doi.wiley.com/10.1002/2016JA023851 1022 doi: 10.1002/2016JA023851 1023 Kubyshkina, M., Semenov, V., Erkaev, N., Gordeev, E., & Kubyshkin, I. (2022).1024 The asymmetry of magnetospheric configuration and substorms occurrence 1025 rate within a solar activity cycle. In A. Kosterov, N. Bobrov, E. Gordeev, 1026 E. Kulakov, E. Lyskova, & I. Mironova (Eds.), Problems of Geocosmos-2020 1027 (pp. 451–464). Cham: Springer International Publishing. Retrieved 2022-12-11, 1028 from https://link.springer.com/10.1007/978-3-030-91467-7_33 (Se-1029 ries Title: Springer Proceedings in Earth and Environmental Sciences) doi: 1030 10.1007/978-3-030-91467-7_33 1031 Kubyshkina, M., Tsyganenko, N., Semenov, V., Kubyshkina, D., Partamies, N., & 1032 Gordeev, E. (2015). Further evidence for the role of magnetotail current shape 1033 in substorm initiation. Earth, Planets and Space, 67(1), 139. Retrieved 2022-1034 12-11, from http://www.earth-planets-space.com/content/67/1/139 doi: 1035 10.1186/s40623-015-0304-1 1036 Laundal, K. M., Cnossen, I., Milan, S. E., Haaland, S. E., Coxon, J., Pedatella, 1037 N. M., ... Reistad, J. P. (2017). North–south asymmetries in Earth's mag-1038 netic field: Effects on high-latitude geospace. Space Science Reviews, 206(1-4), 1039 Retrieved 2022-12-19, from http://link.springer.com/10.1007/ 225 - 257.1040 s11214-016-0273-0 doi: 10.1007/s11214-016-0273-0 1041 Li, H., Wang, C., & Peng, Z. (2013).Solar wind impacts on growth phase dura-1042 tion and substorm intensity: A statistical approach. Journal of Geophysical 1043 Research: Space Physics, 118(7), 4270–4278. Retrieved 2022-12-21, from 1044 http://doi.wiley.com/10.1002/jgra.50399 doi: 10.1002/jgra.50399 1045 Lockwood, M. (1993).Modelling high-latitude ionosphere for time-varying 1046 plasma convection. IEE Proceedings H Microwaves, Antennas and Propa-1047 qation, 140(2), 91.Retrieved 2022-08-18, from https://digital-library 1048 .theiet.org/content/journals/10.1049/ip-h-2.1993.0015 doi 1049 10.1049/ip-h-2.1993.0015 1050 Lockwood, M., Chambodut, A., Finch, I. D., Barnard, L. A., Owens, M. J., & 1051 Haines, C. (2019).Time-of-day/time-of-year response functions of plane-1052 tary geomagnetic indices. Journal of Space Weather and Space Climate, 9, 1053 Retrieved 2022-08-18, from https://www.swsc-journal.org/10.1051/ A20. 1054 swsc/2019017 doi: 10.1051/swsc/2019017 1055 Lockwood, M., Cowley, S., Todd, H., Willis, D., & Clauer, C. (1988).Ion 1056 flows and heating at a contracting polar-cap boundary. Planetary and 1057 Retrieved 2022-08-18, from https:// Space Science, 36(11), 1229-1253. 1058

1059 1060	linkinghub.elsevier.com/retrieve/pii/0032063388900761 doi: 10.1016/0032-0633(88)90076-1
1061	Lockwood, M., & Cowley, S. W. H. (2022). Magnetosphere-Ionosphere Cou-
1062	pling: Implications of Non-Equilibrium Conditions. Frontiers in Astron-
1063	omy and Space Sciences, 9, 908571. Retrieved 2022-08-18, from https://
1064	www.frontiersin.org/articles/10.3389/fspas.2022.908571/full doi:
1065	10.3389/fspas.2022.908571
1066	Lockwood, M., Haines, C., Barnard, L. A., Owens, M. J., Scott, C. J., Cham-
1067	bodut, A., & McWilliams, K. A. (2021). Semi-annual, annual and Uni-
1068	versal Time variations in the magnetosphere and in geomagnetic activ-
1069	ity: 4. Polar cap motions and origins of the Universal Time effect. Jour-
1070	nal of Space Weather and Space Climate, 11, 15. Retrieved 2022-08-18,
1071	from https://www.swsc-journal.org/10.1051/swsc/2020077 doi:
1072	10.1051/swsc/2020077
1073	Lockwood, M., & McWilliams, K. A. (2021a). On optimum solar wind-
1074	magnetosphere coupling functions for transpolar voltage and planetary
1075	geomagnetic activity. Journal of Geophysical Research: Space Physics,
1076	126(12). Retrieved 2022-05-28, from https://onlinelibrary.wiley.com/
1077	doi/10.1029/2021JA029946 doi: 10.1029/2021JA029946
1078	Lockwood, M., & McWilliams, K. A. (2021b). A survey of 25 years' transpolar volt-
1079	age data from the SuperDARN radar network and the expanding-contracting
1080	polar cap model. Journal of Geophysical Research: Space Physics, 126(9). Re-
1081	trieved 2022-08-18, from https://onlinelibrary.wiley.com/doi/10.1029/
1082	2021JA029554 doi: 10.1029/2021JA029554
1083	Lockwood, M., McWilliams, K. A., Owens, M. J., Barnard, L. A., Watt, C. E.,
1084	Scott, C. J., Coxon, J. C. (2020). Semi-annual, annual and Universal Time
1085	variations in the magnetosphere and in geomagnetic activity: 2. Response to solar wind power input and relationships with solar wind dynamic pressure
1086 1087	and magnetospheric flux transport. Journal of Space Weather and Space Cli-
1088	mate, 10, 30. Retrieved 2022-08-18, from https://www.swsc-journal.org/
1089	10.1051/swsc/2020033 doi: 10.1051/swsc/2020033
1090	Lockwood, M., & Milan, S. (2023). Universal time variations in the magneto-
1091	sphere. Frontiers in Astronomy and Space Sciences, 10(9), 1139295. Re-
1092	trieved 2023-02-16, from https://www.frontiersin.org/articles/10.3389/
1093	fspas.2023.1139295/full doi: 10.3389/fspas.2023.1139295
1094	Lockwood, M., Owens, M., & Barnard, L. (2023). Universal Time variations in the
1095	magnetosphere and the effect of CME arrival time: Analysis of the February
1096	2022 event that led to the loss of Starlink satellites. J. Geophys. Res. Space
1097	Science, submitted. Retrieved 2023-01-05, from https://doi.org/10.1002/
1098	essoar.10512909.1 doi: 10.1002/essoar.10512909.1
1099	Lockwood, M., Owens, M. J., Barnard, L. A., Haines, C., Scott, C. J., McWilliams,
1100	K. A., & Coxon, J. C. (2020). Semi-annual, annual and Universal Time vari-
1101	ations in the magnetosphere and in geomagnetic activity: 1. Geomagnetic
1102	data. Journal of Space Weather and Space Climate, 10, 23. Retrieved 2022-
1103	08-18, from https://www.swsc-journal.org/10.1051/swsc/2020023 doi:
1104	10.1051/swsc/2020023
1105	Lockwood, M., Owens, M. J., Barnard, L. A., Watt, C. E., Scott, C. J., Coxon,
1106	J. C., & McWilliams, K. A. (2020). Semi-annual, annual and Universal Time
1107	variations in the magnetosphere and in geomagnetic activity: 3. Modelling.
1108	Journal of Space Weather and Space Climate, 10, 61. Retrieved 2022-08-
1109	18, from https://www.swsc-journal.org/10.1051/swsc/2020062 doi: 10.1051/swsc/2020062
1110	Lyatsky, W., Newell, P. T., & Hamza, A. (2001). Solar illumination as cause of
1111	the equinoctial preference for geomagnetic activity. <i>Geophysical Research Let-</i>
1112 1113	the equinoctial preference for geomagnetic activity. Geophysical Research Let- ters, 28(12), 2353–2356. Retrieved 2022-11-27, from http://doi.wiley.com/
1113	(12), 2000 2000. Removed 2022 II 21, non http://doi.witey.com/

1114	10.1029/2000GL012803 doi: 10.1029/2000GL012803
1115	Lyons, L. R., Zou, Y., Nishimura, Y., Gallardo-Lacourt, B., Angelopulos, V., &
1116	Donovan, E. F. (2018). Stormtime substorm onsets: occurrence and flow chan-
1117	nel triggering. Earth, Planets and Space, 70(1), 81. Retrieved 2022-12-19, from
1118	https://earth-planets-space.springeropen.com/articles/10.1186/
1119	s40623-018-0857-x doi: 10.1186/s40623-018-0857-x
1120	Mayaud, PN. (1972). The aa indices: A 100-year series characterizing the magnetic
1121	activity. J. Geophys. Res., 77(34), 6870-6874. Retrieved from https://doi
1122	.org/10.1029/ja077i034p06870 doi: 10.1029/ja077i034p06870
1123	McIntosh, D. (1959). On the annual variation of magnetic disturbance. Philo-
1124	sophical Transactions of the Royal Society of London. Series A, Mathemati-
1125	cal and Physical Sciences, 251(1001), 525–552. Retrieved 2022-12-09, from
1126	https://royalsocietypublishing.org/doi/10.1098/rsta.1959.0010 doi:
1127	10.1098/rsta.1959.0010
1128	Menvielle, M., & Berthelier, A. (1991). The K-derived planetary indices: Descrip-
1129	tion and availability. <i>Reviews of Geophysics</i> , 29(3), 415. Retrieved 2022-12-12,
1120	from http://doi.wiley.com/10.1029/91RG00994 doi: 10.1029/91RG00994
1131	Milan, S. E., Boakes, P. D., & Hubert, B. (2008). Response of the expand-
1131	ing/contracting polar cap to weak and strong solar wind driving: Implications
1132	for substorm onset. Journal of Geophysical Research: Space Physics, 113(A9),
1133	n/a-n/a. Retrieved 2022-10-23, from http://doi.wiley.com/10.1029/
1135	2008JA013340 doi: 10.1029/2008JA013340
1136	Milan, S. E., Carter, J. A., Sangha, H., Bower, G. E., & Anderson, B. J. (2021).
1130	Magnetospheric flux throughput in the Dungey cycle: Identification of con-
1138	vection state during 2010. Journal of Geophysical Research: Space Physics,
1139	126(2), e2020JA028437. Retrieved from https://agupubs.onlinelibrary
1140	.wiley.com/doi/abs/10.1029/2020JA028437 doi: https://doi.org/10.1029/
1141	2020JA028437
1141	2020JA028437 Milan, S. E., Walach, M., Carter, J. A., Sangha, H., & Anderson, B. J. (2019).
1142	Milan, S. E., Walach, M., Carter, J. A., Sangha, H., & Anderson, B. J. (2019).
1142 1143	Milan, S. E., Walach, M., Carter, J. A., Sangha, H., & Anderson, B. J. (2019). Substorm onset latitude and the steadiness of magnetospheric convection.
1142	 Milan, S. E., Walach, M., Carter, J. A., Sangha, H., & Anderson, B. J. (2019). Substorm onset latitude and the steadiness of magnetospheric convection. Journal of Geophysical Research: Space Physics, 124(3), 1738–1752. Retrieved
1142 1143 1144	 Milan, S. E., Walach, M., Carter, J. A., Sangha, H., & Anderson, B. J. (2019). Substorm onset latitude and the steadiness of magnetospheric convection. Journal of Geophysical Research: Space Physics, 124(3), 1738–1752. Retrieved 2022-12-19, from https://onlinelibrary.wiley.com/doi/abs/10.1029/
1142 1143 1144 1145	 Milan, S. E., Walach, M., Carter, J. A., Sangha, H., & Anderson, B. J. (2019). Substorm onset latitude and the steadiness of magnetospheric convection. <i>Journal of Geophysical Research: Space Physics</i>, 124(3), 1738–1752. Retrieved 2022-12-19, from https://onlinelibrary.wiley.com/doi/abs/10.1029/ 2018JA025969 doi: 10.1029/2018JA025969
1142 1143 1144 1145 1146	 Milan, S. E., Walach, M., Carter, J. A., Sangha, H., & Anderson, B. J. (2019). Substorm onset latitude and the steadiness of magnetospheric convection. Journal of Geophysical Research: Space Physics, 124 (3), 1738–1752. Retrieved 2022-12-19, from https://onlinelibrary.wiley.com/doi/abs/10.1029/ 2018JA025969 doi: 10.1029/2018JA025969 Mishin, V., & Karavaev, Y. (2017). Saturation of the magnetosphere dur-
1142 1143 1144 1145 1146 1147	 Milan, S. E., Walach, M., Carter, J. A., Sangha, H., & Anderson, B. J. (2019). Substorm onset latitude and the steadiness of magnetospheric convection. Journal of Geophysical Research: Space Physics, 124 (3), 1738–1752. Retrieved 2022-12-19, from https://onlinelibrary.wiley.com/doi/abs/10.1029/ 2018JA025969 doi: 10.1029/2018JA025969 Mishin, V., & Karavaev, Y. (2017). Saturation of the magnetosphere dur- ing superstorms: New results from the magnetogram inversion technique.
1142 1143 1144 1145 1146 1147 1148	 Milan, S. E., Walach, M., Carter, J. A., Sangha, H., & Anderson, B. J. (2019). Substorm onset latitude and the steadiness of magnetospheric convection. Journal of Geophysical Research: Space Physics, 124 (3), 1738–1752. Retrieved 2022-12-19, from https://onlinelibrary.wiley.com/doi/abs/10.1029/ 2018JA025969 doi: 10.1029/2018JA025969 Mishin, V., & Karavaev, Y. (2017). Saturation of the magnetosphere dur-
1142 1143 1144 1145 1146 1147 1148 1149	 Milan, S. E., Walach, M., Carter, J. A., Sangha, H., & Anderson, B. J. (2019). Substorm onset latitude and the steadiness of magnetospheric convection. Journal of Geophysical Research: Space Physics, 124(3), 1738–1752. Retrieved 2022-12-19, from https://onlinelibrary.wiley.com/doi/abs/10.1029/ 2018JA025969 doi: 10.1029/2018JA025969 Mishin, V., & Karavaev, Y. (2017). Saturation of the magnetosphere dur- ing superstorms: New results from the magnetogram inversion technique. Solar-Terrestrial Physics, 3(3), 28–36. Retrieved 2022-10-28, from http:// naukaru.ru/en/nauka/article/18490/view doi: 10.12737/stp-33201704
1142 1143 1144 1145 1146 1147 1148 1149 1150	 Milan, S. E., Walach, M., Carter, J. A., Sangha, H., & Anderson, B. J. (2019). Substorm onset latitude and the steadiness of magnetospheric convection. Journal of Geophysical Research: Space Physics, 124(3), 1738–1752. Retrieved 2022-12-19, from https://onlinelibrary.wiley.com/doi/abs/10.1029/ 2018JA025969 doi: 10.1029/2018JA025969 Mishin, V., & Karavaev, Y. (2017). Saturation of the magnetosphere dur- ing superstorms: New results from the magnetogram inversion technique. Solar-Terrestrial Physics, 3(3), 28–36. Retrieved 2022-10-28, from http:// naukaru.ru/en/nauka/article/18490/view doi: 10.12737/stp-33201704 Moen, J., & Brekke, A. (1993). The solar flux influence on quiet time conductances
1142 1143 1144 1145 1146 1147 1148 1149 1150	 Milan, S. E., Walach, M., Carter, J. A., Sangha, H., & Anderson, B. J. (2019). Substorm onset latitude and the steadiness of magnetospheric convection. Journal of Geophysical Research: Space Physics, 124 (3), 1738–1752. Retrieved 2022-12-19, from https://onlinelibrary.wiley.com/doi/abs/10.1029/ 2018JA025969 doi: 10.1029/2018JA025969 Mishin, V., & Karavaev, Y. (2017). Saturation of the magnetosphere dur- ing superstorms: New results from the magnetogram inversion technique. Solar-Terrestrial Physics, 3(3), 28–36. Retrieved 2022-10-28, from http:// naukaru.ru/en/nauka/article/18490/view doi: 10.12737/stp-33201704 Moen, J., & Brekke, A. (1993). The solar flux influence on quiet time conductances in the auroral ionosphere. Geophysical Research Letters, 20(10), 971-974. Re-
1142 1143 1144 1145 1146 1147 1148 1149 1150 1151	 Milan, S. E., Walach, M., Carter, J. A., Sangha, H., & Anderson, B. J. (2019). Substorm onset latitude and the steadiness of magnetospheric convection. Journal of Geophysical Research: Space Physics, 124(3), 1738-1752. Retrieved 2022-12-19, from https://onlinelibrary.wiley.com/doi/abs/10.1029/ 2018JA025969 doi: 10.1029/2018JA025969 Mishin, V., & Karavaev, Y. (2017). Saturation of the magnetosphere dur- ing superstorms: New results from the magnetogram inversion technique. Solar-Terrestrial Physics, 3(3), 28-36. Retrieved 2022-10-28, from http:// naukaru.ru/en/nauka/article/18490/view doi: 10.12737/stp-33201704 Moen, J., & Brekke, A. (1993). The solar flux influence on quiet time conductances in the auroral ionosphere. Geophysical Research Letters, 20(10), 971-974. Re- trieved 2022-12-19, from https://agupubs.onlinelibrary.wiley.com/doi/
1142 1143 1144 1145 1146 1147 1148 1149 1150 1151 1152	 Milan, S. E., Walach, M., Carter, J. A., Sangha, H., & Anderson, B. J. (2019). Substorm onset latitude and the steadiness of magnetospheric convection. Journal of Geophysical Research: Space Physics, 124(3), 1738–1752. Retrieved 2022-12-19, from https://onlinelibrary.wiley.com/doi/abs/10.1029/ 2018JA025969 doi: 10.1029/2018JA025969 Mishin, V., & Karavaev, Y. (2017). Saturation of the magnetosphere dur- ing superstorms: New results from the magnetogram inversion technique. Solar-Terrestrial Physics, 3(3), 28–36. Retrieved 2022-10-28, from http:// naukaru.ru/en/nauka/article/18490/view doi: 10.12737/stp-33201704 Moen, J., & Brekke, A. (1993). The solar flux influence on quiet time conductances in the auroral ionosphere. Geophysical Research Letters, 20(10), 971-974. Re- trieved 2022-12-19, from https://agupubs.onlinelibrary.wiley.com/doi/ abs/10.1029/92GL02109 doi: https://doi.org/10.1029/92GL02109
1142 1143 1144 1145 1146 1147 1148 1149 1150 1151 1152 1153 1154	 Milan, S. E., Walach, M., Carter, J. A., Sangha, H., & Anderson, B. J. (2019). Substorm onset latitude and the steadiness of magnetospheric convection. Journal of Geophysical Research: Space Physics, 124(3), 1738–1752. Retrieved 2022-12-19, from https://onlinelibrary.wiley.com/doi/abs/10.1029/ 2018JA025969 doi: 10.1029/2018JA025969 Mishin, V., & Karavaev, Y. (2017). Saturation of the magnetosphere dur- ing superstorms: New results from the magnetogram inversion technique. Solar-Terrestrial Physics, 3(3), 28–36. Retrieved 2022-10-28, from http:// naukaru.ru/en/nauka/article/18490/view doi: 10.12737/stp-33201704 Moen, J., & Brekke, A. (1993). The solar flux influence on quiet time conductances in the auroral ionosphere. Geophysical Research Letters, 20(10), 971-974. Re- trieved 2022-12-19, from https://agupubs.onlinelibrary.wiley.com/doi/ abs/10.1029/92GL02109 doi: https://doi.org/10.1029/92GL02109 Nagatsuma, T. (2004). Conductivity dependence of cross-polar potential saturation.
1142 1143 1144 1145 1146 1147 1148 1149 1150 1151 1152 1153 1154	 Milan, S. E., Walach, M., Carter, J. A., Sangha, H., & Anderson, B. J. (2019). Substorm onset latitude and the steadiness of magnetospheric convection. Journal of Geophysical Research: Space Physics, 124(3), 1738–1752. Retrieved 2022-12-19, from https://onlinelibrary.wiley.com/doi/abs/10.1029/ 2018JA025969 doi: 10.1029/2018JA025969 Mishin, V., & Karavaev, Y. (2017). Saturation of the magnetosphere dur- ing superstorms: New results from the magnetogram inversion technique. Solar-Terrestrial Physics, 3(3), 28–36. Retrieved 2022-10-28, from http:// naukaru.ru/en/nauka/article/18490/view doi: 10.12737/stp-33201704 Moen, J., & Brekke, A. (1993). The solar flux influence on quiet time conductances in the auroral ionosphere. Geophysical Research Letters, 20(10), 971-974. Re- trieved 2022-12-19, from https://agupubs.onlinelibrary.wiley.com/doi/ abs/10.1029/92GL02109 doi: https://doi.org/10.1029/92GL02109 Nagatsuma, T. (2004). Conductivity dependence of cross-polar potential saturation. Journal of Geophysical Research: Space Physics, 109(A4). Retrieved 2022-12-
1142 1143 1144 1145 1146 1147 1148 1149 1150 1151 1152 1153 1154 1155	 Milan, S. E., Walach, M., Carter, J. A., Sangha, H., & Anderson, B. J. (2019). Substorm onset latitude and the steadiness of magnetospheric convection. Journal of Geophysical Research: Space Physics, 124(3), 1738–1752. Retrieved 2022-12-19, from https://onlinelibrary.wiley.com/doi/abs/10.1029/ 2018JA025969 doi: 10.1029/2018JA025969 Mishin, V., & Karavaev, Y. (2017). Saturation of the magnetosphere dur- ing superstorms: New results from the magnetogram inversion technique. Solar-Terrestrial Physics, 3(3), 28–36. Retrieved 2022-10-28, from http:// naukaru.ru/en/nauka/article/18490/view doi: 10.12737/stp-33201704 Moen, J., & Brekke, A. (1993). The solar flux influence on quiet time conductances in the auroral ionosphere. Geophysical Research Letters, 20(10), 971-974. Re- trieved 2022-12-19, from https://agupubs.onlinelibrary.wiley.com/doi/ abs/10.1029/92GL02109 doi: https://doi.org/10.1029/92GL02109 Nagatsuma, T. (2004). Conductivity dependence of cross-polar potential saturation.
1142 1143 1144 1145 1146 1147 1148 1149 1150 1151 1152 1153 1154 1155 1156	 Milan, S. E., Walach, M., Carter, J. A., Sangha, H., & Anderson, B. J. (2019). Substorm onset latitude and the steadiness of magnetospheric convection. Journal of Geophysical Research: Space Physics, 124(3), 1738–1752. Retrieved 2022-12-19, from https://onlinelibrary.wiley.com/doi/abs/10.1029/ 2018JA025969 doi: 10.1029/2018JA025969 Mishin, V., & Karavaev, Y. (2017). Saturation of the magnetosphere dur- ing superstorms: New results from the magnetogram inversion technique. Solar-Terrestrial Physics, 3(3), 28–36. Retrieved 2022-10-28, from http:// naukaru.ru/en/nauka/article/18490/view doi: 10.12737/stp-33201704 Moen, J., & Brekke, A. (1993). The solar flux influence on quiet time conductances in the auroral ionosphere. Geophysical Research Letters, 20(10), 971-974. Re- trieved 2022-12-19, from https://agupubs.onlinelibrary.wiley.com/doi/ abs/10.1029/92GL02109 doi: https://doi.org/10.1029/92GL02109 Nagatsuma, T. (2004). Conductivity dependence of cross-polar potential saturation. Journal of Geophysical Research: Space Physics, 109(A4). Retrieved 2022-12- 19, from https://agupubs.onlinelibrary.wiley.com/doi/abs/10.1029/ 2003JA010286 doi: https://doi.org/10.1029/2003JA010286
1142 1143 1144 1145 1146 1147 1148 1149 1150 1151 1152 1153 1154 1155 1156	 Milan, S. E., Walach, M., Carter, J. A., Sangha, H., & Anderson, B. J. (2019). Substorm onset latitude and the steadiness of magnetospheric convection. Journal of Geophysical Research: Space Physics, 124 (3), 1738-1752. Retrieved 2022-12-19, from https://onlinelibrary.wiley.com/doi/abs/10.1029/ 2018JA025969 doi: 10.1029/2018JA025969 Mishin, V., & Karavaev, Y. (2017). Saturation of the magnetosphere dur- ing superstorms: New results from the magnetogram inversion technique. Solar-Terrestrial Physics, 3(3), 28-36. Retrieved 2022-10-28, from http:// naukaru.ru/en/nauka/article/18490/view doi: 10.12737/stp-33201704 Moen, J., & Brekke, A. (1993). The solar flux influence on quiet time conductances in the auroral ionosphere. Geophysical Research Letters, 20(10), 971-974. Re- trieved 2022-12-19, from https://agupubs.onlinelibrary.wiley.com/doi/ abs/10.1029/92GL02109 doi: https://doi.org/10.1029/92GL02109 Nagatsuma, T. (2004). Conductivity dependence of cross-polar potential saturation. Journal of Geophysical Research: Space Physics, 109(A4). Retrieved 2022-12- 19, from https://agupubs.onlinelibrary.wiley.com/doi/abs/10.1029/ 2003JA010286 doi: https://doi.org/10.1029/2003JA010286 Newell, P. T., & Gjerloev, J. W. (2011a). Evaluation of SuperMAG auroral electro-
1142 1143 1144 1145 1146 1147 1148 1149 1150 1151 1152 1153 1154 1155 1156 1157 1158	 Milan, S. E., Walach, M., Carter, J. A., Sangha, H., & Anderson, B. J. (2019). Substorm onset latitude and the steadiness of magnetospheric convection. Journal of Geophysical Research: Space Physics, 124 (3), 1738-1752. Retrieved 2022-12-19, from https://onlinelibrary.wiley.com/doi/abs/10.1029/ 2018JA025969 doi: 10.1029/2018JA025969 Mishin, V., & Karavaev, Y. (2017). Saturation of the magnetosphere dur- ing superstorms: New results from the magnetogram inversion technique. Solar-Terrestrial Physics, 3(3), 28-36. Retrieved 2022-10-28, from http:// naukaru.ru/en/nauka/article/18490/view doi: 10.12737/stp-33201704 Moen, J., & Brekke, A. (1993). The solar flux influence on quiet time conductances in the auroral ionosphere. Geophysical Research Letters, 20(10), 971-974. Re- trieved 2022-12-19, from https://agupubs.onlinelibrary.wiley.com/doi/ abs/10.1029/92GL02109 doi: https://doi.org/10.1029/92GL02109 Nagatsuma, T. (2004). Conductivity dependence of cross-polar potential saturation. Journal of Geophysical Research: Space Physics, 109(A4). Retrieved 2022-12- 19, from https://agupubs.onlinelibrary.wiley.com/doi/abs/10.1029/ 2003JA010286 doi: https://doi.org/10.1029/2003JA010286 Newell, P. T., & Gjerloev, J. W. (2011a). Evaluation of SuperMAG auroral electro- jet indices as indicators of substorms and auroral power. Journal of Geophysic
1142 1143 1144 1145 1146 1147 1148 1149 1150 1151 1152 1153 1154 1155 1156 1157 1158 1159 1159	 Milan, S. E., Walach, M., Carter, J. A., Sangha, H., & Anderson, B. J. (2019). Substorm onset latitude and the steadiness of magnetospheric convection. Journal of Geophysical Research: Space Physics, 124 (3), 1738–1752. Retrieved 2022-12-19, from https://onlinelibrary.wiley.com/doi/abs/10.1029/ 2018JA025969 doi: 10.1029/2018JA025969 Mishin, V., & Karavaev, Y. (2017). Saturation of the magnetosphere dur- ing superstorms: New results from the magnetogram inversion technique. Solar-Terrestrial Physics, 3(3), 28–36. Retrieved 2022-10-28, from http:// naukaru.ru/en/nauka/article/18490/view doi: 10.12737/stp-33201704 Moen, J., & Brekke, A. (1993). The solar flux influence on quiet time conductances in the auroral ionosphere. Geophysical Research Letters, 20(10), 971-974. Re- trieved 2022-12-19, from https://agupubs.onlinelibrary.wiley.com/doi/ abs/10.1029/92GL02109 doi: https://doi.org/10.1029/92GL02109 Nagatsuma, T. (2004). Conductivity dependence of cross-polar potential saturation. Journal of Geophysical Research: Space Physics, 109(A4). Retrieved 2022-12- 19, from https://agupubs.onlinelibrary.wiley.com/doi/abs/10.1029/ 2003JA010286 doi: https://doi.org/10.1029/2003JA010286 Newell, P. T., & Gjerloev, J. W. (2011a). Evaluation of SuperMAG auroral electro- jet indices as indicators of substorms and auroral power. Journal of Geophysi- cal Research: Space Physics, 116(A12), 2011JA016779. Retrieved 2022-11-06,
1142 1143 1144 1145 1146 1147 1148 1149 1150 1151 1152 1153 1154 1155 1156 1157 1158 1159 1160 1161	 Milan, S. E., Walach, M., Carter, J. A., Sangha, H., & Anderson, B. J. (2019). Substorm onset latitude and the steadiness of magnetospheric convection. Journal of Geophysical Research: Space Physics, 124 (3), 1738–1752. Retrieved 2022-12-19, from https://onlinelibrary.wiley.com/doi/abs/10.1029/ 2018JA025969 doi: 10.1029/2018JA025969 Mishin, V., & Karavaev, Y. (2017). Saturation of the magnetosphere dur- ing superstorms: New results from the magnetogram inversion technique. Solar-Terrestrial Physics, 3(3), 28–36. Retrieved 2022-10-28, from http:// naukaru.ru/en/nauka/article/18490/view doi: 10.12737/stp-33201704 Moen, J., & Brekke, A. (1993). The solar flux influence on quiet time conductances in the auroral ionosphere. Geophysical Research Letters, 20(10), 971-974. Re- trieved 2022-12-19, from https://agupubs.onlinelibrary.wiley.com/doi/ abs/10.1029/92GL02109 doi: https://doi.org/10.1029/92GL02109 Nagatsuma, T. (2004). Conductivity dependence of cross-polar potential saturation. Journal of Geophysical Research: Space Physics, 109(A4). Retrieved 2022-12- 19, from https://agupubs.onlinelibrary.wiley.com/doi/abs/10.1029/ 2003JA010286 doi: https://doi.org/10.1029/2003JA010286 Newell, P. T., & Gjerloev, J. W. (2011a). Evaluation of SuperMAG auroral electro- jet indices as indicators of substorms and auroral power. Journal of Geophysi- cal Research: Space Physics, 116(A12), 2011JA016779. Retrieved 2022-11-06, from https://onlinelibrary.wiley.com/doi/10.1029/2011JA016779 doi:
1142 1143 1144 1145 1146 1147 1148 1149 1150 1151 1152 1153 1154 1155 1155 1156 1157 1158 1159 1160 1161	 Milan, S. E., Walach, M., Carter, J. A., Sangha, H., & Anderson, B. J. (2019). Substorm onset latitude and the steadiness of magnetospheric convection. Journal of Geophysical Research: Space Physics, 124 (3), 1738–1752. Retrieved 2022-12-19, from https://onlinelibrary.wiley.com/doi/abs/10.1029/ 2018JA025969 doi: 10.1029/2018JA025969 Mishin, V., & Karavaev, Y. (2017). Saturation of the magnetosphere dur- ing superstorms: New results from the magnetogram inversion technique. Solar-Terrestrial Physics, 3(3), 28–36. Retrieved 2022-10-28, from http:// naukaru.ru/en/nauka/article/18490/view doi: 10.12737/stp-33201704 Moen, J., & Brekke, A. (1993). The solar flux influence on quiet time conductances in the auroral ionosphere. Geophysical Research Letters, 20(10), 971-974. Re- trieved 2022-12-19, from https://agupubs.onlinelibrary.wiley.com/doi/ abs/10.1029/92GL02109 doi: https://doi.org/10.1029/92GL02109 Nagatsuma, T. (2004). Conductivity dependence of cross-polar potential saturation. Journal of Geophysical Research: Space Physics, 109(A4). Retrieved 2022-12- 19, from https://agupubs.onlinelibrary.wiley.com/doi/abs/10.1029/ 2003JA010286 doi: https://doi.org/10.1029/2003JA010286 Newell, P. T., & Gjerloev, J. W. (2011a). Evaluation of SuperMAG auroral electro- jet indices as indicators of substorms and auroral power. Journal of Geophysi- cal Research: Space Physics, 116(A12), 2011JA016779. Retrieved 2022-11-06,
1142 1143 1144 1145 1146 1147 1148 1149 1150 1151 1152 1153 1154 1155 1155 1156 1157 1158 1159 1160 1161	 Milan, S. E., Walach, M., Carter, J. A., Sangha, H., & Anderson, B. J. (2019). Substorm onset latitude and the steadiness of magnetospheric convection. Journal of Geophysical Research: Space Physics, 124 (3), 1738–1752. Retrieved 2022-12-19, from https://onlinelibrary.wiley.com/doi/abs/10.1029/ 2018JA025969 doi: 10.1029/2018JA025969 Mishin, V., & Karavaev, Y. (2017). Saturation of the magnetosphere dur- ing superstorms: New results from the magnetogram inversion technique. Solar-Terrestrial Physics, 3(3), 28–36. Retrieved 2022-10-28, from http:// naukaru.ru/en/nauka/article/18490/view doi: 10.12737/stp-33201704 Moen, J., & Brekke, A. (1993). The solar flux influence on quiet time conductances in the auroral ionosphere. Geophysical Research Letters, 20(10), 971-974. Re- trieved 2022-12-19, from https://agupubs.onlinelibrary.wiley.com/doi/ abs/10.1029/92GL02109 doi: https://doi.org/10.1029/92GL02109 Nagatsuma, T. (2004). Conductivity dependence of cross-polar potential saturation. Journal of Geophysical Research: Space Physics, 109(A4). Retrieved 2022-12- 19, from https://agupubs.onlinelibrary.wiley.com/doi/abs/10.1029/ 2003JA010286 doi: https://doi.org/10.1029/2003JA010286 Newell, P. T., & Gjerloev, J. W. (2011a). Evaluation of SuperMAG auroral electro- jet indices as indicators of substorms and auroral power. Journal of Geophysic cal Research: Space Physics, 116(A12), 2011JA016779. Retrieved 2022-11-06, from https://onlinelibrary.wiley.com/doi/10.1029/2011JA016779 doi: 10.1029/2011JA016779
1142 1143 1144 1145 1146 1147 1148 1149 1150 1151 1152 1153 1154 1155 1156 1157 1158 1159 1160 1161 1162 1163	 Milan, S. E., Walach, M., Carter, J. A., Sangha, H., & Anderson, B. J. (2019). Substorm onset latitude and the steadiness of magnetospheric convection. Journal of Geophysical Research: Space Physics, 124 (3), 1738–1752. Retrieved 2022-12-19, from https://onlinelibrary.wiley.com/doi/abs/10.1029/ 2018JA025969 doi: 10.1029/2018JA025969 Mishin, V., & Karavaev, Y. (2017). Saturation of the magnetosphere dur- ing superstorms: New results from the magnetogram inversion technique. Solar-Terrestrial Physics, 3(3), 28–36. Retrieved 2022-10-28, from http:// naukaru.ru/en/nauka/article/18490/view doi: 10.12737/stp-33201704 Moen, J., & Brekke, A. (1993). The solar flux influence on quiet time conductances in the auroral ionosphere. Geophysical Research Letters, 20(10), 971-974. Re- trieved 2022-12-19, from https://agupubs.onlinelibrary.wiley.com/doi/ abs/10.1029/92GL02109 doi: https://doi.org/10.1029/92GL02109 Nagatsuma, T. (2004). Conductivity dependence of cross-polar potential saturation. Journal of Geophysical Research: Space Physics, 109(A4). Retrieved 2022-12- 19, from https://agupubs.onlinelibrary.wiley.com/doi/abs/10.1029/ 2003JA010286 doi: https://doi.org/10.1029/2003JA010286 Newell, P. T., & Gjerloev, J. W. (2011a). Evaluation of SuperMAG auroral electro- jet indices as indicators of substorms and auroral power. Journal of Geophysi- cal Research: Space Physics, 116(A12), 2011JA016779. Retrieved 2022-11-06, from https://onlinelibrary.wiley.com/doi/10.1029/2011JA016779 doi: 10.1029/2011JA016779 Newell, P. T., & Gjerloev, J. W. (2011b). Substorm and magnetosphere charac-
1142 1143 1144 1145 1146 1147 1148 1149 1150 1151 1152 1153 1154 1155 1156 1157 1158 1159 1160 1161 1162 1163	 Milan, S. E., Walach, M., Carter, J. A., Sangha, H., & Anderson, B. J. (2019). Substorm onset latitude and the steadiness of magnetospheric convection. Journal of Geophysical Research: Space Physics, 124 (3), 1738–1752. Retrieved 2022-12-19, from https://onlinelibrary.wiley.com/doi/abs/10.1029/ 2018JA025969 doi: 10.1029/2018JA025969 Mishin, V., & Karavaev, Y. (2017). Saturation of the magnetosphere dur- ing superstorms: New results from the magnetogram inversion technique. Solar-Terrestrial Physics, 3(3), 28–36. Retrieved 2022-10-28, from http:// naukaru.ru/en/nauka/article/18490/view doi: 10.12737/stp-33201704 Moen, J., & Brekke, A. (1993). The solar flux influence on quiet time conductances in the auroral ionosphere. Geophysical Research Letters, 20(10), 971-974. Re- trieved 2022-12-19, from https://agupubs.onlinelibrary.wiley.com/doi/ abs/10.1029/92GL02109 doi: https://doi.org/10.1029/92GL02109 Nagatsuma, T. (2004). Conductivity dependence of cross-polar potential saturation. Journal of Geophysical Research: Space Physics, 109(A4). Retrieved 2022-12- 19, from https://agupubs.onlinelibrary.wiley.com/doi/abs/10.1029/ 2003JA010286 doi: https://doi.org/10.1029/2003JA010286 Newell, P. T., & Gjerloev, J. W. (2011a). Evaluation of SuperMAG auroral electro- jet indices as indicators of substorms and auroral power. Journal of Geophysic al Research: Space Physics, 116(A12), 2011JA016779. Retrieved 2022-11-06, from https://onlinelibrary.wiley.com/doi/10.1029/2011JA016779 doi: 10.1029/2011JA016779 Newell, P. T., & Gjerloev, J. W. (2011b). Substorm and magnetosphere charac- teristic scales inferred from the SuperMAG auroral electrojet indices. Jour- inform https://onlinelibrary.wiley.com/doi/10.1029/2011JA016779

1169	Newell, P. T., & Gjerloev, J. W. (2012). SuperMAG-based partial ring cur-
1170	rent indices. Journal of Geophysical Research: Space Physics, 117(A5),
1171	2012JA017586. Retrieved 2022-12-11, from https://onlinelibrary.wiley
1172	.com/doi/10.1029/2012JA017586 doi: 10.1029/2012JA017586
1173	Newell, P. T., Sotirelis, T., Skura, J. P., Meng, CI., & Lyatsky, W. (2002). Ultravi-
1174	olet insolation drives seasonal and diurnal space weather variations. Journal of
1175	Geophysical Research, 107(A10), 1305. Retrieved 2022-12-09, from http://doi
1176	.wiley.com/10.1029/2001JA000296 doi: 10.1029/2001JA000296
1177	Ou, J., Du, A., Ge, Y., Luo, H., Zhang, Y., & Guo, Z. (2022). Statistical study
1178	on the North-South asymmetric distribution of the mid-low-latitude nightside
1179	disturbed magnetic fields. Journal of Geophysical Research: Space Physics,
1180	127(3). Retrieved 2022-12-19, from https://onlinelibrary.wiley.com/doi/
1181	10.1029/2021JA029970 doi: 10.1029/2021JA029970
1182	Park, K. S., Ogino, T., & Walker, R. J. (2006). On the importance of antiparallel
1183	reconnection when the dipole tilt and IMF B_{-y} are nonzero. Journal of Geo-
1184	physical Research, 111(A5), A05202. Retrieved 2022-12-12, from http://doi
1185	.wiley.com/10.1029/2004JA010972 doi: 10.1029/2004JA010972
1186	Ridley, A. J., Gombosi, T. I., & DeZeeuw, D. L. (2004). Ionospheric control of the
1187	magnetosphere: conductance. Annales Geophysicae, 22(2), 567–584. Retrieved
1188	2022-11-10, from https://angeo.copernicus.org/articles/22/567/2004/
1189	doi: 10.5194/angeo-22-567-2004
1190	Russell, C. T., & McPherron, R. L. (1973). Semiannual variation of geomagnetic
1190	activity. Journal of Geophysical Research, 78(1), 92–108. Retrieved 2022-11-
1191	03, from http://doi.wiley.com/10.1029/JA078i001p00092 doi: 10.1029/
1192	JA078i001p00092
1193	Russell, C. T., Wang, Y. L., & Raeder, J. (2003). Possible dipole tilt dependence of
1194	dayside magnetopause reconnection. <i>Geophysical Research Letters</i> , 30(18). Re-
1195	trieved 2022-12-12, from http://doi.wiley.com/10.1029/2003GL017725 doi:
1190	10.1029/2003GL017725
	Spence, H. E. (1996). The what, where, when, and why of magnetospheric substorm
1198	triggers. Eos, Transactions American Geophysical Union, 77(9), 81–86. Re-
1199 1200	trieved 2022-12-19, from http://doi.wiley.com/10.1029/96E000051 doi: 10
1200	.1029/96EO00051
1201	Stauning, P. (2007). A new index for the interplanetary merging electric field
1202	and geomagnetic activity: Application of the unified polar cap indices. Space
1203	Weather, 5(9), n/a-n/a. Retrieved 2023-02-19, from http://doi.wiley.com/
1204	10.1029/2007SW000311 doi: 10.1029/2007SW000311
1205	Tanaka, T., Ebihara, Y., Watanabe, M., Den, M., Fujita, S., Kikuchi, T.,
1200	Kataoka, R. (2021). Roles of the M-I coupling and plasma sheet dissipa-
1207	tion on the growth-phase thinning and subsequent transition to the onset.
1200	Journal of Geophysical Research: Space Physics, 126(12). Retrieved 2022-12-
1209	19, from https://onlinelibrary.wiley.com/doi/10.1029/2021JA029925
1210	doi: 10.1029/2021JA029925
1211	Thébault, E., Finlay, C. C., Beggan, C. D., Alken, P., Aubert, J., Barrois, O.,
1212	Zvereva, T. (2015). International Geomagnetic Reference Field: the
1213	12th generation. Earth, Planets and Space, 67(1), 79. Retrieved 2022-11-
1214	25, from http://www.earth-planets-space.com/content/67/1/79 doi:
	10.1186/s40623-015-0228-9
1216	Trattner, K. J., Petrinec, S. M., Fuselier, S. A., & Phan, T. D. (2012). The lo-
1217	cation of reconnection at the magnetopause: Testing the maximum mag-
1218	netic shear model with THEMIS observations. Journal of Geophysical Re-
1219	search: Space Physics, 117(A1), 2011JA016959. Retrieved 2023-04-09, from
1220	https://onlinelibrary.wiley.com/doi/10.1029/2011JA016959 doi:
1221	10.1029/2011JA016959
1222	Troshichev, O. (2022). PC index as a ground-based indicator of the solar wind

1224	energy incoming into the magnetosphere: (1) relation of PC index to the so-
1225	lar wind electric field EKL. Frontiers in Astronomy and Space Sciences,
1226	9, 1069470. Retrieved 2023-02-19, from https://www.frontiersin.org/
1227	articles/10.3389/fspas.2022.1069470/full doi: 10.3389/fspas.2022
1228	.1069470
1229	Tulegenov, B., Raeder, J., Cramer, W. D., Ferdousi, B., Fuller-Rowell, T. J.,
1230	Maruyama, N., & Strangeway, R. J. (2023). Storm time polar cap expansion:
1231	interplanetary magnetic field clock angle dependence. Annales Geophysicae,
1232	41(1), 39-54. Retrieved 2023-01-20, from https://angeo.copernicus.org/
1233	articles/41/39/2023/ doi: 10.5194/angeo-41-39-2023
1234	Wang, H., & Lühr, H. (2007). Seasonal-longitudinal variation of substorm occur-
1235	rence frequency: Evidence for ionospheric control. Geophysical Research Let-
1236	ters, 34(7), L07104. Retrieved 2022-11-27, from http://doi.wiley.com/10
1237	.1029/2007GL029423 doi: 10.1029/2007GL029423
1238	Wang, H., Zhang, K. D., Wan, X., & Lühr, H. (2017). Universal time variation
1239	of high-latitude thermospheric disturbance wind in response to a substorm.
1240	Journal of Geophysical Research: Space Physics, 122(4), 4638–4653. Retrieved
1241	2022-11-27, from http://doi.wiley.com/10.1002/2016JA023630 doi:
1242	10.1002/2016JA023630
1243	Zhang, B., Lotko, W., Brambles, O., Wiltberger, M., & Lyon, J. (2015). Electron
1244	precipitation models in global magnetosphere simulations. Journal of Geo-
1245	physical Research: Space Physics, 120(2), 1035–1056. Retrieved 2022-12-09,
1246	from https://onlinelibrary.wiley.com/doi/10.1002/2014JA020615 doi:
1247	10.1002/2014JA020615
1248	Zhao, H., & Zong, QG. (2012). Seasonal and diurnal variation of geomagnetic
1249	activity: Russell-McPherron effect during different IMF polarity and/or ex-
1250	treme solar wind conditions. Journal of Geophysical Research: Space Physics,
1251	117(A11), n/a-n/a. Retrieved 2022-12-29, from http://doi.wiley.com/
1252	10.1029/2012JA017845 doi: 10.1029/2012JA017845
1253	Zhu, C. B., Zhang, H., Ge, Y. S., Pu, Z. Y., Liu, W. L., Wan, W. X., Wang,
1254	Y. F. (2015). Dipole tilt angle effect on magnetic reconnection locations on
1255	the magnetopause. Journal of Geophysical Research: Space Physics, $120(7)$,
1256	5344-5354. Retrieved 2023-04-09, from https://onlinelibrary.wiley.com/
1257	doi/10.1002/2015JA020989 doi: 10.1002/2015JA020989
1258	Zou, Y., Lyons, L., Conde, M., Varney, R., Angelopoulos, V., & Mende, S. (2021).
1259	Effects of substorms on high-latitude upper thermospheric winds. Journal
1260	of Geophysical Research: Space Physics, 126(1). Retrieved 2023-04-09, from
1261	https://onlinelibrary.wiley.com/doi/10.1029/2020JA028193 doi:
1262	10.1029/2020JA028193

1263 7 Open Research

The data used in this study are all openly available. The interplanetary data are available from the Physics Data Facility (SPDF) at NASA's Goddard Space Flight Center as the Omni composite from https://omniweb.gsfc.nasa.gov/ow_min.html. The SuperMAG SML and SMU indices and the substorm onset lists are available from the SuperMAG project website at the Johns Hopkins University Applied Physics Laboratory at http://supermag.jhuapl.edu/indices/.

1270 Acknowledgments

1271The authors are grateful to the many instrument scientists and engineers who make1272the datasets employed in this study possible and the staff of a number of datacentres who1273allow easy access to the data: in particular the Space Physics Data Facility (SPDF) at1274NASA's Goddard Space Flight Center for the Omni composite of interplanetary obser-

vations and the SuperMAG project staff coordinated at The Johns Hopkins University

1276 Applied Physics Laboratory, for the SMR and SML indices. The author thanks the many

PIs and instrument teams who contribute data to the SuperMAG project. This work is

 $_{1278}$ supported by a number of grants: consolidated grants number ST/R000921/1 and ST/V000497/1

¹²⁷⁹ from the United Kingdom Science and Technology Facilities Council (UKRI/STFC) and

the SWIGS Directed Highlight Topic Grant number NE/P016928/1/ and grant NE/S010033/1 $\,$

¹²⁸¹ from the United Kingdom Natural Environment Research Council (UKRI/NERC).